East African Journal of Biophysical and Computational Sciences

(E A J B C S)

ISSN (Online): 2789-3618 and ISSN (Print): 2789-360X

COLLEGE OF NATURAL AND COMPUTATIONAL SCIENCES,
HAWASSA UNIVERSITY

Volume 6 Issue 2 December, 2025

East African Journal of Biophysical and Computational Sciences
ISSN (Online): 2789-3618 and ISSN (Print): 2789-360X

East African Journal of Biophysical and Computational Sciences (EAJBCS)

ISSN (Online): 2789-3618 and ISSN (Print): 2789-360X

Volume 6 Issue 2

College of Natural and Computational Sciences
Hawassa University

December, 2025

Table of Contents

East African Journal of Biophysical and Computational Sciences (EAJBCS)

East African Journal of Biophysical and Computational Sciences (EAJBCS) whose ISSN (Online): 2789-3618 and ISSN (Print): 2789-360X is a double-blind peer-reviewed open-access journal published by Hawassa University, College of Natural & Computational Sciences. This Journal is a multi and interdisciplinary journal that is devoted to attracting high-quality, latest, and valuable advancements in the fields of natural sciences. The Journal invites publications from different geographical contexts and disciplines to advance the depths of knowledge related to physics, chemistry, geology, biology, & veterinary medicine. The manuscript originated from other sciences such as biotechnology, sport science, statistics, and mathematics can also be accepted based on their adjunct nature. The Journal encourages publications of both scholarly and industrial papers on various themes with the aim of giving innovative solutions to natural sciences. It encourages the publishing of open access academic journals on a regular basis (presumably biannual). The Journal publishes original research articles, critical reviews, mini-reviews, short communications, case reports related to the specific theme & a variety of special issues in English. The Journal, published under the Creative Commons open access license (CC BY-NC-ND), doesn't charge fees for publishing an article and hence offers an opportunity to all social classes regardless of their economic statuses. This helps to promote academic research published by resource-poor researchers as a mechanism to give back to society.

The journal is already indexed on known databases like AJOL, DOAJ and CABI ABSTRACTS

Editorial Team

East African Journal of Biophysical and Computational Sciences
ISSN (Online): 2789-3618 and ISSN (Print): 2789-360X

Journal Information

Volume 6(2), 2025
DOI: https://dx.doi.org/10.4314/eajbcs.v6i2.1S

Homepage:
https://journals.hu.edu.et/hu-journals/index.php/eajbcs

Article History
Received: 15 October, 2025
Accepted: 20 November, 2025
Published Online: 25 December, 2025

How to cite
Bekele S.S. and Arara A.A. (2025). Mathematical Modeling of Smooth Curve from Sampled Data via the Discrete Biharmonic Equation. *East African Journal of Biophysical and Computational Sciences* Volume 6(2), 2025. .1-13

Open Access

ARTICLE

Mathematical Modeling of Smooth Curve from Sampled Data via the Discrete Biharmonic Equation

Samson Seifu Bekele[1,*], **Alemayehu Adugna Arara**[1]

[1]Department of Mathematics, Hawassa University, Ethiopia.
*Corresponding author: samsonse@hu.edu.et

Abstract

Curve reconstruction is the process of estimating a smooth function or curve that fits a given set of data points, either exactly (interpolation) or approximately (fitting). Classical approaches, including global polynomial interpolation, splines, Hermite interpolation, and radial basis function fitting, face challenges when data are sparse, irregularly distributed, or noisy. In this paper, we propose a curve reconstruction method based on the discrete form of the biharmonic equation. The method formulates reconstruction as a constrained quadratic optimization problem, incorporating both equality and inequality constraints and producing globally C^1 smooth curves. The approach is physically interpretable, penalizing excessive bending, as in the case of a thin elastic beam, and can be extended to higher-dimensional surface reconstruction. Performance is evaluated through numerical experiments on known functions and synthetic data with various distributions and constraints, including small perturbation tests to assess stability and robustness. The results demonstrate that the proposed method reproduces the data, enforces the prescribed bounds, and remains stable under irregular sampling and noise.

Keywords: Curve reconstruction; Biharmonic equation; Constrained quadratic programming problem; Interpolation; Variational form.

East African Journal of Biophysical and Computational Sciences (EAJBCS) is already indexed on known databases like AJOL, DOAJ, CABI ABSTRACTS and FAO AGRIS.

1 Introduction

Curve reconstruction is a process by which a curve or function is determined that either fits or passes exactly through a given set of data points. It can be seen as an inverse problem, where the given data are considered as observations and the curve is unknown or is to be estimated. In general, there are two approaches to curve reconstruction, namely interpolation and fitting (approximation, regression). Interpolation is the process of constructing a curve that passes exactly through all given data points. It is suitable when the data are exact. Fitting, on the other hand, involves finding a curve that approximates the data points but may not pass through any of them, often minimizing the total error between the curve and the points. It is appropriate when the data have measurement errors, noise, or uncertainty.

Both approaches are applicable in a number of areas ranging from digital signal processing and numerical integration to computer graphics, computer-aided design (CAD), and geosciences, among others (Farin, 2002; Li & Heap, 2008; Mazarguil et al., 2022; Phillips, 2003; Piegl & Tiller, 2012).

Among the classical interpolation methods, global polynomial interpolation is one, where a unique polynomial of degree n

is chosen to pass through $n + 1$ given data points. This method provides an explicit analytic form for the interpolant. The unknowns in the polynomial are computed by solving a corresponding system of linear equations whose coefficient matrix is a Vandermonde matrix. The method provides a smooth interpolating curve but has some drawbacks. If one data point is added or removed, the polynomial must be recomputed from scratch. Moreover, the coefficient matrix is highly ill-conditioned even for a small number of data points n (e.g., $n \geq 10$ or so), leading to large numerical errors. Lagrange interpolation reformulates the problem using basis polynomials instead of monomials. This formulation provides an explicit, closed-form solution, thereby avoiding the need to solve a system of linear equations. However, it still shares the same core limitation: adding new data requires recalculating the entire polynomial, which makes it computationally expensive (Hoffman & Frankel, 2018; Zarowski, 2004). Newton's divided difference method, on the other hand, improves this by offering a hierarchical recursive form, which reuses previous computations when new points are introduced, making it more practical, though still susceptible to oscillations (Runge's phenomenon) for high degrees (Hoffman & Frankel, 2018; Phillips, 2003).

Instead of relying on a single high-order global polynomial, piecewise polynomial interpolation is an alternative approach that provides a more stable result and avoids some of the aforementioned drawbacks. The simplest examples are piecewise constant (nearest-neighbor) and piecewise linear methods. These methods are easy to implement but are either discontinuous (in the constant case) or only C^0 continuous with sharp corners (in the linear case) at the data points. Spline interpolation generalizes this idea by connecting together low-degree polynomials while enforcing smoothness at the points. In particular, cubic splines ensure the continuity of the function and its first two derivatives. A key property is that, among all globally C^2 interpolants, the natural cubic spline uniquely minimizes the L^2 norm of the second derivative. Different forms exist, such as natural splines, with zero curvature at the ends, and clamped splines, with prescribed endpoint slopes (de Boor, 2001; Schumaker, 2007). Additional approaches for reconstruction using function values can be found in (Farin, 2002; Hoffman & Frankel, 2018).

In addition to interpolation using function values, derivative information can also be incorporated. This is the principle behind Hermite interpolation, which constructs a piecewise polynomial that not only matches the given values but also respects the slopes at each node (Xu & Xu, 2022).

In spatial statistics, kriging is one of the most widely used interpolation methods. It provides the best linear unbiased estimator (BLUE) of unknown values (Chiles & Delfiner, 2012; Journel & Huijbregts, 1978). The method treats the data as realizations of a random field characterized by a covariance function $C(h)$. Predictions at unsampled locations are obtained as weighted averages of observed data, with the weights chosen to minimize the mean square prediction error. As a result, kriging yields unbiased estimates, explicitly accounts for spatial correlation, and quantifies prediction uncertainty. These features make it particularly effective when data are noisy or sparse, although it is not primarily intended for geometric curve reconstruction (Cressie, 1993).

Fitting methods relax the strict requirement of passing exactly through all data points. Instead, they approximate the data by minimizing residual errors, most commonly in the least-squares sense. Such approaches are generally more robust to noise and outliers, making them better suited to real-world datasets where exact measurements are rarely available (Hoffman & Frankel, 2018).

Despite the wide range of available interpolation and fitting methods, several challenges remain. Interpolation enforces exact agreement with the data points, which can lead to overfitting and oscillations, such as Runge's phenomenon. Fitting methods, by minimizing residuals, allow for smoothing but require careful selection of the model and regularization. Extending these approaches to two-dimensional surface reconstruction with sparse or irregularly spaced points is often difficult. Moreover, many classical methods struggle to systematically incorporate both equality and inequality constraints and generally lack a direct physical interpretation.

The motivation behind this study arises from the problem of reconstructing the bedrock topography of a region from sparse measurement data, such as wells or exposed bedrock outcrops, which has been the focus of subsequent studies (Kitterød, 2017; Kitterød & Leblois, 2019, 2021). To gain intuition, we first consider the one-dimensional analogue: reconstructing a smooth curve from discrete points. To this end, we employ the biharmonic equation from elasticity theory, which penalizes excessive bending and produces globally smooth solutions suitable for both one- and two-dimensional reconstructions (Szilard, 2004). Conceptually, the biharmonic equation models the deflection of a thin elastic plate or beam, and by applying appropriate constraints, it is possible to deform and generate a surface or curve that honors the given data.

In this paper, we propose a discrete biharmonic formulation for curve reconstruction, framed as a constrained quadratic optimization problem. This method naturally incorporates both equality and inequality constraints, handles irregularly spaced data, and provides a physically interpretable principle of smoothness. Moreover, it establishes a framework for surface reconstruction in higher dimensions.

The structure of this paper is as follows. Section 2 introduces the proposed curve reconstruction model. In Section 3, we detail the discretization method employed. Section 4 then presents the constrained quadratic programming approach used to solve the resulting discrete system. A discussion of performance evaluation metrics is provided in Section 5. Finally, the numerical results, discussion, and conclusion are presented in Sections 6, 7, and 8, respectively.

2 Mathematical Modeling

In this section, we explain how a smooth curve is generated from a given set of data points on the $xy-$plane. For this purpose,

let $0 \leq x_1, x_2, \ldots, x_n \leq L$ be locations of data points on the x axis and let $y_1, y_2, \ldots, y_n$ represent the corresponding measurements(exact values or bounds) along the y-axis. Our main goal is to construct a globally C^1 smooth curve that honours the given data while satisfying the specified equality and inequality constraints at each point. For this end we consider the biharmonic equation problem on $\Omega = [0, L]$:

$$u^{(4)}(x) = q(x), \text{in } \Omega, \tag{1a}$$

with Dirichlet boundary conditions

$$u(0) = y_0, \qquad u(L) = y_L, \tag{1b}$$
$$u'(0) = \alpha, \qquad u'(L) = \beta. \tag{1c}$$

In the context of beam theory, the variable u denotes the transverse deflection, while q represents the applied lateral load. The conditions given in (1b, 1c) correspond to Dirichlet boundary conditions for (1a) and physically model a beam that is clamped at both ends. Let $\partial\Omega = \partial\Omega_D$ denote the boundary of the region Ω which in this case is $\{0, L\}$.

In particular if $x_0 = 0$ and $x_n = L$, then $y_0 = y_1$ and $y_L = y_n$. Given the Sobolev space

$$\mathcal{H}^2(\Omega) = \left\{u \in L^2(\Omega) \;\middle|\; D^\alpha u \in L^2(\Omega),\ \forall |\alpha| \leq 2\right\}$$

and the subspace

$$\mathcal{H}^2_D = \{v \in \mathcal{H}^2(\Omega) : v|_{\partial\Omega_D} = v'|_{\partial\Omega_D} = 0\},$$

the variational form of (1) is:

Find $u \in \mathcal{H}^2(\Omega)$ satisfying the boundary conditions (1b), (1c) and

$$\int_\Omega u''v''dx = \int_\Omega qvdx, \quad \forall v \in \mathcal{H}^2_D. \tag{2}$$

In addition, at the given data points a set of constraints must be satisfied:

$$u(x_i) = y_i, \quad \text{for } i \in \mathcal{E}, \tag{3}$$
$$u(x_i) \leq y_i, \quad \text{for } i \in \mathcal{I}, \tag{4}$$

where $\mathcal{E}$ is the indices of the data points where the measured values are exact, and $\mathcal{I}$ the set of indices corresponding to data points where the measurements define inequality conditions. These sets are disjoint ($\mathcal{E} \cap \mathcal{I} = \phi$), allowing the reconstruction to satisfy equality conditions at $\mathcal{E}$ and inequality bounds at $\mathcal{I}$.

The idea in this curve reconstruction approach is based on the use of the discrete form of (2, 3, 4) to mimic a deflected beam satisfying the given boundary conditions and constraints provided in the data.

The weak form (2) can be written in the abstract form as: Find $u \in \mathcal{H}^2(\Omega)$ satisfying the boundary conditions (1b) such that,

$$a(u, v) = l(v), \quad \forall v \in \mathcal{H}^2_D.$$

Here $a(u, v) = \int_\Omega u''v''dx$ and $l(v) = \int_\Omega qvdx$ represent the bilinear and linear forms respectively. This weak form is equivalent to the energy minimization problem where the solution u minimizes the functional:

$$J(v) = \frac{1}{2}a(v, v) - l(v).$$

In the sense of beam theory, the quantities $\frac{1}{2}a(u, u) = \frac{1}{2}\int_\Omega (u'')^2dx$ and $l(u) = \int_\Omega q(x)u(x)dx$ represent the strain (elastic) energy and potential energy (work done by applied forces), respectively (Gavin, 2014; Szilard, 2004). The former represents the energy stored in the beam as a result of bending, quantifies the internal resistance of the material to deformation, which increases with the curvature of the beam. Since $q(x)$ is a distributed load and $u(x)$ is the deflection at the point x, the product $q(x)u(x)$ gives the infinitesimal work done by the applied force. The total energy of the system is then expressed as:

$$\Pi[u] = \frac{1}{2}\int_\Omega (u'')^2dx - \int_\Omega q(x)u(x)dx. \tag{5}$$

3 Discretization

The discrete form of (2, 3, 4) can be obtained by using the Finite Element Method (FEM) (Larson & Bengzon, 2013; Quarteroni, 2009) taking a finite dimensional function space:

$$\mathcal{V}_h = \text{Span}\{\phi_0, \phi_1, \ldots, \phi_{n_{\text{dof}}-1}\} \subset \mathcal{H}^2(\Omega),$$

where ϕ_i are suitably chosen basis (shape) functions, and n_{dof} denotes the total number of degrees of freedom (DOF). The associated subspace that satisfies the homogeneous Dirichlet boundary conditions is defined as :

$$\mathcal{V}^h_D = \{\phi \in \mathcal{V}_h : \phi = \phi' = 0, \quad \text{on } \partial\Omega\}.$$

To define the basis functions, the physical domain $\Omega = [0, L]$ is partitioned into N finite elements (subintervals) as:

$$0 = \xi_0 < \xi_1 < \xi_2 < \ldots < \xi_N = L,$$

where $h_i = x_{i+1} - x_i$ denotes the length of the ith element (for a uniform mesh, $h_i = h$). This process converts the continuous domain into a computational mesh consisting of nodes $\{x_i\}_{i=0}^N$ and elements $[x_i, x_{i+1}]$.

Within each element, local basis (shape) functions are defined, and the global basis functions $\{\phi_i(x)\}_{i=0}^{n_{\text{dof}}-1}$ are constructed by assembling the local contributions according to the mesh connectivity. These basis functions provide the finite-dimensional approximation space $\mathcal{V}_h \subset \mathcal{H}^2(\Omega)$ used for the discrete formulation.

Within this finite dimensional space, the unknown displacement $u(x)$ is approximated as a linear combination of these basis functions, as:

$$u_h(x) := \sum_{i=0}^{n_{\text{dof}}-1} c_i \phi_i(x),$$

where the coefficients c_i's are the unknown degrees of freedom(DOF) of the system.

But, for the finite element space $\mathcal{V}_h$ to be a valid subspace of $\mathcal{H}^2(\Omega)$, the minimum requirement on its basis function is C^1 continuity. This ensures, the functions as well as their weak first and second derivatives be square integrable across elements boundary, hence belong to $\mathcal{H}^2$.

To determine these basis functions in a reference element, completeness and compatibility requirements (Ottosen & Petersson, 1991) indicate that the element level deflection u^e must be expressed as:

$$u^e(x) = \alpha_0 + \alpha_1 x + \alpha_2 x^2 + \alpha_3 x^3, \quad x \in [\xi_i, \xi_{i+1}].$$

Taking the displacement and slope DOF at the ends $u^e(0) = u_i, (u^e)'(0) = \theta_i, u^e(h) = u_{i+1}, (u^e)'(h) = \theta_{i+1}$, we can show that

$$u^e(x) = \mathbf{N}^e(x)\mathbf{d}^e,$$

where

- $\mathbf{d}^e = [u_i, \theta_i, u_{i+1}, \theta_{i+1}]^T$ is the vector of nodal DOFs (displacements u and slope θ),
- $\mathbf{N}^e(x) = [\phi_1^e(x), \phi_2^e(x), \phi_3^e(x), \phi_4^e(x)]$ is the row vector of shape functions.

Moreover the element basis functions are given in closed form as:

$$\phi_1^e(x) = 1 - 3\frac{x^2}{h^2} + 2\frac{x^3}{h^3}, \qquad \phi_3^e(x) = \frac{x^2}{h^2}\left(3 - 2\frac{x}{h}\right),$$
$$\phi_2^e(x) = x\left(1 - 2\frac{x}{h} + \frac{x^2}{h^2}\right), \quad \phi_4^e(x) = \frac{x^2}{h}\left(\frac{x}{h} - 1\right).$$

Two basis function at each grid node of the mesh are generated one for the displacement and one for the slope. The global basis functions are then defined using two adjacent element basis functions and zero in all other elements. In Fig. 1 the domain $[0, L]$ is discretized into five subintervals and a total of twelve global basis functions are defined: four $(\phi_0, \phi_1, \phi_{10}, \phi_{11})$ correspond to boundary basis functions, while for the internal nodes, ϕ_i with even i represent displacement DOFs and the remaining functions correspond to slope DOFs at each node.

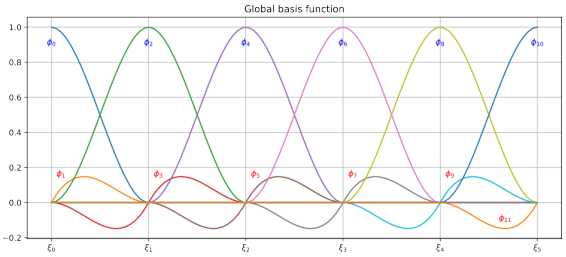

Figure 1: Graphical illustration of the global basis functions. The domain is subdivided into five elements with six nodes.

In this way, we construct the nodal displacement basis functions ϕ_{2i} and the nodal derivative basis functions ϕ_{2i+1} for $i = 0, \ldots, N$, giving a total of $2(N+1)$ degrees of freedom. These functions satisfy the interpolation conditions:

$$\phi_{2i}(\xi_j) = \delta_{ij}, \quad \phi'_{2i}(\xi_j) = 0, \quad \phi_{2i+1}(\xi_j) = 0, \quad \phi'_{2i+1}(\xi_j) = \delta_{ij}, \quad \forall i, j,$$

with $\delta_{i,j}$ representing the Kronecker delta function of two integres i, j defined as:

$$\delta_{ij} = \begin{cases} 1 & (i = j) \\ 0 & (i \neq j) \end{cases}.$$

Replacing u with u_h and v by an arbitrary function $\phi_j \in \mathcal{V}_D^h$ we arrived at the discretized formulation as:

$$\sum_{i=0}^{n_{\text{dof}}-1} c_i \int_\Omega \phi_i'' \phi_j'' dx = \int_\Omega q\phi_j dx, \quad j \in \mathcal{J}, \tag{6}$$

such that:

$$\sum_{i=0}^{n_{\text{dof}}-1} c_i \phi_i(x_k) = y_k, \quad \text{for } k \in \mathcal{E}, \tag{7}$$
$$\sum_{i=0}^{n_{\text{dof}}-1} c_i \phi_i(x_k) \leq y_k, \quad \text{for } k \in \mathcal{I}, \tag{8}$$

where $\mathcal{J}$ represent the set of indexes of basis functions $\phi_j \in \mathcal{V}_D^h$.

This can be written in matrix form as:

$$A\mathbf{x} = \mathbf{b}, \tag{9a}$$
$$C\mathbf{x} = \mathbf{d}, \tag{9b}$$
$$E\mathbf{x} \leq \mathbf{e}, \tag{9c}$$

with $\mathbf{x}$ is the vector of degrees of freedom of u_h. Here, the matrix A represents the corresponding stiffness matrix, which is symmetric and positive definite; $\mathbf{b}$ is the load vector. The constraint matrices C (equality) and E (inequality) consist of basis function values at the respective data locations. Since the basis functions possess local support and all data points are distinct, both C and E are guaranteed to have full row rank. As the boundary is of Dirichlet type the DOF $c_0, c_1, c_{n_{\text{dof}}-2}$ and $c_{n_{\text{dof}}-1}$ are specified in (9).

In some practical applications, the values or derivatives at the boundaries may be unspecified. If the boundary derivative values $u'(0)$ and $u'(L)$ are unknown, the corresponding degrees of freedom in the approximate solution u_h are c_1 and $c_{n_{\text{dof}}-1}$. These can then be treated as unknowns and estimated by solving the discrete system (9). Similarly, if the derivatives are known

but the boundary displacements $u(0)$ and $u(L)$ are unknown, the corresponding degrees of freedom c_0 and $c_{n_{\text{dof}}-2}$ can be estimated from the same system.

4 Constrained Quadratic Programming Approach

From the discretization of the continuous form, we arrive at a system of equations and inequalities (9). In general, this system is overdetermined and may also include inequality constraints. From the outset, our goal has been to construct a globally smooth (C^1) curve based on the concept of bending beams. By the nature of beam deflection, it is evident that at equilibrium a beam bends to minimize its total energy (5), comprising both internal and external contributions. In the discrete formulation, these are represented by $\frac{1}{2}\mathbf{x}^T A\mathbf{x}$ (internal energy) and $-\mathbf{x}^T\mathbf{b}$ (external energy), with the total energy given by:

$$J(\mathbf{x}) = \frac{1}{2}\mathbf{x}^T A\mathbf{x} - \mathbf{x}^T\mathbf{b}.$$

Consequently, we choose to solve the system using a constrained quadratic programming (QP) formulation:

$$\begin{aligned} \min_{\mathbf{x}} \quad & \frac{1}{2}\mathbf{x}^T A\mathbf{x} - \mathbf{b}^T\mathbf{x}, && \text{(10a)} \\ \text{subject to} \quad & C\mathbf{x} = \mathbf{d}, && \text{(10b)} \\ & E\mathbf{x} \leq \mathbf{e}. && \text{(10c)} \end{aligned}$$

This structure makes the problem a natural candidate for quadratic programming as the objective is quadratic (bending energy), ensuring smoothness,the equality constraints guarantee interpolation and exact boundary enforcement and the inequality constraints provide flexibility to incorporate additional physical or geometric requirements. Practically the quadratic programming problem is solved in Python using the cvxpy package with the OSQP solver, an operator splitting method designed for convex quadratic programs with linear equality and inequality constraints.

In particular, when $\mathcal{I} = \{\}$, i.e., with no inequality constraint, the problem (10) reduced to interpolation and has the lagrangian

$$\mathcal{L}(\mathbf{x}, \lambda) = \frac{1}{2}\mathbf{x}^T A\mathbf{x} - \mathbf{b}^T\mathbf{x} + \lambda^T(C\mathbf{x} - \mathbf{d}).$$

Using the first-order optimality condition on $\mathcal{L}$, i.e., $\frac{\partial \mathcal{L}}{\partial \mathbf{x}} = \frac{\partial \mathcal{L}}{\partial \lambda} = 0$, we have the normal equation, i.e. the Karush–Kuhn–Tucker (KKT) system, for quadratic programming problem:

$$\underbrace{\begin{bmatrix} A & C^T \\ C & 0 \end{bmatrix}}_{\mathbf{M}} \begin{bmatrix} \mathbf{x} \\ \boldsymbol{\lambda} \end{bmatrix} = \underbrace{\begin{bmatrix} \mathbf{b} \\ \mathbf{d} \end{bmatrix}}_{\mathbf{rhs}}. \qquad (11)$$

Existence of reconstructed curve:

Since the stiffness matrix A is symmetric positive definite, the objective function is strictly convex. The equality constraint matrix $C \in \mathbb{R}^{|\mathcal{E}| \times n_{\text{dof}}}$, from the local support nature of the basis functions and distinct data point locations, has full row rank. This implies that the linear map $C : \mathbb{R}^{n_{\text{dof}}} \to \mathbb{R}^{|\mathcal{E}|}$ is surjective. Consequently, for any prescribed right-hand side $\mathbf{d} \in \mathbb{R}^{|\mathcal{E}|}$, the constraint $C\mathbf{x} = \mathbf{d}$ defines a nonempty affine subspace, i.e., a feasible region.

Minimizing a strictly convex function over a nonempty affine set guarantees the existence and uniqueness of the minimizer $[\mathbf{x}, \boldsymbol{\lambda}]^T$. Equivalently, the associated KKT matrix (11) is nonsingular. Because the reconstructed curve u_h is obtained from $\mathbf{x}$ through a linear combination of the basis functions, the resulting curve is unique within the chosen approximation space. This establishes the well-posedness of the reconstruction step.

Dynamic Adaptation of the Method:

The method is able to update the solution incrementally when new data points are added. For example, if a single data point is added, this corresponds to a constraint of the form $C_{\text{new}}\mathbf{x} = \mathbf{d}_{\text{new}}$, resulting in the KKT system

$$\underbrace{\begin{bmatrix} A & C^T & C_{\text{new}}^T \\ C & 0 & 0 \\ C_{\text{new}} & 0 & 0 \end{bmatrix}}_{\mathbf{M}_{\text{new}}} \begin{bmatrix} \mathbf{x} \\ \boldsymbol{\lambda} \\ \boldsymbol{\lambda}_{\text{new}} \end{bmatrix} = \underbrace{\begin{bmatrix} \mathbf{b} \\ \mathbf{d} \\ \mathbf{d}_{\text{new}} \end{bmatrix}}_{\mathbf{rhs}_{\text{new}}}. \qquad (12)$$

The structure of $\mathbf{M}_{\text{new}}$ indicates that the system does not need to be rebuilt from scratch when a new data point is added. Instead, we append C_{new} to the original matrix $\mathbf{M}$ and $\mathbf{d}_{\text{new}}$ to the right-hand side vector. This makes the method dynamically updatable and significantly reduces computational cost.

Since the problem has a unique solution, it can be formally obtained as $\mathbf{M}_{\text{new}}^{-1}\mathbf{rhs}_{\text{new}}$. However, the computation of $\mathbf{M}_{\text{new}}^{-1}$ can be efficiently performed using the block matrix inverse formula:

$$\begin{aligned} \mathbf{M}_{\text{new}}^{-1} &= \begin{pmatrix} \mathbf{M} & B^T \\ B & 0 \end{pmatrix}^{-1}, \quad B = \begin{pmatrix} C_{\text{new}} & 0 \end{pmatrix}, \\ &= \begin{pmatrix} \mathbf{M}^{-1} - \mathbf{M}^{-1}B^T S^{-1} B\mathbf{M}^{-1} & \mathbf{M}^{-1}B^T S^{-1} \\ S^{-1}B\mathbf{M}^{-1} & -S^{-1} \end{pmatrix}, \\ S &= B\mathbf{M}^{-1}B^T. \end{aligned}$$

This expression is entirely in terms of the original inverse $\mathbf{M}^{-1}$ and the new constraint C_{new}. The Schur complement $S = B\mathbf{M}^{-1}B^T = C_{\text{new}}XC_{\text{new}}^T$, where X is the top-left block of $\mathbf{M}^{-1}$. The invertibility of S is guaranteed as long as the rows of C_{new} are linearly independent of the rows of C.

Let

$$\mathbf{V}_{\text{old}} = \begin{pmatrix} \mathbf{x}_{\text{old}} \\ \boldsymbol{\lambda}_{\text{old}} \end{pmatrix} = \mathbf{M}^{-1}\mathbf{rhs} = \begin{pmatrix} X & Y \\ Z & W \end{pmatrix} \mathbf{rhs},$$

be the solution of the original system (11). Then the solution of the updated system (12) can be expressed as

$$\boldsymbol{\lambda}_{\text{new}} = S^{-1}(C_{\text{new}}\mathbf{x}_{\text{old}} - \mathbf{d}_{\text{new}}), \tag{13a}$$

$$\mathbf{x} = \mathbf{x}_{\text{old}} - XC_{\text{new}}^{T}\boldsymbol{\lambda}_{\text{new}}, \tag{13b}$$

$$\boldsymbol{\lambda} = \boldsymbol{\lambda}_{\text{old}} - ZC_{\text{new}}^{T}\boldsymbol{\lambda}_{\text{new}}. \tag{13c}$$

The solution formula (13) has a recurrence-like structure: each time a new constraint is added, the updated solution is obtained from the previous solution plus a correction depending only on the new constraint. This allows the solution to be incrementally updated without re-solving the entire system, and sequential additions produce a chain of solutions that grow with the number of constraints.

5 Model Evaluation

The performance of the proposed method is evaluated using approaches, combining quantitative error metrics with qualitative assessment. To establish accuracy, we first validate the method against a known analytical function. This provides a benchmark for quantifying error through several metrics, including the L^2 norm for overall fit, the L^∞ norm for the maximum pointwise deviation, and the L^2 norm of the derivative error to assess smoothness and physical plausibility of the reconstructed curve. In addition, the normalized root mean square error (NRMSE) is employed for scale independent comparison.

In addition to these quantitative metrics, qualitative assessment is conducted by visually inspecting the reconstructed curves. This includes examining the ability of the method to accurately interpolate equality constraints, respect inequality bounds, maintain smoothness across the domain, and avoid spurious oscillations. Visual comparisons are also made between the reconstructed curves and classical interpolators, such as cubic splines, under both uniform and irregular sampling, as well as in the presence of small perturbations in the input data.

Formally, let f denote the exact function and g the reconstructed curve obtained using the proposed approach. The error function is defined as $e(x) = f(x) - g(x)$. The following metrics are considered to capture different aspects of the error, including function values, derivatives, and integral properties:

- **Normalized Root Mean Square Error (NRMSE):**

$$\text{NRMSE} = \frac{1}{f_{max} - f_{min}}\sqrt{\sum_{i=1}^{N}\frac{(f(\xi_i) - g(\xi_i))^2}{N}}.$$

- L^∞ **Norm of the Error (L^∞- Error):** Also known as the maximum error, it measures the largest pointwise deviation.

$$||e||_\infty = ||f - g||_\infty = \sup_{x\in[0,L]} |f(x) - g(x)|.$$

- L^2 **Norm of the Error (L^2-Error):** Measures the mean-squared difference between the two curves. Smaller values indicate a better overall fit.

$$||e||_2 = ||f - g||_2 = \sqrt{\int_0^L (f(x) - g(x))^2\, dx}.$$

- L^2 **Norm of the First Derivative Error:** Evaluates how well the slope of the reconstructed curve matches the slope of the exact curve.

$$||e'||_2 = ||f' - g'||_2 = \sqrt{\int_0^L (f'(x) - g'(x))^2\, dx}.$$

Beyond numerical accuracy, the robustness of the method is also examined. In cases where the exact function is unknown, stability is assessed by introducing small random perturbations to the input data and verifying that the reconstruction remains consistent. Furthermore, the method's performance can be systematically evaluated under different point distributions, including uniformly spaced, irregularly spaced, and clustered points. Finally, all reconstructions are subject to visual inspection to ensure physical plausibility and to confirm the absence of spurious oscillations.

Sensitivity analysis can also be performed for the problem (10) to examine how small perturbations in the measurement data $\mathbf{d}$ affect the solution $\mathbf{x}$. Let $\mathbf{x}^*$ be the optimal primal solution of the unperturbed problem, and let $\boldsymbol{\lambda}^*$ and $\boldsymbol{\mu}^*$ be the optimal dual multipliers for the equality and inequality constraints, respectively. Define the active set

$$\mathcal{A} = \{\, i : E_i\mathbf{x}^* = \mathbf{e}_i \,\},$$

where E_i and $\mathbf{e}_i$ denote the i^{th} row of the matrix E and the i^{th} entry of the vector $\mathbf{e}$, respectively.

Suppose a small perturbation $\Delta\mathbf{d}$ is applied to $\mathbf{d}$, and assume that the active set $\mathcal{A}$ remains unchanged. The corresponding perturbed solution becomes $\mathbf{x}^* + \Delta\mathbf{x}$, with dual multipliers $\boldsymbol{\lambda}^* + \Delta\boldsymbol{\lambda}$ and $\boldsymbol{\mu}^*_{\mathcal{A}} + \Delta\boldsymbol{\mu}_{\mathcal{A}}$. Subtracting the KKT systems of the perturbed and unperturbed problems yields the linearized system

$$\underbrace{\begin{pmatrix} A & C^T & E_{\mathcal{A}}^T \\ C & 0 & 0 \\ E_{\mathcal{A}} & 0 & 0 \end{pmatrix}}_{\mathbf{K}} \begin{pmatrix} \Delta\mathbf{x} \\ \Delta\boldsymbol{\lambda} \\ \Delta\boldsymbol{\mu}_{\mathcal{A}} \end{pmatrix} = \begin{pmatrix} \mathbf{0} \\ \Delta\mathbf{d} \\ \mathbf{0} \end{pmatrix}.$$

Thus,

$$\begin{pmatrix} \Delta\mathbf{x} \\ \Delta\boldsymbol{\lambda} \\ \Delta\boldsymbol{\mu}_{\mathcal{A}} \end{pmatrix} = \mathbf{K}^{-1}\begin{pmatrix} \mathbf{0} \\ \Delta\mathbf{d} \\ \mathbf{0} \end{pmatrix} = \begin{pmatrix} \mathbf{K}_{11} & \mathbf{K}_{12} & \mathbf{K}_{13} \\ \mathbf{K}_{21} & \mathbf{K}_{22} & \mathbf{K}_{23} \\ \mathbf{K}_{31} & \mathbf{K}_{32} & \mathbf{K}_{33} \end{pmatrix}\begin{pmatrix} \mathbf{0} \\ \Delta\mathbf{d} \\ \mathbf{0} \end{pmatrix},$$

and we obtain

$$\Delta \mathbf{x} = \mathbf{K}_{12}\, \Delta \mathbf{d} = J\, \Delta \mathbf{d}, \tag{14}$$

where $J = \frac{\partial \mathbf{x}^*}{\partial \mathbf{d}}$ is the Jacobian of the optimal solution with respect to the data $\mathbf{d}$.

From (14), we see that the perturbation in the solution is linearly related to the perturbation in the input data.

Let

$$G = \begin{pmatrix} C \\ E_{\mathcal{A}} \end{pmatrix}, \qquad S = -GA^{-1}G^T, \qquad S^{-1} = \begin{pmatrix} S_{11}^{-1} & S_{12}^{-1} \\ S_{21}^{-1} & S_{22}^{-1} \end{pmatrix}.$$

Then the sensitivity matrix J admits the explicit form

$$J = \begin{cases} A^{-1}C^T(CA^{-1}C^T)^{-1}, & \text{if } \mathcal{A} = \varnothing, \\ -A^{-1}\left(C^T S_{11}^{-1} + E_{\mathcal{A}}^T S_{21}^{-1}\right), & \text{otherwise.} \end{cases}$$

Using the linear relation (14), for a set of perturbations $\{\Delta \mathbf{d}^{(k)}\}_{k=1}^{K}$ and the resulting perturbations in the solution $\{\Delta \mathbf{x}^{(k)}\}_{k=1}^{K}$, we may compute the maximum deviation at each grid point, $\max_k |\Delta \mathbf{x}_i^{(k)}|$, the standard deviation $\sigma_x = \text{std}\{\Delta \mathbf{x}^{(k)}\}$, and visualize the corresponding 95% confidence interval about the optimal solution $\mathbf{x}^*$.

6 Results

In this section, we use the discrete biharmonic curve reconstruction method under a variety of scenarios. The results are organized to show the method's flexibility in handling different types of constraints and boundary conditions, as well as its accuracy compared to classical interpolation technique. For each of this result the lateral load q is chosen to be zero. We consider the following cases:

- Reconstruction with only equality constraints at the given data points, illustrating the ability of the method to exactly interpolate the known values.
- Reconstruction with both equality and inequality constraints at selected points, demonstrating the method's capability to enforce bounds on the solution.
- Validation of the method using data sampled from known analytical functions, to quantify the accuracy and robustness of the reconstructed curves.
- Observe the stability of the resulting curve reconstruction for small perturbation in the data points.

Imposed conditions

Reconstruction of a curve using the proposed method in the presence of equality and/or inequality conditions at data points and specified boundary condition.

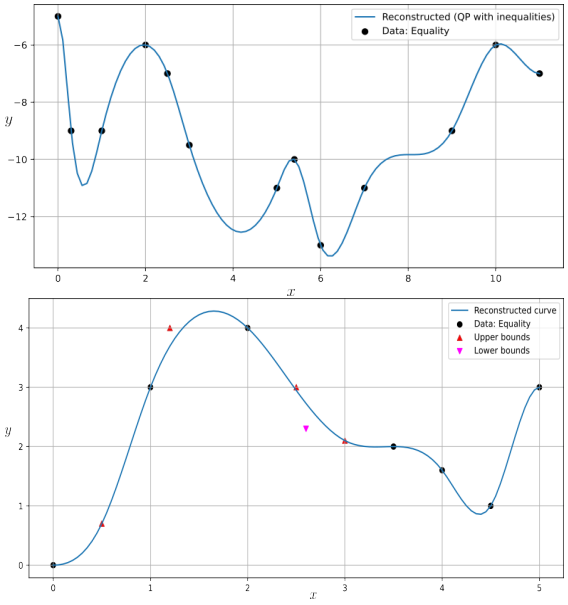

Figure 2: Plot of the curve reconstructed using the discrete biharmonic approach for the case of a randomly chosen data consisting of only equality conditions (*Left*) and for the case where data contain both equality, lower bound and upper bound at some locations (*Right*).

As shown in Fig.2, for the given set of synthetic data points and specified Dirichlet boundary conditions (DBCs), the proposed method generates a curve that passes through all interpolation points, satisfies the prescribed lower bound, upper bound constraint, and enforces known Dirichlet boundary conditions as expected. In particular, the reconstructed curve in Fig. (2, *Right*) the interpolation points are with coordinates $(x_{\text{data}}, y_{\text{data}}) = ([0,\ 1,\ 2,\ 3.5,\ 4,\ 4.5,\ 5],\ [0,\ 3,\ 4,\ 2,\ 1.6,\ 1,\ 3])$, the location of the upper bounds are at $x_{up} = [0.5, 1.2, 2.5, 3]$ with values $y_{up} = [0.7, 4, 3, 2.1]$, location and values for the lower bound is $x_{lb} = [2.6], y_{lb} = [2.3]$ and the derivates at the ends are zero.

For this data, the resulting curve has values $[0, 3, 4, 2, 1.6, 1, 3]$ at the interpolation, $[0.7, 3.63, 2.63, 1.65]$ at the upper bound locations and $[2.34]$ at lower bound. The results indicate the interpolation constraints are satisfied exactly. The reconstructed value at the lower bound location exceeds the required minimum of 2.3, and the values at the upper bound locations remain below or equal to the specified limits. This demonstrates that the method can simultaneously interpolate given data and honor inequality constraints, producing a curve that is both accurate and physically consistent.

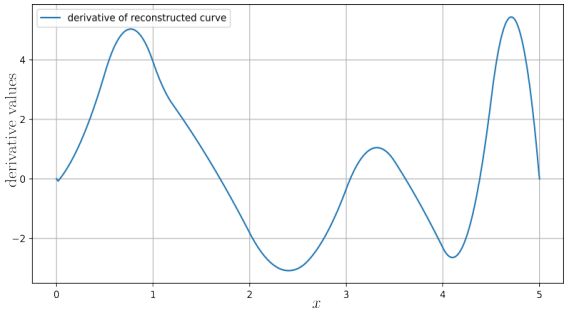

Figure 3: Plot of the derivative of the reconstructed curve(Fig: 2; *Right*)

In addition, the smoothness requirement is confirmed by examining the derivative of the reconstructed curve. As shown in Fig. 3, the derivative is continuous, indicating that the reconstructed curve possesses a continuous first derivative and therefore belongs to the class C^1. Moreover, the boundary derivative conditions, which are zero at both ends in this case, are also satisfied exactly, as evident from the figure.

In some practical applications, the endpoint derivatives are typically unknown leading to presence of unspecified Dirichlet boundary conditions. An estimate of these can be obtained from the solution of the discrete system.

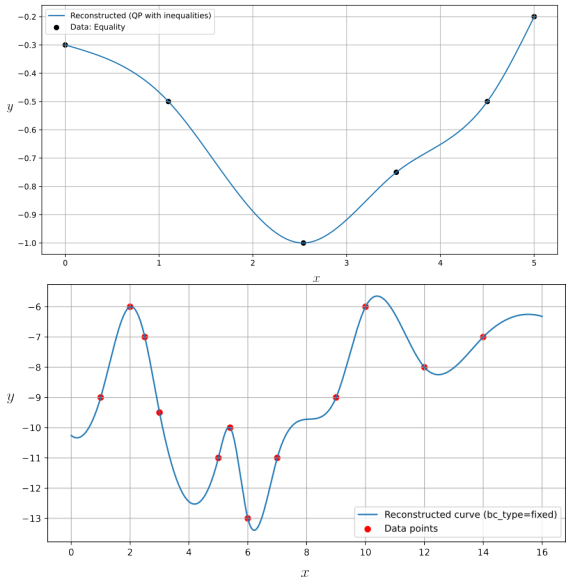

Figure 4: Reconstructed curve from a given set of data points where the endpoint derivatives(*Left*) and values(*Right*) are not prescribed and are instead estimated.

Performance of the proposed method

To assess the performance of the proposed method, data points are taken from known representative functions. For each case, visual comparison of the exact curve, the reconstruction produced by our method, and a standard *cubic spline* interpolator, are shown in Fig. 5. Data points are taken from a known function: $f(x) = \sin(x)$ with irregularly spaced points *Left* and Bessel function of the first kind of order zero $J_0(\sqrt{x})$ with regularly spaced points *Right*.

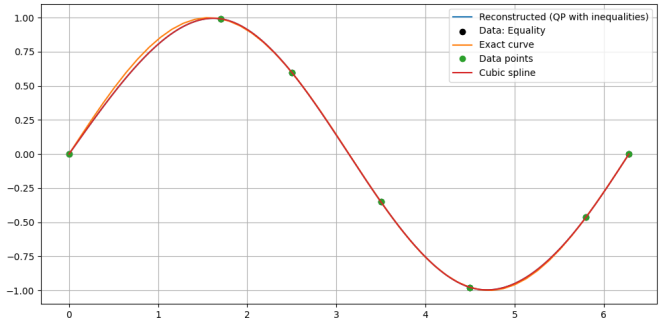

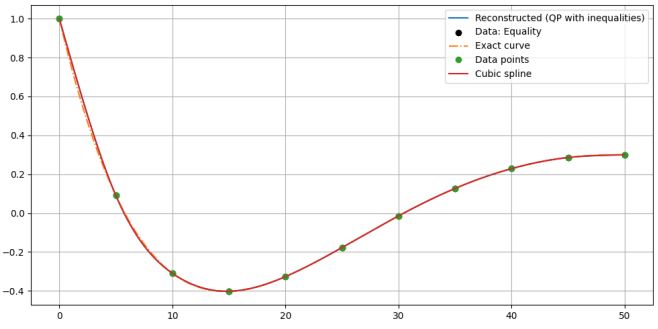

Figure 5: Visual comparison of the proposed method with the cubic spline.

Additional functions from different classes are selected to further evaluate the method, each representing a distinct curve behavior. For each function, performance metrics are computed using uniformly spaced data points, and the results are reported in Table 1. The trapezoidal rule was employed to approximate the integrals appearing in the matrices. The reported error norm values(maximum norm, L^2 norm of the error) can be normalized and interpreted as percentages relative to the range.

Stability

The influence of small perturbations in the input data on the reconstructed curve gives important indication of the stability of the proposed method. To examine this, we introduce random noise of small magnitude to the y-values of the sampled points and analyze the corresponding changes in the reconstructed curve. Both uniformly spaced and non uniformly spaced data points are considered to assess the method's resilience under different sampling patterns. In Fig. 6 and 7 data points are taken from the function $f(x) = \frac{1}{1+25x^2}$ and small perturbations are applied to the corresponding y_i's.

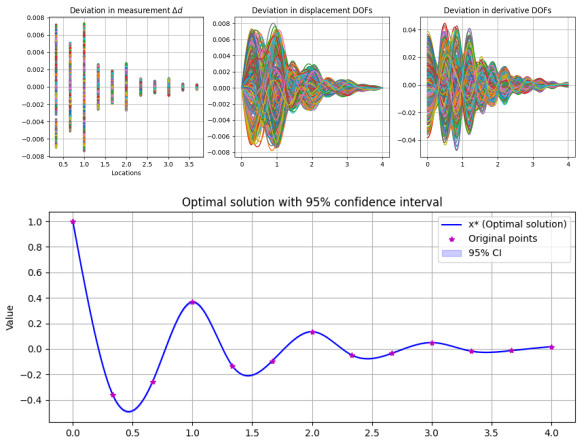

Figure 6: Effect of small perturbations Δd's on the reconstructed curve with 95% confidence interval: equally spaced points.

Table 1: Performance of the proposed approach for data points sampled uniformly from known analytic functions. Here, n denotes the number of data points.

f	L	n	Range(f)	NRMSE	$\|\|e\|\|_\infty$	$\|\|e\|\|_{L^2}$	$\|\|e'\|\|_{L^2}$
$J_0(\sqrt{x})$	50	11	1.403	0.006	0.038	0.060	0.10
$x^3 - 4x^2 + 3x$	3	10	2.744	0.006	0.054	0.029	0.30
$\sin(x)$	2π	7	2.000	0.007	0.010	0.036	0.07
$\frac{1}{1+25x^2}$	1	8	0.962	0.001	0.002	0.001	0.029
$e^{-x}\cos(2\pi x)$	4	13	1.614	0.011	0.060	0.036	0.35

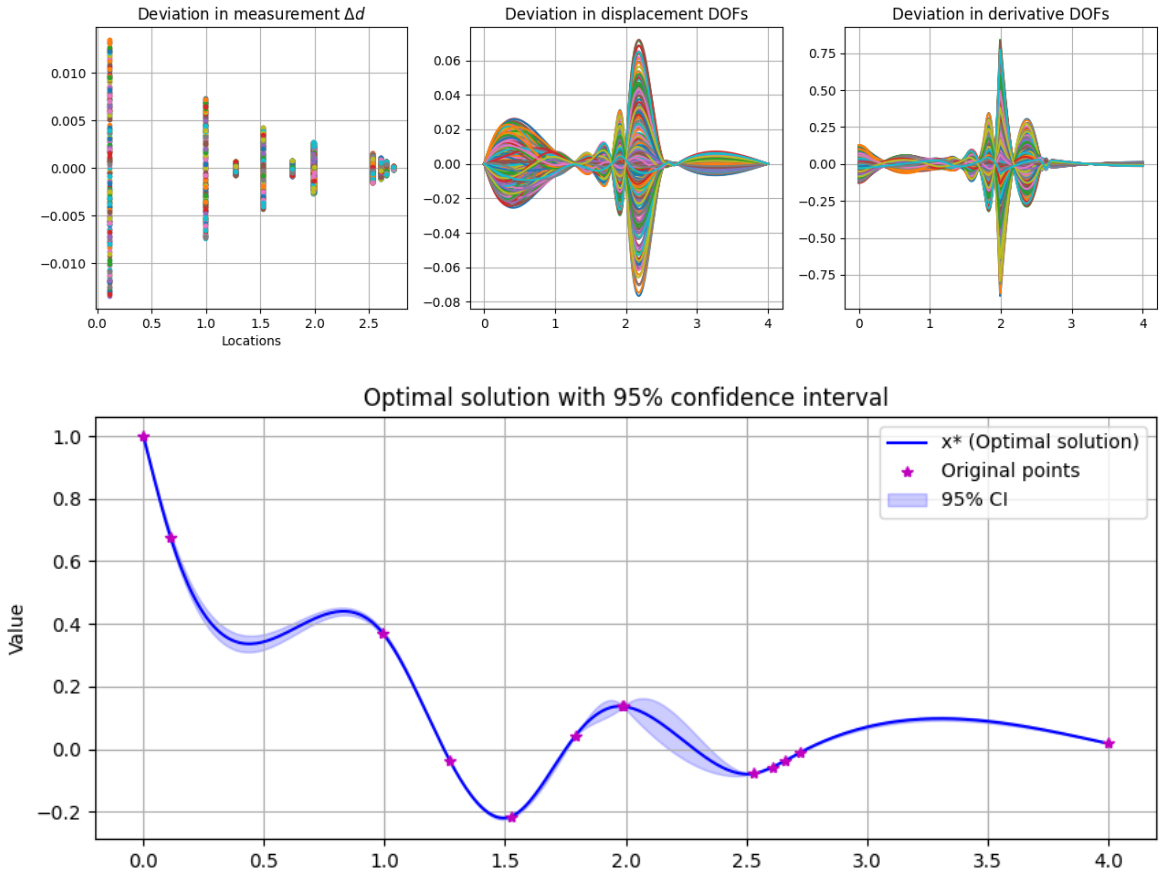

Figure 7: Effect of small perturbations in Δd's on the reconstructed curve with 95% confidence interval: unequally spaced points.

7 Discussion

An important aspect of the proposed method is its ability to flexibly accommodate different types of requirements while maintaining smoothness. *First*, it exactly interpolates through the equality data points, ensuring that the reconstructed curve honors all available information. *Second*, it is capable of satisfying inequality constraints, such as prescribed upper/lower bounds, demonstrating its ability in incorporating additional problem specific requirements. *Third*, the method consistently enforces the given boundary conditions, whether Dirichlet or Mixed, without having unnecessary oscillations near the boundaries.

Finally, by construction, the discrete biharmonic formulation produces curves that are not only honor conditions at the data points but also smooth, with continuity in the first derivative. This combination of physical interpretability, interpolation, constraint enforcement, boundary adherence and smoothness makes the approach well suited for practical applications where multiple conditions must be satisfied simultaneously.

From the NRMSE values in Table 1, we observe that the maximum deviation of the reconstructed curves from the exact functions is less than 1%. These results indicate that the proposed discrete biharmonic approach provides a robust and highly accurate method for curve reconstruction from the given data points. The consistently low NRMSE values (e.g., < 0.01) across diverse test functions demonstrate strong global fidelity, showing that the reconstructed curves are, on average, very close to the exact curves.

Furthermore, small L^∞ errors (e.g., < 0.06) provide evidence of local stability, confirming that no significant localized deviations or unwanted oscillations occur. This represents an

improvement over classical high order polynomial interpolation, which is known to suffer from instabilities such as the Runge's phenomenon.

The absolute error norms further demonstrate the accuracy of the proposed method. The L^2-errors remain small across all tested functions, with values ranging between 0.001 and 0.060, showing that the reconstructed curves are too close to the originals in terms of global shape. In contrast, the derivative errors are relatively larger (0.029–0.35). For instance, the oscillatory function $e^{-x}\cos(2\pi x)$ exhibits the highest derivative error (0.35), while smoother functions such as $\frac{1}{1+25x^2}$ yield much lower errors (0.029).

Further investigation in to the L^2 norm of the derivative of the proposed approach and the cubic interpolator over the same FEM grid shows that for the first three functions both methods have almost the same error values (L^2 norm of the value as well as derivative) where as for the last two cases the cubic spline has large error values of 2.10 and 1.135 respectively.

The robustness of the proposed method was further demonstrated through tests involving small perturbations to the input data. By adding random noise to the sampled points, we observed in Figs. 6, 7 that the largest deviation in the solution are 0.008 and 0.06 for the case of equally spaced and unequally spaced data points respectively. This shows the reconstructed curves remained very close to the one obtained from the unperturbed data.

The perturbation is introduced as follows. For each constraint d_j, the maximum error magnitude S_j is first set to 2% of its given value, that is, $S_j = 0.02\,|d_j|$. In this way, constraints with larger absolute values are allowed to have proportionally larger absolute errors.

In each trial k, the perturbation $\Delta d^{(k)}$ is generated by multiplying S elementwise by a random vector $\mathbf{r}$, where each component r_j is drawn independently from a uniform distribution over the interval $[-1, 1]$. Consequently, each entry of Δd (say Δd_j) lies within the range $[-S_j, S_j]$.

Table 2 quantifies this effect: across all considered functions, the maximum deviation (L_∞) is below 0.12, the mean absolute error (MAE) remains around 0.02–0.04, and the normalized RMSE (NRMSE) does not exceed 2.4%. This demonstrates that, rather than amplifying measurement errors, the discrete biharmonic formulation effectively smooths out minor fluctuations while preserving the global shape of the curve. Importantly, the absence of spurious oscillations in the perturbed reconstructions confirms that the method can reliably handle imperfect or noisy data, a feature that is crucial for practical applications where measurement errors are unavoidable.

Table 2: Maximum norm, MAE, and NRMSE for the deviation of the reconstructed curve from the original curve due to perturbations in the data values; uniformly spaced data points.

f	$\|\|\cdot\|\|_\infty$	MAE	NRMSE (%)
$J_0(\sqrt{x})$	0.04	0.02	1.49
$x^3 - 4x^2 + 3x$	0.12	0.04	2.03
$\sin(x)$	0.07	0.03	1.54
$\frac{1}{1+25x^2}$	0.04	0.02	2.39
$e^{-x}\cos(2\pi x)$	0.06	0.02	1.50

Comparison with some known methods:
To further validate the efficacy of the proposed biharmonic approach, we conducted a comparative analysis against well-established interpolation and regression methods, including Kriging, Radial Basis Function (RBF) interpolation, and Gaussian Process Regression (GPR).

Specifically, Kriging and GPR are rooted in stochastic processes and provide uncertainty quantification, while RBFs are deterministic kernel-based interpolators. Figure 8 illustrates the performance of these methods for data points sampled from a known analytic function, considering both uniformly and non-uniformly spaced sampling. A quantitative assessment of the performance metrics, based on the Mean Absolute Error (MAE), Root Mean Square Error (RMSE), and maximum error norms (L^∞), is provided in Table 3.

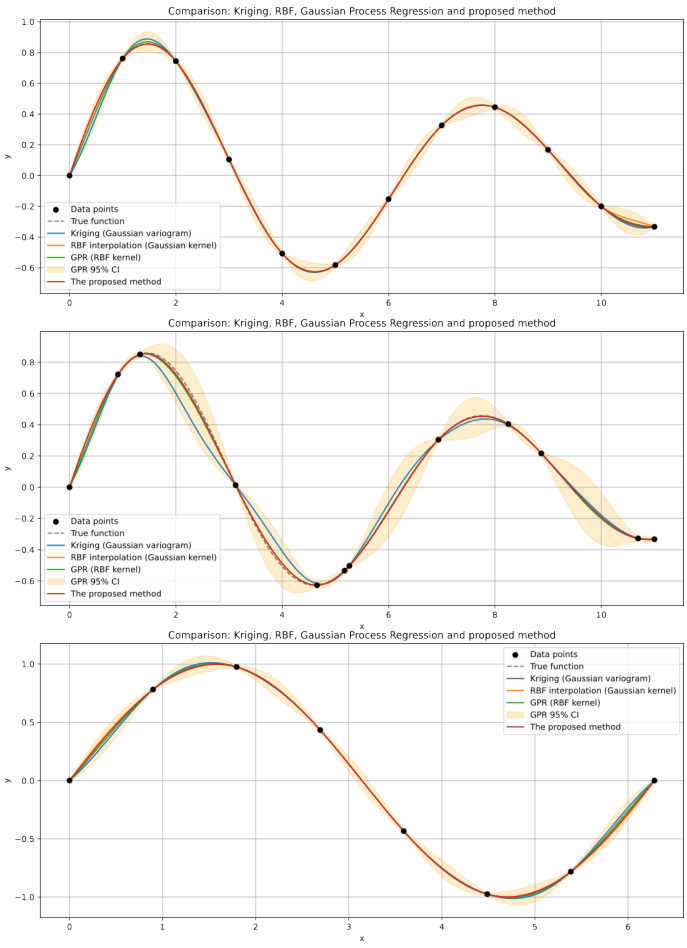

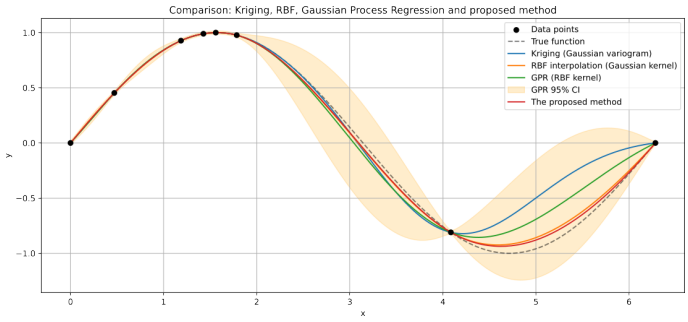

Figure 8: Comparison of the proposed approach in relation to kriging, radial basis function and gaussian process regression methods for points picked from $e^{-0.1x}\sin(x)$ (*Top*) and $\sin(x)$ (*Bottom*).

Effect of discretization size:

The effect of discretization size on the accuracy of the reconstructed curve is illustrated in Fig. 9 for the functions $e^{-0.1x}\sin(x)$ and $\sin(x)$, using uniformly spaced data points as summarized in Table 3. For both examples, the error metrics initially vary with mesh refinement but eventually reach a plateau, indicating that the solution becomes nearly independent of the discretization size. This flattening behavior demonstrates that the reconstruction method attains numerical stability beyond a certain resolution, and further mesh refinement yields negligible improvement in accuracy.

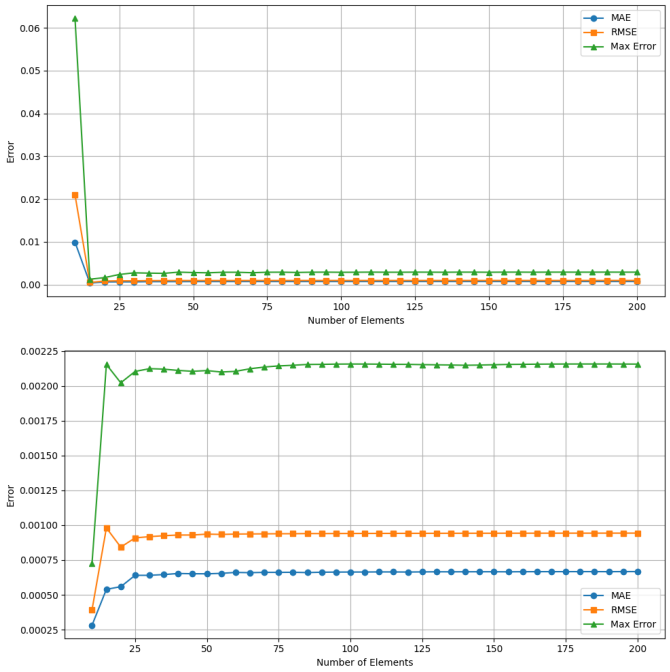

Figure 9: Effect of mesh density (step size) on the proposed curve reconstruction.

The conditioning of the discrete system was also examined for grids ranging from 10 to 200 elements. The condition number increased from approximately 10^3 on coarse meshes to around 10^7 on the finest mesh. This behavior is consistent with the theoretical properties differential operators, whose discretizations naturally become more ill-conditioned as the mesh is refined.

Despite these strengths, the accuracy of the proposed method depends strongly on the distribution and density of input data points. In sparsely sampled regions, the reconstructed curve may fail to capture local variations, while closely spaced points can induce localized oscillations due to strict enforcement of pointwise constraints. Being deterministic, the method does not account for data uncertainty or spatial correlations, which are often important in spatial interpolation to leverage information from neighboring observations.

Surface reconstruction case:

The scalability of the proposed approach to surface reconstruction is illustrated in Fig. 10 with homogeneous Dirichlet boundary condition and interior data point location [(0.3, 0.2), (0.2, 0.7), (0.7, 0.2), (0.8, 0.63), (0.5, 0.7), (0.45, 0.45), (0.52, 0.61)] and the corresponding z values [0.2, 0.1,-0.23, 0.32, -0.2, -0.15, 0.12]. The computational domain is discretized using the DUNE (Bastian et al., 2021) software, whereas the weak form of the governing equations is approximated using the Virtual Element Method (VEM) (Beirão da Veiga et al., 2013; Brezzi & Marini, 2013). The Figure shows both the projection of the reconstructed surface onto the xy-plane (left) and its three-dimensional representation (right). Moreover, this surface reconstruction approach has been applied to the estimation of bedrock topography, as presented in (Bekele et al., 2025), with additional results forthcoming.

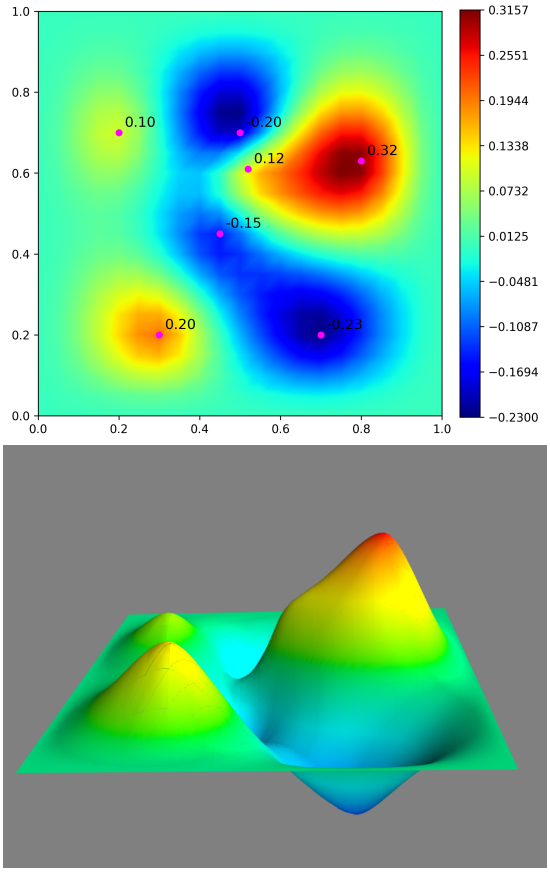

Figure 10: Surface reconstruction from a given set of data points using the extension of the proposed approach.

Table 3: Error comparison for the two functions under uniform and non-uniform sampling illustrated in Fig. 8.

Example	Data Type	Method	MAE	RMSE	Max Norm
Ex1: $\sin(x)e^{-0.1x}$ $x \in [0, 11]$	Uniform (12 pts)	Kriging	0.0086	0.0180	0.0778
		RBF	0.0031	0.0065	0.0294
		GPR	0.0040	0.0085	0.0370
		Proposed	0.0007	0.0010	0.0029
	Non-uniform	Kriging	0.0390	0.0583	0.1702
		RBF	0.0052	0.0088	0.0245
		GPR	0.0084	0.0140	0.0388
		Proposed	0.0058	0.0092	0.0251
Ex2: $\sin(x)$ $x \in [0, 2\pi]$	Uniform (8 pts)	Kriging	0.0141	0.0206	0.0509
		RBF	0.0034	0.0052	0.0127
		GPR	0.0058	0.0088	0.0223
		Proposed	0.0007	0.0009	0.0022
	Non-uniform	Kriging	0.1240	0.2113	0.5141
		RBF	0.0338	0.0470	0.1031
		GPR	0.0878	0.1305	0.2992
		Proposed	0.0262	0.0366	0.0793

8 Conclusion

In this paper, we introduce a method for reconstructing curves based on a discrete version of the biharmonic equation. Our approach generates globally C^1 smooth curves that adapt naturally to various types of data and boundary conditions. It interpolates exact measurements while also enforcing inequality constraints, such as prescribed upper and lower bounds. Through experiments with both uniform and irregular data distributions, we found that the method consistently produces stable, oscillation free curves. This is particularly valuable in practical scenarios, where data are often sparse, noisy, or unevenly sampled. In addition, the method is flexible in handling both Dirichlet and Mixed boundary conditions.

Another significant strength lies in its physical interpretability: the biharmonic equation mimics the behavior of thin elastic beams or plates, providing an intuitive link between mathematical smoothness and physical phenomena.

Finally, the method naturally extends to higher dimensions, offering promise for applications such as surface reconstruction in geosciences, including bedrock topography estimation. Overall, this demonstrates the broader potential of the approach and opens pathways for future work, including integration of additional data sources and uncertainty quantification.

Acknowledgments

The authors would like to thank the Editor-in-Chief and the anonymous reviewers for their insightful comments and constructive suggestions, which significantly enhanced the clarity, rigor, and readability of this manuscript.

Conflict of Interest

The authors declare that they have no competing financial interests or personal relationships that could have influenced the work reported in this paper.

Funding

The authors did not receive any funding for this research.

References

Bastian, P., Blatt, M., Dedner, A., Dreier, N.-A., Engwer, C., Fritze, R., Gräser, C., Grüninger, C., Kempf, D., Klöfkorn, R., et al. (2021). The dune framework: Basic concepts and recent developments. *Computers & Mathematics with Applications*, *81*, 75–112.

Beirão da Veiga, L., Brezzi, F., Cangiani, A., Manzini, G., Marini, L. D., & Russo, A. (2013). Basic principles of virtual element methods. *Mathematical Models and Methods in Applied Sciences*, *23*(01), 199–214.

Bekele, S. S., Wolde, M. M., Führer, C., Kitterød, N.-O., & Kværnø, A. (2025). Modeling a smooth surface by a constrained biharmonic equation with application in soil science. https://arxiv.org/abs/2510.23195

Brezzi, F., & Marini, L. D. (2013). Virtual element methods for plate bending problems. *Computer Methods in Applied Mechanics and Engineering*, *253*, 455–462.

Chiles, J.-P., & Delfiner, P. (2012). *Geostatistics: Modeling spatial uncertainty*. John Wiley & Sons.

Cressie, N. (1993). *Statistics for spatial data*. Wiley.

de Boor, C. (2001). *A practical guide to splines* (3rd). Springer-Verlag.

Farin, G. (2002). *Curves and surfaces for cagd: A practical guide*. Morgan Kaufmann.

Gavin, H. P. (2014). Example of the principle of minimum total potential energy. *CEE 201L. Duke U*.

Hoffman, J. D., & Frankel, S. (2018). *Numerical methods for engineers and scientists*. CRC Press.

Journel, A. G., & Huijbregts, C. J. (1978). *Mining geostatistics*. Academic Press.

Kitterød, N.-O. (2017). Estimating unconsolidated sediment cover thickness by using the horizontal distance to a bedrock outcrop as secondary information. *Hydrology and Earth System Sciences*, *21*(8), 4195–4211.

Kitterød, N.-O., & Leblois, É. (2019). Modelling bedrock topography. *Earth Surface Dynamics Discussions*, 1–36.

Kitterød, N.-O., & Leblois, É. (2021). Estimation of sediment thickness by solving poisson's equation with bedrock outcrops as boundary conditions. *Hydrology Research*, *52*(3), 597–619.

Larson, M. G., & Bengzon, F. (2013). *The finite element method: Theory, implementation, and applications* (Vol. 10). Springer Science & Business Media.

Li, J., & Heap, A. D. (2008). A review of spatial interpolation methods for environmental scientists.

Mazarguil, A., Oudre, L., & Vayatis, N. (2022). Non-smooth interpolation of graph signals. *Signal processing*, *196*, 108480.

Ottosen, N., & Petersson, H. (1991, March). *Introduction to the finite element method* (2nd ed.). Division of Structural Mechanics, LTH.

Phillips, G. M. (2003). *Interpolation and approximation by polynomials* (Vol. 14). Springer Science & Business Media.

Piegl, L., & Tiller, W. (2012). *The nurbs book*. Springer Science & Business Media.

Quarteroni, A. (2009). *Numerical models for differential problems*. Springer.

Schumaker, L. L. (2007). *Spline functions: Basic theory* (3rd). Cambridge University Press.

Szilard, R. (2004). Theories and applications of plate analysis: Classical, numerical and engineering methods. *Appl. Mech. Rev.*, *57*(6), B32–B33.

Xu, Y., & Xu, R. (2022). Research on interpolation and data fitting: Basis and applications. *arXiv preprint arXiv:2208.11825*.

Zarowski, C. J. (2004). *An introduction to numerical analysis for electrical and computer engineers*. John Wiley & Sons.

East African Journal of Biophysical and Computational Sciences
ISSN (Online): 2789-3618 and ISSN (Print): 2789-360X

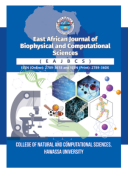

Journal Information

Volume 6(2), 2025
DOI: https://dx.doi.org/10.4314/eajbcs.v6i2.2S

Homepage:
https://journals.hu.edu.et/hu-journals/index.php/eajbcs

Article History

Received: 13 October, 2025
Accepted: 21 November, 2025
Published Online: 25 December, 2025

How to cite

Wolde et al. (2025). Biharmonic Trend Modeling with Sequential Gaussian Simulation for Geospatial Estimation of Soil Thickness. *East African Journal of Biophysical and Computational Sciences* Volume 6(2), 2025, 14-24

ARTICLE

Biharmonic Trend Modeling with Sequential Gaussian Simulation for Geospatial Estimation of Soil Thickness

Maregnesh Mechal Wolde[1,*], Zerihun Kinfe Birhanu[1], Nils-Otto Kitterød[2]

[1]Department of Mathematics, Hawassa University, Ethiopia.
[2] Soil and Water Science Section, Norwegian University of Life Sciences (NMBU), Ås, Norway

*Corresponding author: beharmech@gmail.com

Abstract

An integrated approach for soil thickness estimation is developed and evaluated. The method combines a biharmonic trend model with a stochastic Sequential Gaussian Simulation (SGS) component. Numerical experiments are first carried out in one dimentional synthetic data to provide a controlled enviroment for testing the methodology, investigating interpolation behavior, and determining parameter sensitivity. The approch is then extended to a two dimensional synthetic domain to see how well it captures spatial variability that is more representative of real-world applications. In both settings, the large-scale structure of the soil thickness field is approximated using a biharmonic equation, while the small-scale variability is represented by SGS applied to the residuals. This decomposition enables the method to preserve global smoothness imposed by the PDE model while simultaneously reproducing local heterogeneity through stochastic simulation. The results demonstrate that the hybrid method reduces prediction error relative to the PDE model or ordinary kriging alone, and that it provides a flexible approach for uncertainity quantification, making it suitable for realistic soil thickness mapping problems. .

Keywords: Soil thickness; Biharmonic PDE; Sequential Gaussian Simulation; Uncertainty .

1 Introduction

Soil thickness is an important variable in hydrological, ecological, and geo-engineering applications (Liu et al., 2013; Yan et al., 2021). Its estimation remains difficult because field observations are typically sparse, the terrain may vary rapidly, and measurements often contain noise. A recent study by Kitterød and Leblois (2021) introduced a Poisson's equation with a constant-curvature assumption. Although this formulation provides a useful representation of large-scale behaviour, the imposed curvature is restrictive and may not reflect the spatial variability observed in natural landscapes. Kitterød and Leblois (2021) assumed that large-scale sediment thickness and bedrock topography might be modeled as parabolic functions resembling the U-shaped forms common in glacial landscapes. Solution of the Poisson's equations are sensitive to boundary conditions, which makes it less realistic when boundary information is

uncertain. Stochastic methods, such as Sequential Gaussian Simulation (SGS), have been used to represent small-scale variability and quantify uncertainty. For example, Jamshidi et al. (2014) applied SGS to investigate soil erodibility at the catchment scale, demonstrating its ability to reproduce local heterogeneity and provide multiple realizations for uncertainty analysis. However, SGS depends on the choice of variogram model and does not incorporate physical constraints, which may reduce simulation results outside data clusters. These considerations motivate a combined approach. PDE-based methods provide physically consistent large-scale trends but are limited to account uncertainity, whereas SGS capture local variability but lack physical structure. A hybrid strategy can take advantage of both.

The objective of this study is to develop and assess a hybrid PDE-SGS approach for soil thickness estimation. The large-scale trend is modeled using a thin-plate biharmonic equation, a classical fourth-order elliptic PDE widely used for generating smooth surfaces and plate-bending approximations (Antonietti et al., 2018; Gazzola et al., 2010; Kumar, 2024; Timoshenko & Woinowsky-Krieger, 1959). In our formulation, the biharmonic operator is driven by data-informed load functions, allowing spatially varying curvature that adapts to the underlying terrain structure (Brenner & Scott, 2008). Small-scale variability is represented by applying SGS to the residual field, ensuring that stochastic fluctuations are consistent with the estimated spatial covariance model. The method is first tested in a controlled one-dimensional synthetic example where the exact solution is known, allowing a direct comparison between the numerical results and the exact solution. This environment enables a transparent presentation of the mathematical formulation and provides a direct means of verifying the finite element implementation of the biharmonic trend (Beirão da Veiga et al., 2013; Chinosi & Marini, 2006). Synthetic noise is introduced to mimic measurement uncertainty and to evaluate the reliability of the approach under realistic data conditions. The trend component is represented through a set of biharmonic basis functions whose coefficients are estimated from the data, while the SGS component generates multiple realizations that reproduce small-scale spatial structure. Predictive accuracy and uncertainty are assessed through resampling strategies, including leave-one-out cross-validation. The main contributions of this paper are:

1. construction of the soil-thickness trend using a biharmonic equation whose load functions are calculated directly from the observations,
2. incorporation of variability and uncertainty through Sequential Gaussian Simulation (SGS),
3. demonstration of the method's behaviour under sparse and noisy observations, and
4. development of a finite element implementation for the one-dimensional model.

Below, the general idea is outlined in Section 2, followed by an example of a one-dimensional solution in Section 3. The PDE-SGS procedure is presented in Section 4, while the finite element implementation is summarized in Section 5. Numerical results are provided in Section 6, and the discussion and conclusions are given in Sections 7 and 8.

2 Methodology

The method we propose combines PDE-based trend modelling with stochastic simulations. The proposed approach includes:

1. A PDE trend using the biharmonic operator to capture large-scale smooth trends in soil thickness.
2. A stochastic simulation component using Sequential Gaussian Simulation to model small-scale variability and uncertainty.

The hybrid solution is expressed as:

$$\mathbb{U}(x) = T(x) + R(x), \tag{1}$$

where $T(x)$ represents the ensemble realization of the trend obtained by solving a constrained biharmonic equation, and $R(x)$ represents the stochastic residual simulated using SGS.

3 Mathematics Formulation

We consider the following problem on a closed domain $\Omega \subset \mathbb{R}^n$:

$$\Delta^2 u = q \ \text{ in } \ \Omega \tag{2a}$$

with boundary conditions:

$$u = 0 \quad \text{and} \quad \partial_n u = 0 \quad \text{on } \partial\Omega_{\mathrm{D}}, \tag{2b}$$

$$\Delta u = 0 \quad \text{and} \quad \partial_n(\Delta u) = 0 \quad \text{on } \partial\Omega_{\mathrm{N}}. \tag{2c}$$

The boundary $\partial\Omega = \partial\Omega_{\mathrm{D}} \cup \partial\Omega_{\mathrm{N}}$ is divided into a part $\partial\Omega_{\mathrm{D}}$ for Dirichlet boundary conditions and another $\partial\Omega_{\mathrm{N}}$ for Neumann boundary conditions. The right hand side function q will be referred to as the load function.

3.1 One-Dimensional Mathematical Formulation

We consider the one-dimensional case as a special instance of the general n-dimensional formulation in Sec. 3 with $n = 1$, i.e., the domain is $\Omega = [0, L]$. In this setting, the biharmonic equation (2a) - (2c) simplifies to

$$\frac{d^4 u(x)}{dx^4} = q(x), \quad x \in \Omega, \tag{3a}$$

subject to homogeneous Dirichlet boundary conditions at the end points:

$$u(0) = 0, \qquad u(L) = 0, \tag{3b}$$

$$u'(0) = 0, \qquad u'(L) = 0, \tag{3c}$$

where the prime ($'$) denotes differentiation with respect to x. The load function $q(x)$ is expressed as:

$$q(x) = \sum_{i=1}^{n_d} p_i q_i(x), \tag{3d}$$

where $q_i(x)$ are chosen load functions, p_i are unknown coefficients, and n_d is the number of basis functions (data points).

3.1.1 Variational (Weak) Formulation

Let V denote the function space that incorporates the essential (Dirichlet) boundary conditions of the problem:

$$V = \{\, v \in H^2(\Omega) \mid v(0) = v(L) = 0,\ v'(0) = v'(L) = 0 \,\}.$$

Functions in V therefore satisfy both the prescribed values and prescribed slopes at the boundary. To derive the weak formulation, we multiply (3a) by a test function $v \in V$ and integrate over the domain. Applying integration by parts twice and using the fact that both v and v' vanish at the boundaries yields the following weak problem:

Find $u \in V$ such that

$$\int_\Omega u''(x)\, v''(x)\, dx = \int_\Omega q(x)\, v(x)\, dx \quad \forall\, v \in V. \tag{4}$$

3.1.2 Discretization

To approximate the solution of the biharmonic (beam) problem, we employ the finite element method (FEM). The domain $[0, L]$ is partitioned into N uniform elements, with mesh points

$$0 = x_0 < x_1 < \cdots < x_N = L,$$

where $h = x_{i+1} - x_i$ denotes the uniform element length.

3.1.3 Basis functions: cubic Hermite polynomials

Since the Euler-Bernoulli beam equation involves both displacement and slope as nodal degrees of freedom, each element requires four degrees of freedom: $u(0), u'(0), u(h)$, and $u'(h)$. Accordingly, we adopt cubic Hermite polynomials as basis functions. This ensures C^1 continuity across elements, which are standard for fourth-order PDEs. On a reference element of length h, the beam profile is approximated as

$$u(x) = N_1^e u_1^e + N_2^e u_2^e + N_3^e u_3^e + N_4^e u_4^e,$$

where u_1^e, u_2^e are the displacement and slope at the left node, and u_3^e, u_4^e correspond to the right node. The cubic Hermite shape functions are given by

$$N_1^e = 1 - 3\frac{x^2}{h^2} + 2\frac{x^3}{h^3}, \qquad N_3^e = \frac{x^2}{h^2}\left(3 - 2\frac{x}{h}\right),$$
$$N_2^e = x\left(1 - 2\frac{x}{h} + \frac{x^2}{h^2}\right), \qquad N_4^e = \frac{x^2}{h}\left(\frac{x}{h} - 1\right).$$

The global finite element space $\mathbb{V}_h$ is formed by assembling these local Hermite basis functions over all elements. Imposing the clamped boundary conditions $u(0) = u(L) = 0$ and $u'(0) = u'(L) = 0$ sets the corresponding end functions to zero.

3.1.4 Discrete weak form

The approximate solution is expressed as

$$u_h(x) = \sum_{i=0}^{2N+1} c_i \phi_i(x),$$

with unknown coefficients c_i determined from the discrete weak form

$$a(u_h, \phi_j) = F(\phi_j), \qquad j = 0, 1, \ldots, 2N+1.$$

This leads to the linear system

$$\mathbf{K}_h \mathbf{U}_h = \mathbf{Q}_h,$$

where

$$(\mathbf{K}_h)_{ij} = \int_0^L \phi_i''(x)\, \phi_j''(x)\, dx, \qquad (\mathbf{Q}_h)_j = \int_0^L f(x)\, \phi_j(x)\, dx.$$

Here $\mathbf{K}_h$ and $\mathbf{Q}_h$ denote the stiffness matrix and load vector, respectively. Solving for $\mathbf{U}_h$ yields the finite element approximation $u_h(x)$.

3.2 Determination of Load Coefficients

To determine the unknown coefficients p_i, we enforce interpolation at the known data points (ξ_i, d_i):

$$u(\xi_i) = \sum_{j=1}^{n_d} p_j u_j(\xi_i) + u_{bc}(\xi_i) = d_i, \quad i = 1, \ldots, n_d. \tag{5}$$

This results in a linear system:

$$\underbrace{\begin{bmatrix} u_1(\xi_1) & u_2(\xi_1) & \cdots & u_{n_d}(\xi_1) \\ u_1(\xi_2) & u_2(\xi_2) & \cdots & u_{n_d}(\xi_2) \\ \vdots & \vdots & \ddots & \vdots \\ u_1(\xi_{n_d}) & u_2(\xi_{n_d}) & \cdots & u_{n_d}(\xi_{n_d}) \end{bmatrix}}_{A} \underbrace{\begin{bmatrix} p_1 \\ p_2 \\ \vdots \\ p_{n_d} \end{bmatrix}}_{P} = \underbrace{\begin{bmatrix} d_1 \\ d_2 \\ \vdots \\ d_{n_d} \end{bmatrix} - \begin{bmatrix} u_{bc}(\xi_1) \\ u_{bc}(\xi_2) \\ \vdots \\ u_{bc}(\xi_{n_d}) \end{bmatrix}}_{D},$$

$$AP = D. \tag{6}$$

Upon solving (6), the load coefficients p_i are obtained. The PDE solution with n_d data points $\{(\xi_i, d_i)\}_{i=1}^{n_d}$ is then reconstructed as

$$u(x) = \sum_{i=1}^{n_d} p_i\, u_i(x) + u_{bc}(x), \tag{7}$$

where u_i be the solutions of the biharmonic equations $\Delta^2 u_i = q_i$ with homogeneous Dirichlet boundary conditions for each of the load basis functions q_i, $i = 1, \ldots, n_q$. $u_{bc}(x)$ satisfies the boundary conditions alone.

4 Method Integration (PDE-SGS)

This section presents the combined approach that integrates the PDE-based trend reconstruction with Sequential Gaussian Simulation. The trend component is first estimated using the biharmonic PDE model, and its uncertainty is assessed through a leave-one-out cross-validation procedure. The resulting trend variance is then incorporated into the SGS algorithm to ensure that both spatial correlation and trend uncertainty are represented in the final realization. The overall approach yields spatial fields that honor the observed ata, the physical smoothness constraints enforced by the PDE, and the stochastic variability modeled through SGS.

4.1 Variance in the Trend Surface

To assess the uncertainty of the reconstructed trend, we employ a leave-one-out (LOO) analysis. At each iteration, one data point is removed, the trend surface is recomputed, and the excluded location is predicted. This procedure quantifies the sensitivity of the model to individual observations.

Formally, the ensemble of trend realizations is given by

$$T(x) = \{u^{(j)}(x)\}_{j=1}^{N_{\text{LOO}}}, \tag{8}$$

where $u^{(j)}(x)$, $j = 1, \ldots, N_{\text{LOO}}$, denotes the surface obtained by excluding the j^{th} point.

The mean trend surface is defined as

$$\bar{u}(x) = \frac{1}{N_{\text{LOO}}} \sum_{j=1}^{N_{\text{LOO}}} u^{(j)}(x), \tag{9}$$

and the corresponding variance is

$$\sigma_T^2(x) = \frac{1}{N_{\text{LOO}} - 1} \sum_{j=1}^{N_{\text{LOO}}} \left(u^{(j)}(x) - \bar{u}(x)\right)^2. \tag{10}$$

Thus, as a result, $T(x)$ in (1) can be replaced by the mean trend $\bar{u}(x)$, and the expression can be rewritten as

$$U(x) = \bar{u}(x) + R(x).$$

Residuals are then defined as

$$r_i = d_i - \bar{u}(\xi_i), \quad i = 1, \ldots, n_d. \tag{11}$$

4.2 Sequential Gaussian Simulation (SGS)

Once the trend component has been obtained, the residuals (11) are treated as a stochastic field and modeled using Sequential Gaussian Simulation. SGS generates multiple equally probable realizations of a spatial variable that respect both the observed values and their spatial correlation structure (Deutsch & Journel, 1992; Gómez-Hernández & Srivastava, 2021). The variogram is the key input that characterizes this spatial dependence. In this work, an exponential variogram model is employed,

$$\gamma(h) = c_0 + c_1 \left(1 - \exp\left(\beta \left(\frac{h}{h_a}\right)^2\right)\right), \tag{12}$$

where c_0 is the nugget, c_1 the partial sill, h_a the range, and $\beta = -\log(20)$, a commonly used shape parameter in geostatistical modeling, which determines the variance when $h = h_a$, and therefore is called the practical range. This model is chosen because it is flexible and widely used in practice. The estimated variogram parameters, reported in Section 6, are then used to simulate the residual field. SGS is carried out on a discretized grid of the domain. At each simulation step a grid node ξ_k is chosen at random from the unsimulated set. For the first unsampled location $x^* = \xi^*_{\kappa(1)}$, the conditioning data consist solely of the observed residuals,

$$\hat{\mathcal{C}}_0 = \{(\xi_i, r_i)\}_{i=1}^{n_d}.$$

Using ordinary kriging, the estimation at this location is expressed as

$$z_{OK}(x^*) = \sum_{i=1}^{n_d} \omega_i r_i, \tag{13}$$

subject to the unbiasedness constraint

$$\sum_{i=1}^{n_d} \omega_i = 1,$$

where ω_i denotes the kriging weight assigned to the i^{th} observation (Webster & Oliver, 2007). The weights are obtained by solving the linear system

$$\mathbf{Cov} \cdot \vec{x} = \mathbf{C}_{e,o},$$

where **Cov** is the covariance matrix of the observation points, $\mathbf{C}_{e,o}$ represents the covariance between the observations and the estimation point, and $\vec{x}$ contains the kriging weights and Lagrange multiplier. At x^*, the kriging mean $\mu(x^*) = z_{OK}(x^*)$ and the kriging variance $\sigma_R^2(x^*)$ are combined with the variance from the LOO-based trend surfaces, $\sigma_T^2(x^*)$ (10), to account for trend uncertainty. A simulated value is then drawn as

$$R(x^*) \sim \mathcal{N}\big(\mu(x^*),\, \sigma_R^2(x^*) + \sigma_T^2(x^*)\big).$$

This simulated value is appended to the conditioning set, and the procedure is repeated for the next unsimulated location along the random path. The process continues until all grid nodes are simulated, resulting in one complete realization of the residual field.

4.3 Final Reconstruction

The final realization is obtained by adding the PDE-based trend to the simulated residual field:

$$\mathbb{U}(x) = \bar{u}(x) + R(x). \tag{14}$$

Repeating this process with different random paths and draws (e.g., $K = 100$) yields an ensemble of realizations. These realizations reproduce both the large-scale PDE-based trend structure and the small-scale stochastic variability while honoring the observed data.

5 Implementation

The computational workflow is organized into three main stages: (i) verification of the finite element solver by comparison with a problem that admits an exact solution, (ii) estimation of the trend through a biharmonic formulation discretized by finite elements, and (iii) stochastic modeling of the residual component using sequential Gaussian simulation (SGS).

5.1 Computing the Biharmonic Equation Analytically

Before applying the method to synthetic data, we verify the finite element implementation against a biharmonic problem that admits a closed-form analytical solution. Such verification is standard practice in numerical analysis and finite element development (Braess, 2007; Brenner & Scott, 2008). The one-dimensional biharmonic equation corresponds to the classical clamped Euler-Bernoulli beam equation (Szabó & Babuška, 2021; Timoshenko & Goodier, 1951):

$$u^{(4)}(x) = 1, \qquad x \in [0, L], \tag{15a}$$

with clamped boundary conditions

$$u(0) = u(L) = 0, \qquad u'(0) = u'(L) = 0. \tag{15b}$$

Integrating (15a) four times yields

$$u(x) = \tfrac{1}{24}x^4 + Ax^3 + Bx^2 + Cx + D.$$

Imposing the clamped conditions (15b) at $x = 0$ gives $C = D = 0$. The remaining conditions $u(L) = 0$ and $u'(L) = 0$ lead to

$$\begin{aligned} \tfrac{1}{24}L^4 + AL^3 + BL^2 &= 0, \\ \tfrac{1}{6}L^3 + 3AL^2 + 2BL &= 0. \end{aligned}$$

Solving this system yields

$$A = -\tfrac{L}{12}, \qquad B = \tfrac{L^2}{24}.$$

Thus, the exact analytical solution is

$$u_{\text{exact}}(x) = \tfrac{1}{24}x^4 - \tfrac{L}{12}x^3 + \tfrac{L^2}{24}x^2, \tag{16}$$

which is the unique polynomial satisfying the biharmonic operator and clamped boundary conditions (Timoshenko & Goodier, 1951). To evaluate the accuracy of the finite element approximation u_h, we compute the discrete maximum and L^2 norms of the error at the computational nodes x_j:

$$\|e\|_\infty = \max_j \left|u_{\text{exact}}(x_j) - u_h(x_j)\right|, \tag{17a}$$

$$\|e\|_2 \approx \left(\sum_j \left|u_{\text{exact}}(x_j) - u_h(x_j)\right|^2 \Delta x_j\right)^{1/2}. \tag{17b}$$

These metrics allow us to compare numerical results with the analytical solution and to verify the expected convergence behavior of the biharmonic finite element discretization (Braess, 2007; Brenner & Scott, 2008).

5.2 One-Dimensional Biharmonic Trend Estimation

We model the trend as the solution of a biharmonic boundary value problem on the interval $\Omega = [0, L]$, with clamped boundary conditions (3b) and (3c). The weak form (4) is discretized using cubic Hermite shape functions on a uniform mesh of N elements. The resulting stiffness matrix denoted by $\mathbf{K}_h$: $\mathbf{K}_h \in \mathbb{R}^{2(N+1)\times 2(N+1)}$ corresponds to the finite element discretization of the biharmonic operator (3a). External forcing is represented by Gaussian load functions centered at the data points:

$$q_i(x) = \frac{1}{\sigma\sqrt{2\pi}} \exp\left(-\frac{1}{2}\left(\frac{x - \xi_i}{\sigma}\right)^2\right), \quad i = 1, \ldots, n_d, \tag{18}$$

with a set of synthetic data points $\{(\xi_i, d_i)\}_{i=1}^{n_d}$. The trend is constructed as a linear combination of solution of (3a), each $u_j(x)$ corresponding to a Gaussian load centered at ξ_i (18):

$$u(x) = \sum_{j=1}^{n_d} p_j \, u_j(x),$$

where the coefficients p_j are determined by enforcing interpolation at the observation points.

6 Results

6.1 Comparison with the Exact Solution

As an initial verification, we consider the biharmonic boundary-value problem (15) on the domain $x \in [0, 10]$, where the exact solution (16) is expressed as:

$$u_{\text{exact}}(x) = \frac{1}{24}x^4 - \frac{5}{6}x^3 + \frac{25}{6}x^2.$$

We solved the discrete biharmonic problem using the cubic-Hermite finite-element formulation described in Sec. 3.1.3, and the comparison with the exact solution is shown in Figure 1. This test is especially useful because the forcing term is constant, and the exact solution is a smooth polynomial. As a result, it allows for a quick but careful evaluation of our finite element solver's accuracy and boundary condition implementation. Table 4 and Figure 1 summarize the error norms and condition numbers for uniformly refined meshes. The infinity norm and L^2 error in (17) decrease rapidly for the finer mesh, indicating the accuracy of the finite element discretization. The condition number increases proportionally to h^{-4}, where h represents the mesh size. This is consistent with the theoretical behavior of stiffness matrices associated with fourth-order operators (Ciarlet & Raviart, 1972).

6.2 Application of the PDE to Synthetic Data

The methodology was implemented on a synthetic 1D dataset after comparing the numerical and exact solutions. The computational domain was defined on $[0, 10]$ with $n_d = 14$ irregularly spaced observation points: $\{(\xi_i, d_i)\}_{i=1}^{n_d}$. The soil thickness data are

d = {1.5, 1.7, 2.0, 2.05, 2.5, 2.8, 3.0, 3.3, 3.8, 0.2, 1.0, 0.6, 4.5, 4.0}, at the corresponding locations

ξ = {6.0, 13.0, 7.0, 9.0, 11.0, 13.0, 8.0, 6.0, 27.0, 10.0, 9.0, 10., 15.0, 18.0}.

The biharmonic formulation (3a) was updated with a Gaussian load function (18) and cubic Hermite finite element discretization was used to create the basis functions. The biharmonic trend estimator is a linear combination of basis functions, with coefficients obtained by solving system (6) using observed data (Figure 2, **A**). Near $x = 4$, two closely spaced data points (Figure 2, **A**, marked by ⧫) caused small oscillations in the solution. To reduce artifacts and avoid negative soil thickness estimation, the two points were replaced with their average. The adjusted biharmonic trend is shown in (Figure 2, **B**), where the averaged point is indicated by ■, demonstrating the method's ability to capture smooth large-scale variations while suppressing spurious fluctuations. To account for uncertainty in the trend, 14 realizations (8) were generated using the sensitivity analysis described in Sec. 4.1. The variance was computed using Equation (10), and the mean trend defined in Equation (9) was used as a reliable estimate of the underlying trend(Figure 2 (**C**)).

6.3 Choice of Load Functions

In our study, we implemented two types of load functions to drive the biharmonic equation: the Dirac delta and the Gaussian function. The Dirac delta function, $\delta(x - \xi_i)$, represents an idealized point load concentrated exactly at a given observation location $\xi_i, \quad i = 1, \cdots, n_d$. Numerically, it can be implemented either as a discrete spike at the nearest grid point. Using the Dirac delta load minimizes oscillations when data points are closely spaced, and thus improves the numerical stability of the biharmonic solution. However, the physical meaning of the load is better captured by the Gaussian function, which distributes the influence of each observation over a small region controlled by a spread parameter σ. The Gaussian load gradually decreases away from the center, representing a more realistic distributed effect of each data point on the sediment soil thickness surface (Figure 2, A), because soil thickness is most likely a smooth process in space. Therefore, while the Dirac delta is useful for testing numerical performance, the Gaussian function provides a physically meaningful approximation of the influence of each observation on the surface construction of two dimentional case.

6.4 Application Sequential Gaussian Simulation

The Sequential Gaussian Simulation procedure from Sec. 4.2 was applied under two data settings to capture both large-scale trends and small-scale variability (Figure 3).

1. **SGS on the raw data (Ordinary Kriging setting).** In this case, the trend component is set to zero, and SGS is applied directly to the observed (synthetic) soil-thickness values to obtain an ordinary kriging-type estimate. (Figures 4, **A** and **C**) show a single SGS realization and the mean of 100 realizations, respectively.

2. **SGS on the residual field.** To incorporate uncertainty and capture small-scale variability, SGS was applied to the residuals obtained after removing the biharmonic trend. Multiple realizations were generated by sampling from conditional Gaussian distributions at unsampled locations. (Figure 4 , **B**) compares a single realization with the mean of hundreds of leave-one-out (LOO) realizations, while (Figure 4 , **D**) compares a single realization with the average of 100 realizations based on all residual data. The final hybrid field was reconstructed by adding the SGS residuals to the biharmonic trend (14), resulting in a surface that combines smooth large-scale structure with localized stochastic fluctuations.

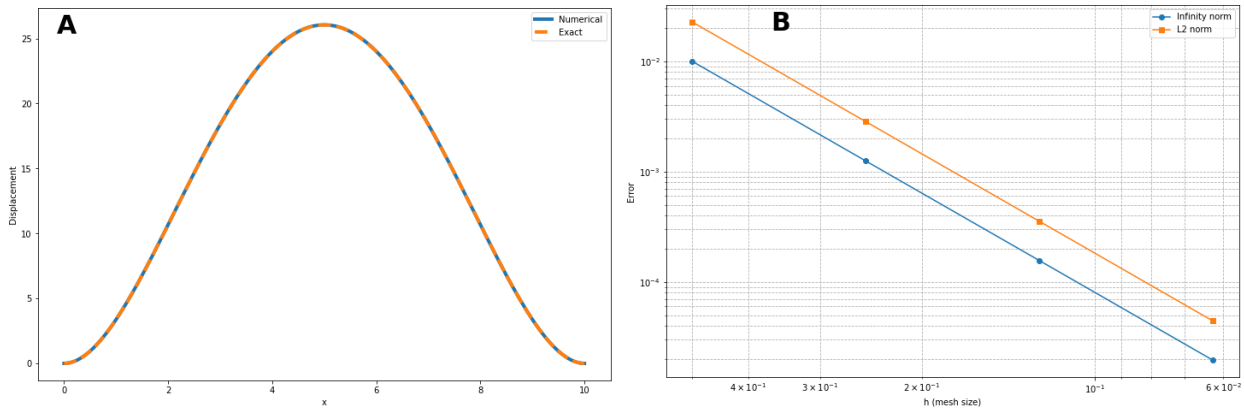

Figure 1: **A**: comparison of the numerical (15b) and exact (16) solutions; **B**: log–log plot of the errors in the infinity norm ($\|e\|_\infty$) and in the L_2 norm (17).

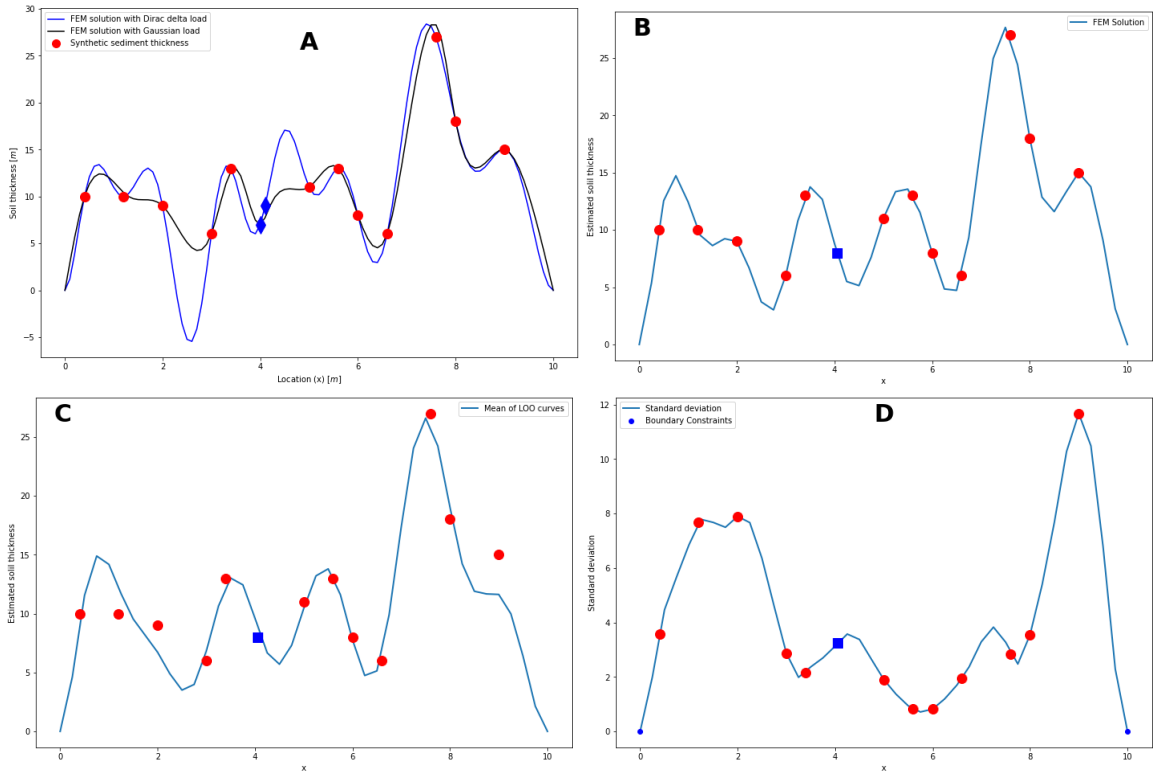

Figure 2: **A**: Interpolation at data points (6) and (7); **B**: local averaging; **C**: average of leave-one-out estimation(9); **D**: Standard deviation of the LOO curves (10).

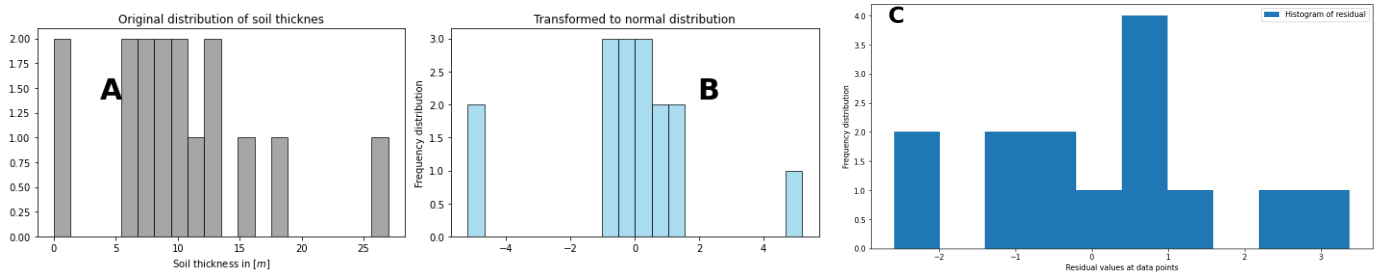

Figure 3: **A**: Histogram of synthetic soil thickness (11); **B**:Histogram of transformed soil thickness; **C**: Histogram of residual (14).

6.5 Comparison of Modeling Approaches

Based on Table 1, the variogram parameters estimated for the Ordinary Kriging (OK) and Hybrid (Trend + SGS) models differ significantly, reflecting that each model captures distinct underlying spatial structures. The smaller sill in the Hybrid model indicates that the residual variance is lower,

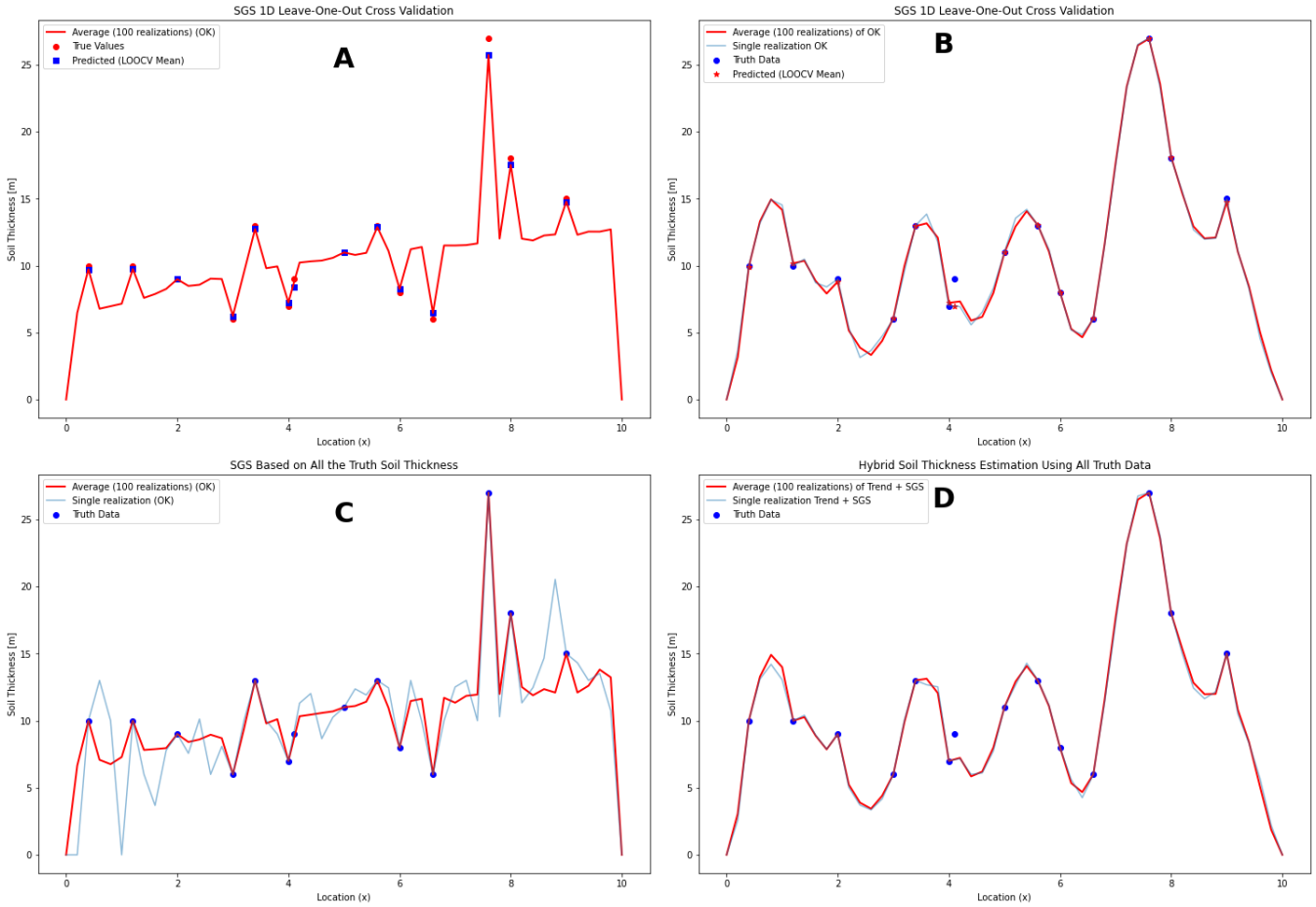

Figure 4: **A**: SGS (Ordinary Kriging estimation) applied directly to the raw data using LOO cross-validation. **B**: SGS applied to the residual field using LOO, combined with the biharmonic trend (14). **C**: SGS(OK) of all synthetic soil-thickness data. **D**: SGS of the residual computed from all synthetic soil-thickness, combined with the biharmonic trend.) (14).

confirming that the stochastic component primarily captures local fluctuations around the physically based trend. The slightly larger range in the Hybrid case also suggests improved spatial continuity of the residuals, implying that spatial correlation persists over longer distances. These variogram characteristics demonstrate that the Hybrid approach achieves a better balance between global smoothness and local variability compared to the OK model alone.

(Table 2 and 3) summarizes the performance of the three modeling approaches: the PDE-based trend model, Ordinary Kriging (OK), and the hybrid approach (Trend + SGS), in terms of Mean Absolute Error (MAE), relative Mean Absolute Error (RMAE), and the coefficient of determination (R^2). The error criterias (Table 3) indicate a substantial improvement in model performance when moving from the PDE-based trend model to the OK and hybrid methods.

Ordinary kriging provides smooth estimates by definition, but it assumes second-order stationarity. By modeling the trend separately, we instead assume first-order stationarity of the residuals, allowing for better representation of local variations while maintaining a reasonable large-scale structure (Figure 4, **A, C**). The error criteria for OK are MAE $= 0.404$, RMAE $= 0.035$, and $R^2 = 0.992$, indicating good local accuracy but limited global structural representation. The PDE-based trend model produces a smooth, curvature-driven surface that captures the majority of the large-scale spatial variability while maintaining physical consistency across the domain (Figure 2, **C**). The error metrics are MAE $= 0.966$, RMAE $= 0.083$, and $R^2 = 0.970$. This demonstrates that the trend model provides a globally coherent and physically meaningful estimation but underestimates local variations near measurement points due to the lack of a stochastic component.

The Hybrid approach (Trend + SGS) achieves the best overall performance by combining the PDE-based trend with a stochastic residual component. This integration captures soil thickness variability at both large and fine scales. The Hybrid model has the lowest errors, MAE $= 0.326$, RMAE $= 0.028$, and the highest coefficient of determination, $R^2 = 0.993$. It preserves the physically consistent trend of the PDE model while incorporating the local variability represented by the stochastic Gaussian simulation (SGS) (Figure 4, **B, D**).

Table 1: Estimated variogram parameters for Ordinary Kriging (OK) (Raw data) and Hybrid (Trend + SGS) models (residual).

Model	Nugget	Sill	Range
Ordinary Kriging (OK)	4.69	13.39	24.07
Hybrid (Trend + SGS)	1.96	3.76	27.50

Table 2: Sorted data by ascending Location

Location	Synthetic Soil Thickness	OK	Trend	Hybrid
0.4	10	9.73	8.95	9.97
1.2	10	9.75	12.22	10.33
2.0	9	8.98	6.73	9.08
3.0	6	6.25	6.83	6.09
3.4	13	12.74	12.38	12.96
4.0	7	7.25	9.59	7.21
4.1	9	8.43	8.29	7.23
5.0	11	10.98	10.45	11.02
5.6	13	12.88	13.24	13.06
6.0	8	8.27	7.76	8.04
6.6	6	6.46	6.56	6.11
7.6	27	25.74	26.18	26.98
8.0	18	17.52	19.02	18.15
9.0	15	14.79	11.62	15.00

Table 3: Validation criterias for the three methods

Method	**MAE**	**RMAE**	**R^2**
OK	0.404	0.035	0.992
Trend	0.966	0.083	0.970
Hybrid	0.326	0.028	0.993

Formulas:

$$\text{MAE} = \frac{1}{n}\sum_{i=1}^{n}|y_i - \hat{y}_i|, \quad \text{RMAE} = \frac{\text{MAE}}{\bar{y}}, \quad R^2 = 1 - \frac{\sum_{i=1}^{n}(y_i-\hat{y}_i)^2}{\sum_{i=1}^{n}(y_i-\bar{y})^2}$$

where y_i is the synthetic soil thickness at location i, $\hat{y}_i$ is the predicted value at location i, n is the total number of data points, $\bar{y}$ is the mean of synthetic soil thickness.

6.6 Two-Dimensional (Gaussian Spread)

We extend the proposed methodology to a two-dimensional setting governed by the biharmonic plate equation (2a) -(2c). The numerical experiments are designed to reconstruct soil thickness trend and to estimate the unknown coefficients p_i associated with the Gaussian load functions centered at the synthetic observation locations $\tilde{\xi}_i$ (18). The parameter σ controls the spatial spread of each Gaussian load. A small value such as $\sigma = 0.1$ yields a more localized load distribution and results in reduced oscillations in the reconstructed surface compared with a wider kernel (e.g., $\sigma = 0.5$). The larger σ spreads the load over a broader region, causing interactions between nearby observation points and introducing additional oscillatory artifacts in the solution (Figure 5 and 6).

In this experiment, we use the soil thickness data

$\tilde{d}$ = (1.6, 1.2, 0.6, 1.6, 2.0, 1.0, 2.0, 1.8, 0.8, 2.4, 0.9, 0.7, 1.0, 0.5, 0.6), at the locations

$\tilde{\xi}$ = {(3.0, 5.0), (6.0, 5.5), (8.0, 7.0), (5.0, 7.0), (7.0, 7.0), (3.0, 7.5), (3.1, 3.0), (4.0, 6.0), (5.0, 6.0), (5.1, 6.1), (6.0, 4.0), (8.0, 2.0), (5.0, 4.0), (7.0, 5.0), (9.0, 1.5)}.

Table 4: Error norms and condition numbers for the problem in Figure 1, solved with FEM on the interval $[0, 10]$ using cubic Hermite elements.

N	h	$\|e\|_\infty$	$\|e\|_2$	$cond(\mathbf{K}_h)$
20	5.000×10^{-1}	1.000×10^{-2}	2.273×10^{-2}	1.71×10^{4}
40	2.500×10^{-1}	1.250×10^{-3}	2.841×10^{-3}	2.75×10^{5}
80	1.250×10^{-1}	1.566×10^{-4}	3.552×10^{-4}	4.41×10^{6}
160	6.250×10^{-2}	1.958×10^{-5}	4.440×10^{-5}	7.06×10^{7}

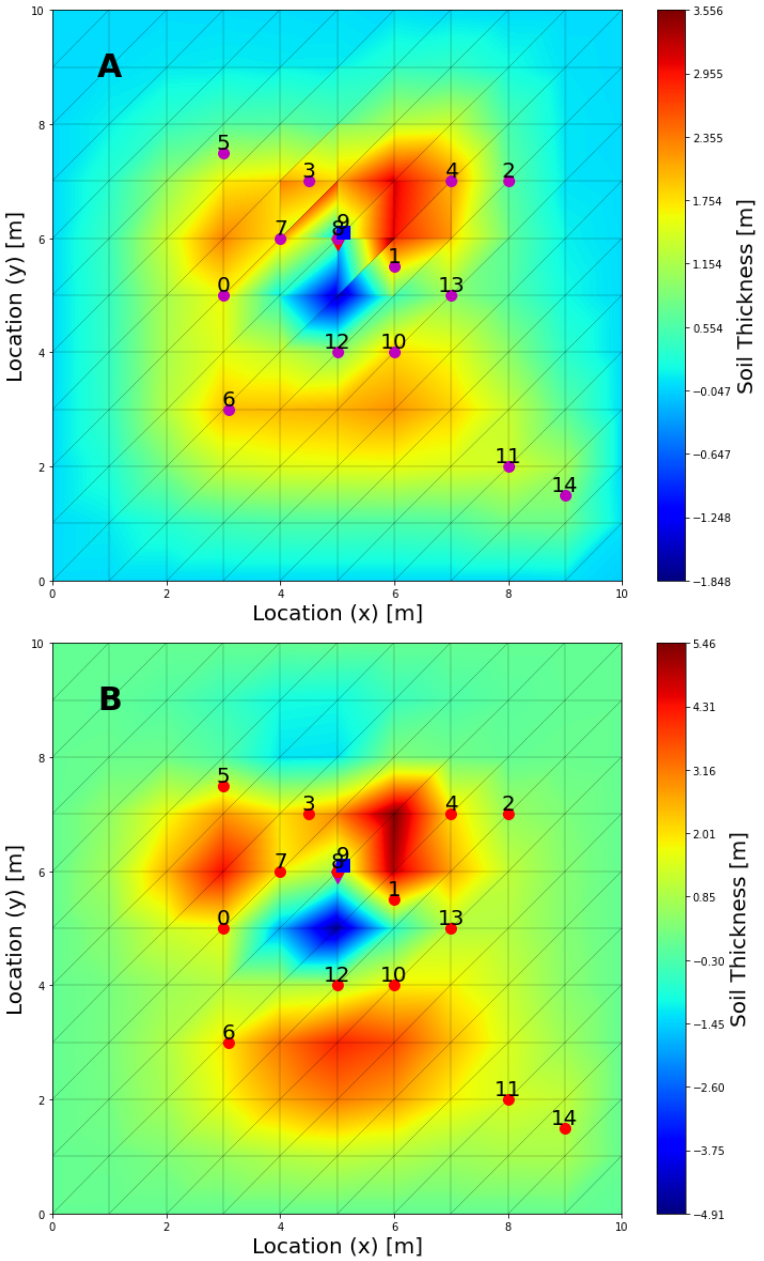

Figure 5: (**A**) Two-dimensional interpolation results with $\sigma = 0.1$. (**B**) Two-dimensional interpolation results with $\sigma = 0.5$. The points ■ and ♦ highlight the two data points responsible for the observed oscillation.

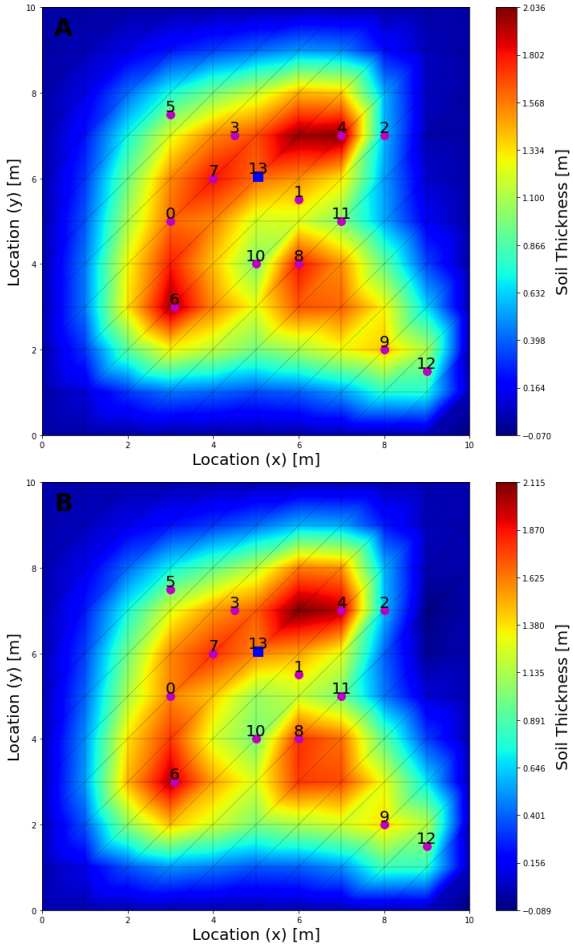

Figure 6: Results after replacing the two data points (shown as ■ and ♦ in Figure 5) with their averaged value. (**A**) uses $\sigma = 0.1$, and (**B**) uses $\sigma = 0.5$.

7 Discussion

The one-dimensional experiments were carried out to examine the behavior of the proposed approach in a controlled setting where the exact solution is known (Figure 1). This allows a transparent assessment of how the biharmonic trend model and the stochastic residual component contribute to the final estimate. The results show that the biharmonic trend captures the large-scale structure of the soil profile and produces a smooth background surface. This smoothness arises naturally from the biharmonic operator and prevents the type of overfitting that may occur when interpolation is applied directly to sparse or unevenly spaced data (Figure 2). The trend is therefore well suited for representing the slowly varying component of the soil thickness field. The stochastic component introduced through SGS adds the local variability that the PDE-based trend cannot reproduce. Because SGS simulates conditional realizations using the estimated variogram structure, it preserves the spatial correlation observed in the data while introducing realistic small-scale fluctuations. The ensemble of SGS realizations provides a measure of uncertainty, and the variance field highlights regions where predictions become less reliable. As expected, these areas coincide with locations where observations are sparse or where the measured values exhibit sharp deviations from the surrounding trend. Interpolation-related limitations. The study also revealed limitations when interpolation is used directly on the data without regularization. In particular, when observations lie very close to each other as illustrated by the points marked with ■ and ♦ the interpolant may develop oscillations in the reconstructed surface. This behavior is visible in both one-dimensional and the two-dimensional examples (Figures 4, **A** , Figures 5, **A** and **B**) and is a well-known artifact of high-order interpolation on irregularly spaced data. Local averaging of the problematic points reduces these oscillations (Figures 4, **B**, Figures 6, **A** and **B**) and leads to a more stable surface while preserving the general structure of the dataset. To construct the two-dimensional discrete form of (2), we used the `DUNE` approach (Bastian et al., 2021). The `dune-vem` module enables the use of $\mathcal{C}^1$-conforming virtual element spaces, which provide a smooth representation suitable for the biharmonic equation. This formulation reduces the number of degrees of freedom relative to classical finite elements without sacrificing accuracy (Beirão da Veiga et al., 2013; Dedner & Hodson, 2024). In addition, the choice of the kernel width σ in (18) affects the smoothness and flexibility of the basis functions: larger values of σ allow sharper local variations, while smaller values produce smoother surfaces. The numerical experiments in 2D (Figures 5, **A** and **B**) illustrate this influence.

Overall, the combination of a biharmonic trend and a stochastic residual model provides a balance between physical smoothness and local variability. The trend offers global coherence, while SGS supplies the fine-scale fluctuations needed to represent the observed soil thickness. The 1D tests verify the correctness of the approach and clarify the role of each component before applying the method to more complex two-dimensional domains.

8 Conclusion

The hybrid PDE-SGS method demonstrates advantages over the individual components, providing improved predictive accuracy and a more realistic representation of soil thickness variability. While the present study focuses on one-dimensional and regular two-dimensional domains to verify the mathematical formulation and numerical implementation, the framework naturally extends to irregular two-dimensional settings. In such cases, the treatment of boundary conditions becomes more practical. To clarify this point, we now refer the reader to our extended work (Bekele et al., 2025), where we have already implemented a mixed, data-driven boundary (domain) strategy: observed data are used to prescribe boundary values along measured boundary segments, while Neumann conditions are applied on segments lacking observations. As demonstrated in (Bekele et al., 2025), this approach enhances the physical realism of the reconstructed soil-thickness surfaces.

Acknowledgments

We are grateful to Prof. Anne Kværnø, Prof. Claus Führer, and Dr. Alemayehu Adugna, for many inspiring discussions. The authors also thank the Department of Mathematics, Hawassa University, for its institutional support.

Funding

This research received no specific grant from funding agencies in the public, commercial, or not-for-profit sectors.

Conflict of interest

The authors declare that they have no conflict of interest.

References

Antonietti, P. F., Manzini, G., & Verani, M. (2018). The fully nonconforming virtual element method for biharmonic problems. *Mathematical Models and Methods in Applied Sciences*, *28*(2), 387–407. https://doi.org/10.1142/S0218202518500100

Bastian, P., Blatt, M., Dedner, A., Dreier, N. A., Engwer, C., Fritze, R., Grser, C., Grninger, C., Kempf, D., Klfkorn, R., Ohlberger, M., & Sander, O. (2021). The dune framework: Basic concepts and recent developments. *Computers & Mathematics with Applications*, *81*, 75–112.

Beirão da Veiga, L., Brezzi, F., Cangiani, A., Manzini, G., Marini, L. D., & Russo, A. (2013). Basic principles of virtual element methods. *Mathematical Models and Methods in Applied Sciences*, *23*(1), 199–214.

Bekele, S. S., Wolde, M. M., Führer, C., Kitterød, N.-O., & Kværnø, A. (2025). Modeling a smooth surface by a constrained biharmonic equation with application in soil science. https://arxiv.org/abs/2510.23195

Braess, D. (2007). *Finite elements: Theory, fast solvers, and applications in solid mechanics* (3rd ed.). Cambridge University Press.

Brenner, S. C., & Scott, L. R. (2008). *The mathematical theory of finite element methods* (3rd ed., Vol. 15). Springer.

Chinosi, C., & Marini, L. D. (2006). A virtual element method for the biharmonic problem. *Computers & Structures*, *84*(13–14), 914–923.

Ciarlet, P. G., & Raviart, P. A. (1972). Finite element approximation of the biharmonic problem. *Numerische Mathematik*, *18*(4), 335–348.

Dedner, A., & Hodson, A. (2024). A framework for implementing general virtual element spaces. *SIAM Journal on Scientific Computing*, *46*(3), B229–B253. https://doi.org/10.1137/23M1573653

Deutsch, C. V., & Journel, A. G. (1992). Geostatistical software library and users guide. *New York*.

Gazzola, F., Grunau, H.-C., & Sweers, G. (2010). *Polyharmonic boundary value problems* (Vol. 1991). Springer.

Gómez-Hernández, J. J., & Srivastava, R. M. (2021). One step at a time: The origins of sequential simulation and beyond. *Mathematical Geosciences*, *53*(2), 193–209.

Jamshidi, R., Dragovich, D., & Webb, A. A. (2014). Catchment scale geostatistical simulation and uncertainty of soil erodibility using sequential gaussian simulation. *Environmental Earth Sciences*, *71*(12), 4965–4976.

Kitterød, N.-O., & Leblois, É. (2021). Estimation of sediment thickness by solving poisson's equation with bedrock outcrops as boundary conditions. *Hydrology Research*, *52*(3), 597–619.

Kumar, R. (2024). Numerical solutions for biharmonic interface problems via weak galerkin finite element methods. *Applied Mathematics and Computation*, *467*, 128496. https://doi.org/10.1016/j.amc.2023.128496

Liu, Q., West, A. J., & Dietrich, W. E. (2013). A simple geomorphic-based analytical model for predicting the spatial distribution of soil thickness in headwater hillslopes and catchments. *Water Resources Research*, *49*(10), 7029–7046. https://doi.org/10.1002/2013WR013834

Szabó, B. A., & Babuška, I. (2021). *Applied finite element analysis* (2nd ed.). John Wiley & Sons.

Timoshenko, S. P., & Goodier, J. N. (1951). *Theory of elasticity* (2nd ed.). McGraw–Hill.

Timoshenko, S. P., & Woinowsky-Krieger, S. (1959). *Theory of plates and shells* (2nd ed.). McGraw-Hill.

Webster, R., & Oliver, M. A. (2007). *Geostatistics for environmental scientists* (2nd ed.). John Wiley & Sons.

Yan, Q., Wainwright, H., Dafflon, B., Uhlemann, S., Falco, N., Kwang, J., & Hubbard, S. (2021). A hybrid data–model approach to map soil thickness in mountain hillslopes. *Earth Surface Dynamics*, *9*, 1347–1367. https://doi.org/10.5194/esurf-9-1347-2021

East African Journal of Biophysical and Computational Sciences
ISSN (Online): 2789-3618 and ISSN (Print): 2789-360X

Journal Information

Volume 6(2), 2025
DOI: https://dx.doi.org/10.4314/eajbcs.v6i2.3S

Homepage:
https://journals.hu.edu.et/hu-journals/index.php/eajbcs

Article History

Received: 09 October, 2025
Accepted: 24 November, 2025
Published Online: 25 December, 2025

How to cite

Chikako T.U and Goshu A.T. (2025). Alpha Power Transformed Half Normal Distribution with Its Properties and Applications. *East African Journal of Biophysical and Computational Sciences* Volume 6(2), 2025, 27-37

ARTICLE

Alpha Power Transformed Half Normal Distribution with Its Properties and Applications

Teshita Uke Chikako[1,*], **Ayele Taye Goshu**[1]

[1]Department of Mathematics Education, Kotebe University of Education, Ethiopia
*Corresponding author: tasheman09@gmail.com

Abstract

The study aims to propose a new continuous probability distribution named Alpha Power Transformed Half-Normal Distribution by applying alpha power transformation method to Half normal distribution. Several vigorous statistical and mathematical properties of new distribution are derived. Simulation studies are conducted to evaluate their performance, and comparative model fitting is carried out using real and simulated datasets. The study employs the alpha power transformation technique, simulation experiments, and goodness-of-fit measures to compare the new distribution with five existing distributions. Results indicate that the proposed model provides a superior fit to two real-world datasets and one simulated dataset compared to five competing distributions. The hazard function of the new distribution exhibits highly flexible forms, enhancing its applicability to various lifetime and reliability data. The Alpha Power Transformed Half-Normal Distribution represents a significant contribution to probability and statistical theory. Its flexibility and strong empirical performance suggest its potential for broad application, and further testing on diverse life datasets is recommended.

Keywords: Alpha power transformation; New distribution; Half-normal distribution; Probability and Statistics.

East African Journal of Biophysical and Computational Sciences (EAJBCS) is already indexed on known databases like AJOL, DOAJ, CABI ABSTRACTS and FAO AGRIS.

1 Introduction

Probability distributions perform a decisive role in data-driven decision-making and analysis. Their applications span numerous fields, including physics, computer science, public health, medicine, insurance, reliability analysis, survival analysis, signal processing, communications, and engineering. However, classical distributions often fail to adequately represent diverse real-world datasets, highlighting the need to generalize existing distributions (Mohiuddin & Kannan, 2022). The generalization of existing probability models has become an important area of research in statistical theory (Mohiuddin & Kannan, 2021). For example, Yousof H.M. (2019) presented a new lifetime and regression model with real-world applications, while Alizadeh et al. (2021) proposed a new two-parameter lifetime model and derived its statistical properties. Similarly, Altun et al. (2018) introduced a generalized lifetime model derived from

the half-normal distribution, including its regression form and properties.

The Half-Normal (HN) distribution is a special case of the normal distribution restricted to non-negative values (Nadarajah & Kotz, 2006). It has been widely used in lifetime data analysis, quality control, and various other disciplines (Wallner, 2020). Despite its usefulness, the HN distribution is limited by its rigidity, with its shape is controlled solely by a single scale parameter, making it incapable of modeling skewed, heavy-tailed, or otherwise complex datasets. Moreover, its hazard rate is monotonic and non-decreasing, which restricts its applicability in modeling systems that exhibit non-monotonic hazard behaviors, such as bathtub-shaped or decreasing hazard rates commonly seen in reliability and survival studies.

To address these limitations, numerous extensions of the HN distribution had been proposed. For instance, the Square-Transformed Half-Normal distribution, derived by (Bousseba & Sakr, 2025), has a fixed shape because squaring does not introduce any additional parameter. Its tail behavior, skewness, and kurtosis are still inflexible and unable to adjust to actual data that calls for flexibility and various hazard shapes. The Alpha Power Transformed Half-Normal distribution is motivated by this constraint and overcomes it by adding a shape parameter. Similarly, the Exponentiated Half-Normal Distribution (EHND) introduced by Cordeiro et al. (2016) adds a shape parameter to enhance flexibility in modeling various data structures. Likewise, the Kumaraswamy Half-Normal Distribution (KHND) developed by Alizadeh et al. (2020) incorporates the Kumaraswamy distribution as a generator, providing additional adaptability for diverse data patterns. Although these generalizations improve the model's flexibility, they still may not adequately capture certain complex datasets or hazard rate shapes, such as bathtub or decreasing hazard functions frequently observed in reliability studies.

Several other one-parameter lifetime distributions have been developed. For example, the XGamma distribution proposed by Sen et al. (2016) combines exponential and gamma distributions, while the XLindley distribution introduced by Chouia and Zeghdoudi (2021) mixes exponential and Lindley distributions. Both models exhibit desirable statistical properties, but are limited by their single-parameter structure, which restricts their ability to model a wide range of data behaviors. In an effort to enhance flexibility, Alshenawy (2022) developed the three-parameter X-Gamma Inverse Weibull distribution, whose density is a linear combination of Inverse Weibull densities. Although this model can capture increasing, decreasing, and unimodal hazard rates, it still fails to represent bathtub-shaped hazards adequately. Therefore, there remains a need for a more flexible two-parameter model capable of fitting datasets with various hazard rate forms.

To fill this gap, we introduce a new distribution with additional shape parameter from the half-normal distribution using the alpha power transformation (APT) method. The alpha power transformation technique, originally developed by Mahdavi and Kundu (2017), provides a systematic way to generate flexible probability distributions. Later, (Alizadeh et al., 2021) extended this concept to define a broader class of modified distributions.

The primary objective of this study is to propose a new, lithe two-parameter model called the Alpha Power Transformed Half-Normal Distribution (APTHND). We derive and prove its statistical properties, and demonstrate its performance through data fitting, simulation studies, and graphical analyses using R software version 4.3.1 (R Core Team, 2023).

2 The Base Half Normal Distribution

The half-normal distribution is a probability distribution that is a variant of the normal distribution, but only extends in one direction from the mean. It is a widely used distribution in applied statistics (Wallner, 2020). It provides a useful framework for modeling and analyzing non-negative continuous data that exhibits one-sided patterns.

Let the random variable represented by X follow the half normal distribution with mean zero and variance σ^2. Then, the corresponding probability density and cumulative distribution functions are given as (Bader et al., 2022).

$$f(x) = \frac{\sqrt{2}}{\sigma\sqrt{\pi}} e^{-x^2/(2\sigma^2)}, \quad x > 0, \tag{1}$$

$$F(x) = \text{erf}\left(\frac{x}{\sigma\sqrt{2}}\right), \quad x > 0, \tag{2}$$

where $\text{erf}(\cdot)$ is the error function.

In this paper, we introduce a new distribution by transforming the half normal distribution using the alpha power transformation technique proposed by Mahdavi and Kundu (2017).

3 Alpha Power Transformed Half-Normal Distribution

The Alpha Power Transformation (APT) approach was introduced by Mahdavi and Kundu (2017) to increase flexibility of the new class of distributions. Given base distribution with $f(x)$ and $F(x)$, the APT transformation generally gives new probability density function $f_{APT}(x)$ and cumulative distribution function $F_{APT}(x)$:

$$f_{\text{APT}}(x) = \begin{cases} \log(\alpha) f(x)[\alpha F(x)]^{\alpha-1}, & \text{if } \alpha > 0, \alpha \neq 1, \\ f(x), & \text{if } \alpha = 1, \end{cases} \tag{3}$$

$$F_{\text{APT}}(x) = \begin{cases} \dfrac{\alpha F(x) - 1}{\alpha - 1}, & \text{if } \alpha > 0, \alpha \neq 1, \\ F(x), & \text{if } \alpha = 1. \end{cases} \tag{4}$$

Using APT method given in equations (3 - 4), we introduce the novel distribution which is called Alpha Power Transformed Half Normal (APTHN) distribution from the base half normal distribution given in equations (1- 2).

Theorem 1: A random variable X having an alpha power transformed half normal distribution with two parameters if its CDF and PDF were given as below:

a. The CDF is

$$F_{\text{APTHN}}(x;\alpha,\sigma^2)=\begin{cases}\dfrac{\alpha^{\text{erf}\left(\frac{x}{\sigma\sqrt{2}}\right)}-1}{\alpha-1}, & \text{if } x>0,\ \alpha>0,\ \alpha\neq 1,\\ \text{erf}\left(\dfrac{x}{\sigma\sqrt{2}}\right), & \text{if } x>0,\ \alpha=1.\end{cases} \tag{5}$$

b. The PDF is

$$f_{\text{APTHN}}(x;\alpha,\sigma^2)=\begin{cases}\dfrac{2\alpha\,\text{erf}\left(\frac{x}{\sigma\sqrt{2}}\right)\ln(\alpha)e^{-x^2/(2\sigma^2)}}{\sqrt{\pi}\,\sigma(\alpha-1)}, & \text{if } x>0,\ \alpha>0,\\ & \alpha\neq 1,\\ \dfrac{2}{\sigma\sqrt{\pi}}e^{-x^2/(2\sigma^2)}, & \text{if } x>0,\ \alpha=1.\end{cases} \tag{6}$$

The function $f_{\text{APTHN}}(x;\alpha,\sigma^2)$ is non-negative and has integration equal to one.

Proof: a. If X is a random variable following APTHN distribution, then its CDF is derived by substituting equation (2) in equation (4):

$$\begin{aligned}F_{\text{APTHN}}(x;\alpha,\sigma^2)&=\frac{\alpha^{F(x)}-1}{\alpha-1}\\&=\frac{\alpha^{\text{erf}\left(\frac{x}{\sigma\sqrt{2}}\right)}-1}{\alpha-1}.\end{aligned}$$

b. If X is a random variable following APTHN distribution, then its PDF is obtained by derivation of equation (5):

$$\begin{aligned}f_{\text{APTHN}}(x;\alpha,\sigma^2)&=\frac{d}{dx}\left(F_{\text{APT}}(x;\alpha,\sigma^2)\right)\\&=\frac{d}{dx}\left(\frac{\alpha^{\text{erf}\left(\frac{x}{\sigma\sqrt{2}}\right)}-1}{\alpha-1}\right)\\&=\frac{1}{\alpha-1}\frac{d}{dx}\left(\alpha^{\text{erf}\left(\frac{x}{\sigma\sqrt{2}}\right)}\right)\\&=\frac{1}{\alpha-1}\ln(\alpha)\alpha^{\text{erf}\left(\frac{x}{\sigma\sqrt{2}}\right)}\frac{d}{dx}\left[\text{erf}\left(\frac{x}{\sigma\sqrt{2}}\right)\right]\\&=\frac{1}{\alpha-1}\ln(\alpha)\alpha^{\text{erf}\left(\frac{x}{\sigma\sqrt{2}}\right)}\cdot\frac{2}{\sqrt{\pi}}e^{-x^2/(2\sigma^2)}\cdot\frac{1}{\sigma\sqrt{2}}\\&=\frac{\sqrt{2}\ln(\alpha)\alpha^{\text{erf}\left(\frac{x}{\sigma\sqrt{2}}\right)}e^{-x^2/(2\sigma^2)}}{\sqrt{\pi}(\alpha-1)\sigma}.\end{aligned}$$

To show integration of PDF is unity:

$$\begin{aligned}&\int_0^\infty f_{\text{APTHN}}(x)\,dx\\&\quad=\int_0^\infty\frac{\sqrt{2}\ln(\alpha)e^{-x^2/(2\sigma^2)}\alpha^{\text{erf}\left(\frac{x}{\sigma\sqrt{2}}\right)}}{\sqrt{\pi}(\alpha-1)\sigma}\,dx\\&\quad=\frac{\sqrt{2}\ln(\alpha)}{\sqrt{\pi}(\alpha-1)\sigma}\int_0^\infty e^{-x^2/(2\sigma^2)}\alpha^{\text{erf}\left(\frac{x}{\sigma\sqrt{2}}\right)}\,dx.\end{aligned}$$

Let $u=\text{erf}\left(\frac{x}{\sigma\sqrt{2}}\right)$. Then

$$\frac{du}{dx}=\frac{2}{\sqrt{\pi}}e^{-x^2/(2\sigma^2)}\cdot\frac{1}{\sigma\sqrt{2}},\quad dx=\frac{\sqrt{\pi}\sigma}{\sqrt{2}}e^{x^2/(2\sigma^2)}\,du.$$

Thus,

$$\begin{aligned}&\int_0^\infty f_{\text{APTHN}}(x)\,dx\\&\quad=\frac{\sqrt{2}\ln(\alpha)}{\sqrt{\pi}(\alpha-1)\sigma}\int_0^1 e^{-x^2/(2\sigma^2)}\alpha^u\frac{\sqrt{\pi}\sigma}{\sqrt{2}}e^{x^2/(2\sigma^2)}\,du\\&\quad=\frac{\ln(\alpha)}{\alpha-1}\int_0^1\alpha^u\,du\\&\quad=\frac{\ln(\alpha)}{\alpha-1}\left.\frac{\alpha^u}{\ln(\alpha)}\right|_0^1\\&\quad=\frac{1}{\alpha-1}(\alpha^1-\alpha^0)=1.\end{aligned}$$

Theorem 2: Assume a random variable X follows the APTHN distribution, then

The survival function of X is

$$S_{\text{APTHN}}(x;\alpha,\sigma^2)=\begin{cases}\dfrac{\alpha-\alpha^{\text{erf}\left(\frac{x}{\sigma\sqrt{2}}\right)}}{\alpha-1}, & \text{if } x>0,\ \alpha>0,\ \alpha\neq 1,\\ 1-\text{erf}\left(\dfrac{x}{\sigma\sqrt{2}}\right), & \text{if } x>0,\ \alpha=1.\end{cases} \tag{7}$$

The hazard rate function of X is

$$h_{\text{APTHN}}(x;\alpha,\sigma^2)=\begin{cases}\dfrac{2\alpha^{\text{erf}\left(\frac{x}{\sigma\sqrt{2}}\right)}\ln(\alpha)e^{-x^2/(2\sigma^2)}}{\sqrt{\pi}\,\sigma\left(\alpha-\alpha^{\text{erf}\left(\frac{x}{\sigma\sqrt{2}}\right)}\right)}, & \text{if } x>0,\ \alpha>0,\\ & \alpha\neq 1,\\ \dfrac{2e^{-x^2/(2\sigma^2)}}{\sqrt{\pi}\,\sigma\left[1-\text{erf}\left(\frac{x}{\sigma\sqrt{2}}\right)\right]}, & \text{if } x>0,\ \alpha=1.\end{cases} \tag{8}$$

Proof: For the random variable X with $\alpha>0,\alpha\neq 1$, its survival function is:

$$\begin{aligned}S_{\text{APTHN}}(x;\alpha,\sigma^2)&=\int_x^\infty f_{\text{APTHN}}(t;\alpha,\sigma^2)\,dt\\&=\int_x^\infty\frac{\sqrt{2}\ln(\alpha)e^{-t^2/(2\sigma^2)}\alpha^{\text{erf}\left(\frac{t}{\sigma\sqrt{2}}\right)}}{\sqrt{\pi}(\alpha-1)\sigma}\,dt\\&=\frac{\sqrt{2}\ln(\alpha)}{\sqrt{\pi}(\alpha-1)\sigma}\int_x^\infty e^{-t^2/(2\sigma^2)}\alpha^{\text{erf}\left(\frac{t}{\sigma\sqrt{2}}\right)}\,dt.\end{aligned}$$

Let $u = \text{erf}\left(\frac{t}{\sigma\sqrt{2}}\right)$. Then

$$\frac{du}{dt} = \frac{2}{\sqrt{\pi}} e^{-t^2/(2\sigma^2)} \cdot \frac{1}{\sigma\sqrt{2}}, \quad dt = \frac{\sqrt{\pi}\sigma}{\sqrt{2}} e^{t^2/(2\sigma^2)}\, du.$$

Thus,

$$\begin{aligned} S_{\text{APTHN}}(x;\alpha,\sigma^2) &= \frac{\sqrt{2}\ln(\alpha)}{\sqrt{\pi}(\alpha-1)\sigma} \int_{u(x)}^{1} e^{-t^2/(2\sigma^2)} \alpha^u \frac{\sqrt{\pi}\sigma}{\sqrt{2}} e^{t^2/(2\sigma^2)}\, du \\ &= \frac{\ln(\alpha)}{\alpha-1} \int_{\text{erf}\left(\frac{x}{\sigma\sqrt{2}}\right)}^{1} \alpha^u\, du \\ &= \frac{\ln(\alpha)}{\alpha-1} \left.\frac{\alpha^u}{\ln(\alpha)}\right|_{\text{erf}\left(\frac{x}{\sigma\sqrt{2}}\right)}^{1} \\ &= \frac{1}{\alpha-1}\left(\alpha^1 - \alpha^{\text{erf}\left(\frac{x}{\sigma\sqrt{2}}\right)}\right) \\ &= \frac{\alpha - \alpha^{\text{erf}\left(\frac{x}{\sigma\sqrt{2}}\right)}}{\alpha-1}. \end{aligned}$$

The hazard function of random variable X is:

$$h_{\text{APTHN}}(x;\alpha,\sigma^2) = \begin{cases} \dfrac{2\alpha^{\text{erf}\left(\frac{x}{\sigma\sqrt{2}}\right)} \ln(\alpha) e^{-x^2/(2\sigma^2)}}{\sqrt{\pi}\,\sigma\left(\alpha - \alpha^{\text{erf}\left(\frac{x}{\sigma\sqrt{2}}\right)}\right)}, & \text{if } x>0,\ \alpha>0, \\ & \alpha \neq 1, \\ \dfrac{2e^{-x^2/(2\sigma^2)}}{\sqrt{\pi}\,\sigma\left[1-\text{erf}\left(\frac{x}{\sigma\sqrt{2}}\right)\right]}, & \text{if } x>0,\ \alpha=1. \end{cases} \tag{9}$$

4 Plots of Alpha Power Transformed Half Normal Distribution

The plots of the probability density function, cumulative distribution function, survival function, and hazard function of the APTHN distribution are shown in three cases. These are when variance is equal to one, when variance is greater than one, and when variance is less than one.

Case 1. Case of variance of half normal distribution $\sigma^2 = 1$ with $0 < \alpha \geq 1$ The plots in Figure 1 show that as alpha value gets very small ($\alpha < 1$) while variance is kept at unity, the curve of pdf loses its bell shape until it looks like the decaying exponential density function. The mode grows. The respective cdf quickly grows and converges to one as alpha gets smaller as compared to the base half normal case (alpha = 1). The black colored plots refer to the base half normal distribution.

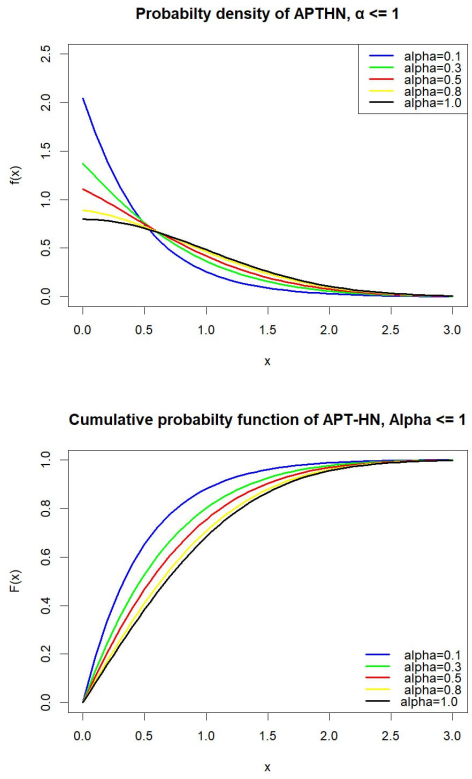

Figure 1: Plots of density and cumulative distribution functions of APTHN for $\alpha \leq 1, \sigma^2 = 1$.

Plots in Figure 2 show that as alpha value gets larger (alpha > 1) while variance is fixed to be one, the modal point moves to the right, generates high left skewness and low right skewness. The cdf grows and converges to 1 with lower growth rate as compared to the base distribution.

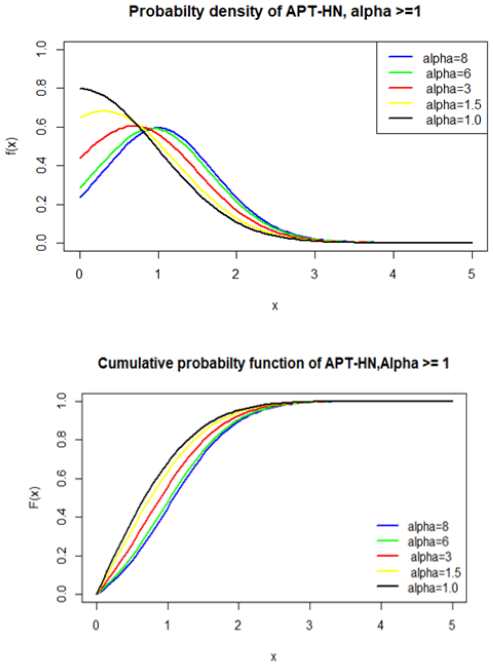

Figure 2: Plots of density and cumulative distribution functions of APTHN for $\alpha \geq 1, \sigma^2 = 1$.

Figures 3-4 illustrates the respective survival and hazard functions. The survival function is generally decreasing and converges to limit zero. Its rate of decay increases with increasing alpha value. The hazard function has bump shapes for alpha smaller than one and is ever increasing for alpha greater than one. These are new interesting features of the hazard function we can expect from the new APTHN distribution. The black-colored plots refer to the base half-normal distribution.

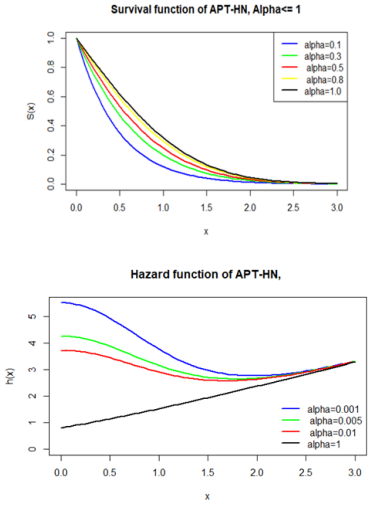

Figure 3: Plots of survival and hazard function of APTHN for $0 < \alpha \leq 1, \sigma^2 = 1$

Case 2. Case of variance of half normal distribution $\sigma^2 > 1$ with $0 < \alpha \geq 1$ Figures 5-8 show that the plots of the PDF, CDF, survival and hazard functions. Similar curves and properties are illustrated by the new distribution except over the larger domain of X. This is expected since larger variance is taken. The black colored plots refer to the base half normal distribution.

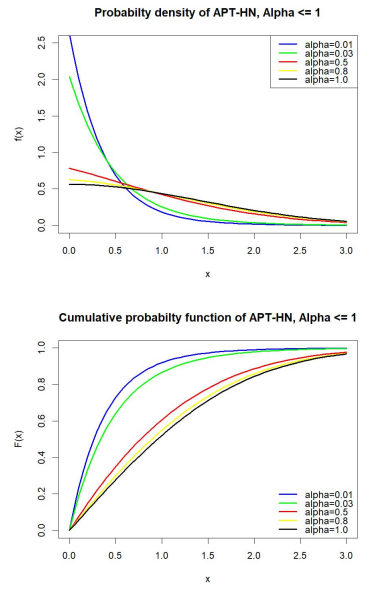

Figure 5: Plots of survival and hazard function of APTHN for $0 < \alpha \leq 1, \sigma^2 = 1$

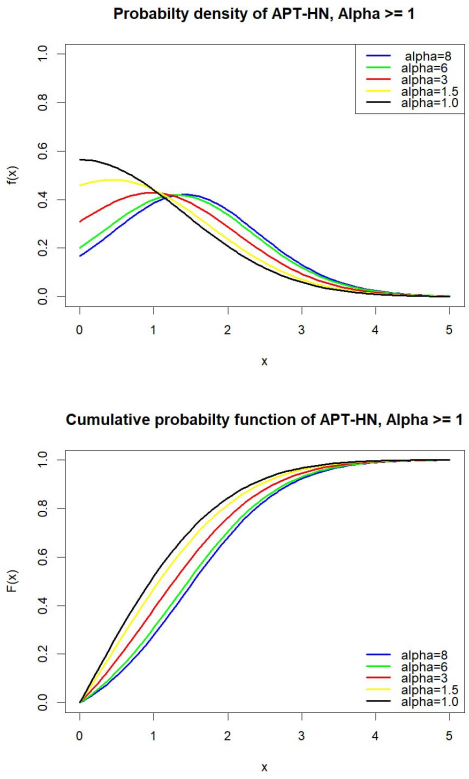

Figure 6: Plots of density and cumulative distribution functions for $\alpha \geq 1, \sigma^2 = 2$.

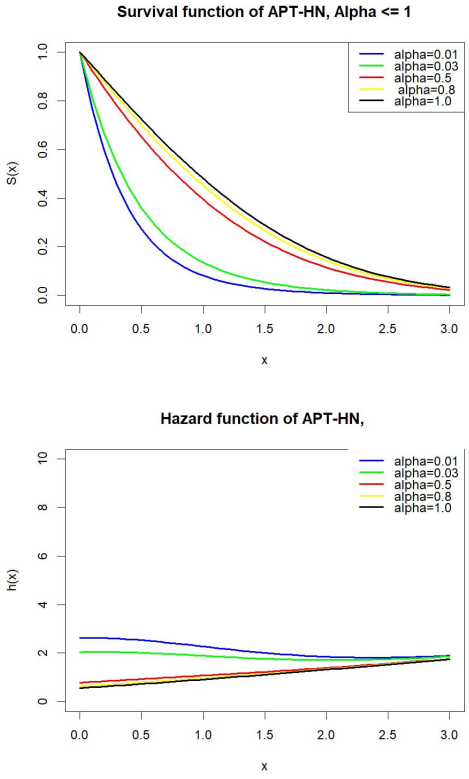

Figure 7: Plots of survival and hazard functions for $0 < \alpha \leq 1$, $\sigma^2 = 2$

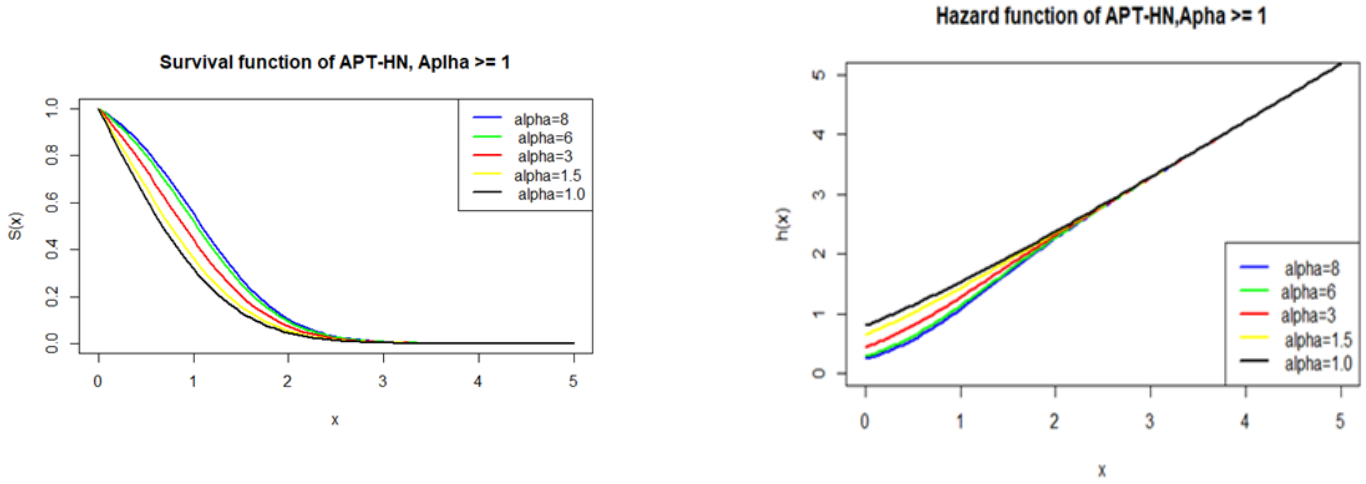

Figure 4: Plots of survival and hazard function of APTHN for $\alpha \geq 1, \sigma^2 = 1$.

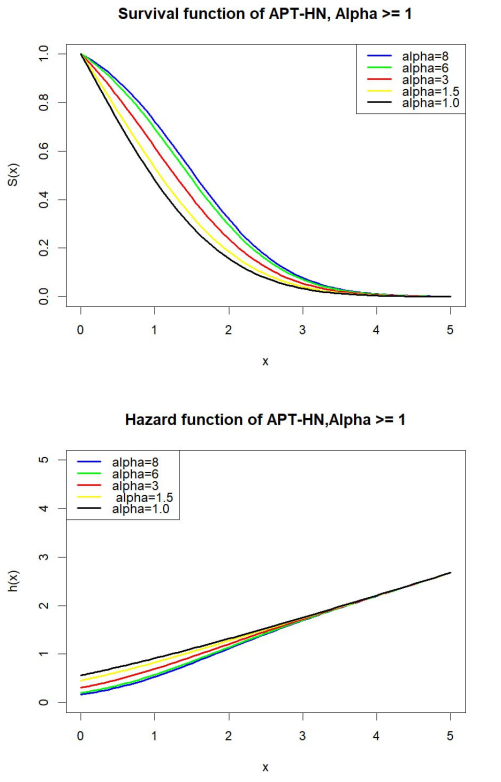

Figure 8: Plots of survival and hazard functions for $\alpha \geq 1$, $\sigma^2 = 2$.

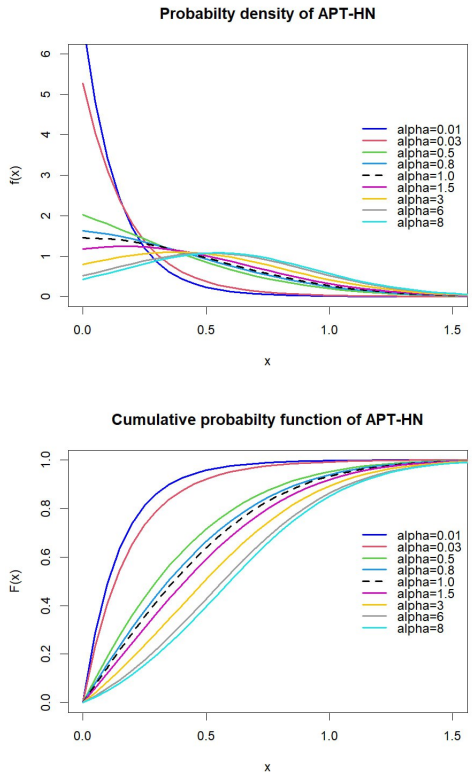

Figure 9: Plots of density and cumulative distribution functions for $0 < \alpha \geq 1, \sigma^2 = 0.3$.

Case 3. Case of variance of half normal distribution $\sigma^2 < 1$ with $0 < \alpha \geq 1$ The plots in Figure 9-10 demonstrate that the curves of the probability density, cumulative distribution, survival and hazard functions of the new distribution shrink to smaller domain of X and re-shaping the skewness of the distribution. This is expected for such smaller variance values less than one. The hazard function shows flexible curves that can be used for modelling life data having such behavior including bumping shapes. Black colored plots refer to base distribution.

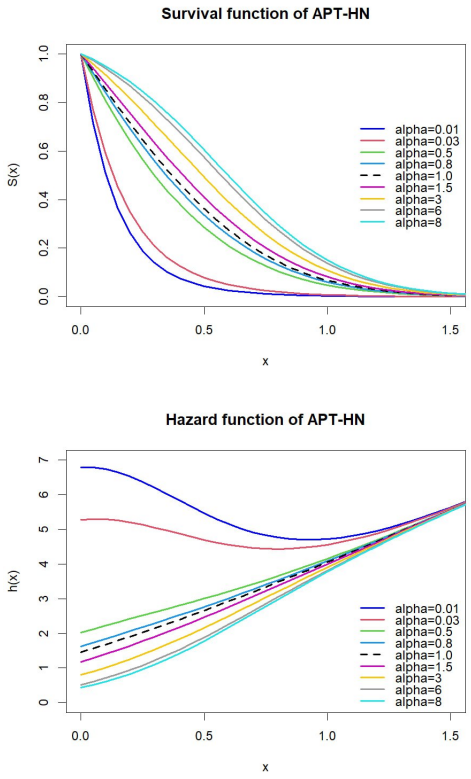

Figure 10: Plots of survival and hazard functions for $0 < \alpha \geq 1$, $\sigma^2 = 0.3$.

The plots 1-10 demonstrate the shapes of the probability density, cumulative distribution, survival, and hazard functions of the new distribution. Various interesting features are shown by varying the two parameters. One feature to emphasize is the plot with parameters = 0.01 and = 0.3 with blue color in Figure 9-10. The plot shows a decaying nature in the pdf, the fastest growth in the cdf, a fast decline in survival probability, and the largest hazard rate with a bumping shape. The hazard rate has inflection points.

In data fitting practices, for example, for right-skewed data, we often require such a new distribution as an alternative model to the exponential distribution whose hazard rate is constant. Thus, we believe that the new probability distribution (APTHND) is different from the base distribution and is so flexible, showing its novelty. We derive detailed properties of the model APTHN distribution in next section.

5 Properties of Alpha Power Transformed Half Normal Distribution

5.1 Quantile Function and Median

Assume X is the random variable that follows the APTHN distribution with location zero, variance sigma square and shape alpha, then the quantile function Q(u) of X is given by:

$$Q(u) = F^{-1}\left(\frac{\alpha^{erf(u/\sigma\sqrt{2})} - 1}{\alpha - 1}\right) \tag{10}$$

If u is uniform distribution with interval (0,1), then X APTHN, the pth quantile function of APTHN distribution is given by:

$$X_p = \frac{\sqrt{2}\,\sigma\, erf(ln(p\,(\alpha-1)+1))}{ln(\alpha)} \tag{11}$$

Median can be derived as

$$X_{0.5} = \frac{\sqrt{2}\,\sigma\, erf^{-1}(ln(0.5\,(\alpha-1)+1))}{ln(\alpha)} \tag{12}$$

5.2 Moments

Assume there is a random variable X, for r a positive integer and if $X \in L^r$, the r^{th} moment of X is

$$E[X^r] = \int_{-\infty}^{\infty} x^r f(x)\, dx.$$

Where L^r is the space consisting of all random variables whose r^{th} absolute power is integrable, and for $1 \leq r < \infty$, L^r denotes the set of random variables X such that $E[|X|^r] < \infty$.

Theorem 3: If a random variable X is from the APTHN distribution, then its rth moment is given by

$$\mu'_r = \frac{\sigma^r \ln(\alpha)}{\alpha - 1}\sqrt{\frac{2}{\pi}}\sum_{k=0}^{\infty}\frac{(\ln(\alpha))^k}{k!}I_{r,k} \tag{13}$$

where

$$I_{r,k} = \int_0^{\infty} u^r e^{-u^2 2}\left(\text{erf}\left(u\sqrt{2}\right)\right)^k du \tag{14}$$

Proof If the random variable X had PDF (6), then the rth moments of X, where X follows the APTHN distribution are calculated as

$$\mu'_{r=} \int_0^{\infty} x^r f_{APT}\left(x;\alpha,\sigma^2\right) dx$$

$$\mu'_{r=} \int_0^{\infty} x^r \frac{\sqrt{2}\left(\alpha^{\text{erf}\left(x\sigma\sqrt{2}\right)} * \ln(\alpha) * e^{-x^2 2\sigma^2}\right)}{\sqrt{\pi}\,(\alpha-1)\,\sigma} dx$$

$$\mu'_{r=} \frac{\sqrt{2}\ln(\alpha)}{\sqrt{\pi}\,(\alpha-1)\,\sigma}\int_0^{\infty} x^r \alpha^{\text{erf}\left(x\sigma\sqrt{2}\right)} e^{-x^2 2\sigma^2} dx$$

By using the exponential series representation

$\alpha^w = \sum_{k=0}^{\infty}\frac{(\ln(\alpha))^k}{k!}w^k$, we have:

$$\alpha^{\text{erf}\left(x\sigma\sqrt{2}\right)} = \sum_{k=0}^{\infty}\frac{(\ln(\alpha))^k}{k!}\left(\text{erf}\left(x\sigma\sqrt{2}\right)\right)^k \tag{15}$$

$$\mu'_{r=}\ \frac{\sqrt{2}\ln(\alpha)}{\sqrt{\pi}\,(\alpha-1)\,\sigma}\sum_{k=0}^{\infty}\frac{(\ln(\alpha))^k}{k!}\int_0^{\infty}x^r e^{-x^2 2\sigma^2}\left(\operatorname{erf}\left(x\sigma\sqrt{2}\right)\right)^k dx$$

By setting $u = x/\sigma$, then $\frac{du}{dx} = \frac{1}{\sigma}$ and $\sigma du = dx$, then $x = u\sigma$

$$\mu'_{r=}\ \frac{\sigma^r\sqrt{2}\ln(\alpha)}{\sqrt{\pi}\,(\alpha-1)}\sum_{k=0}^{\infty}\frac{(\ln(\alpha))^k}{k!}\int_0^{\infty}u^r e^{-u^2 2}\left(\operatorname{erf}\left(u\sqrt{2}\right)\right)^k du$$

$$\mu'_{r=}\ \frac{\sigma^r\sqrt{2}\ln(\alpha)}{\sqrt{\pi}\,(\alpha-1)}\sum_{k=0}^{\infty}\frac{(\ln(\alpha))^k}{k!}I_{r,k}$$

Where $I_{r,k} = \int_0^{\infty}u^r e^{-u^2 2}\left(\operatorname{erf}\left(u\sqrt{2}\right)\right)^k du$

5.3 Mean and Variance of APTHN Distribution.

For a random variable $X \in L^1$, the mean of X is $E[X] = \int_{-\infty}^{\infty} xf(x)dx$, Expectation of X. This can be easily obtained by putting $r = 1$ from rth moment. It is given as

$$\mu = \mu'_{1=}\ \frac{\sigma^1\sqrt{2}\ln(\alpha)}{\sqrt{\pi}\,(\alpha-1)}\sum_{k=0}^{\infty}\frac{(\ln(\alpha))^k}{k!}I_{1,k} \tag{16}$$

Similarly; suppose that the random variable $X \in L^2$, then the variance X is the second central moments.

$$Var\ (X) = E\left[(X - E[X])^2\right] = E\left[X^2\right] - E[X]^2$$

Therefore, the variance of random variable X, where X follows the APTHN distribution is given by $Var\ (X) = E\left[X^2\right] - E[X]^2$, Hence $E\left[X^2\right]$ is the second moment (μ'_2) which is easily obtained by putting $r = 2$ from rth moment. Thus it is given by:

$$Var\ (X) = \mu'_2 - (\mu'_1)^2 = \frac{\sigma^2\sqrt{2}\ln(\alpha)}{\sqrt{\pi}\,(\alpha-1)}\sum_{k=0}^{\infty}\frac{(\ln(\alpha))^k}{k!}I_{2,k} - \mu^2 \tag{17}$$

Moment Generating Function (MGF): The MGF of the random variable X is the function $\psi_x(t) = E[e^{tx}] = \int_{-\infty}^{\infty}e^{tx}f(x)dx$, provided that the expectation occurs for all t in some neighborhood of the origin [9].

The Moment generating Function of random variable X where X follows APTHN distribution is:

$$\psi_x(t) = E\left(e^{tx}\right) = \int_0^{\infty}e^{tx}f_{APT}\left(x;\alpha,\sigma^2\right)dx$$

$$\psi_x(t) = \sum_{r=0}^{\infty}\frac{t^r}{r!}\int_0^{\infty}x^r f_{APT}\left(x;\alpha,\sigma^2\right)dx$$

$$= \sum_{r=0}^{\infty}\frac{t^r}{r!}\mu'_r$$

$$\psi_x(t) = \frac{\sigma^r\sqrt{2}\ln(\alpha)}{\sqrt{\pi}\,(\alpha-1)}\sum_{k=0}^{\infty}\sum_{r=0}^{\infty}\frac{t^r}{r!}\frac{(\ln(\alpha))^k}{k!}I_{r,k}$$

5.4 Characteristic Function

The characteristic function of a random variable X is the function $\varphi_x : \mathbb{R} \to \mathbb{C}$ expressed by: $\varphi_x(t) = E\left[e^{itx}\right] = \int_{-\infty}^{\infty}e^{itx}f(x)dx$, where $\mathbb{R}$ is set of real number and $\mathbb{C}$ complex number (Karr, 1993). The Characteristic function of random variable X, where X follows APTHN distribution is expressed by

$$\varphi_x(t) = E\left(e^{itx}\right) = \int_0^{\infty}e^{itx}f_{APT}\left(x;\alpha,\sigma^2\right)dx$$

$$\varphi_x(t) = \sum_{r=0}^{\infty}\frac{(it)^r}{r!}\int_0^{\infty}x^r f_{APT}\left(x;\alpha,\sigma^2\right)dx$$

$$= \sum_{r=0}^{\infty}\frac{(it)^r}{r!}\mu'_r$$

Hence, characteristic function becomes:

$$\varphi_x(t) = \frac{\sigma^r\sqrt{2}\ln(\alpha)}{\sqrt{\pi}\,(\alpha-1)}\sum_{k=0}^{\infty}\sum_{r=0}^{\infty}\frac{(it)^r}{r!}\frac{(\ln(\alpha))^k}{k!}I_{r,k} \tag{18}$$

Where $i = \sqrt{-1}$ is a complex number

5.5 Order Statistics

Assume $X_1, X_2, \ldots, X_n$ be a random sample taken from APTHN distribution, and let $X_{(1)} \le X_{(2)} \le \cdots \le X_{(n)}$ denote the order statistics. Then, the probability density function of the random variable $X_{(i)}$ is expressed by:

$$g_{X_i}(x) = \frac{n!}{(i-1)!\,(n-i)!}f(x) * F(x)^{i-1}(1-F(x))^{n-i}$$

The PDF of the random variable $X_{(i)}$ can be expressed as

$$g_{X_i}(x) = \frac{n!}{(i-1)!\,(n-i)!}\frac{\sqrt{2}\left(\alpha^{\operatorname{erf}\left(x\sigma\sqrt{2}\right)} * \ln(\alpha) * e^{-x^2 2\sigma^2}\right)}{\sqrt{\pi}\,(\alpha-1)\,\sigma}\left(\frac{\alpha^{\operatorname{erf}\left(x\sigma\sqrt{2}\right)}-1}{\alpha-1}\right)^{i-1}\left(1-\frac{\alpha^{\operatorname{erf}\left(x\sigma\sqrt{2}\right)}+1}{\alpha-1}\right)^{n-1} \tag{17}$$

In particular, the PDF of the first and last order statistics of the random variable X can be derived as

$$g_{X_1}(x) = \frac{n\sqrt{2}\ln(\alpha)\alpha^{\text{erf}\left(x\sigma\sqrt{2}\right)}e^{-x^2 2\sigma^2}}{\sqrt{\pi}\ (\alpha-1)^n\ \sigma}\left(\alpha-\alpha^{\text{erf}\left(x\sigma\sqrt{2}\right)}\right)^{n-1}$$

$$g_{X_n}(x) = \frac{n\sqrt{2}\ln(\alpha)\alpha^{\text{erf}\left(x\sigma\sqrt{2}\right)}e^{-x^2 2\sigma^2}}{\sqrt{\pi}\ (\alpha-1)^n\ \sigma}\left(\alpha^{\text{erf}\left(x\sigma\sqrt{2}\right)}-1\right)^{n-1}$$

6 Maximum Likelihood Estimation of Parameters

The population parameters of the APTHN distribution can be estimated using maximum likelihood estimation (MLE) method. It derivation is shown below.

Suppose $X_1, \ldots, X_n$ be n independently identically distributed random observations from $f_{\text{APTHN}}(\boldsymbol{x};\boldsymbol{\theta})$ with $\boldsymbol{\theta} = (\alpha, \sigma^2) \in \Omega = [0,\infty) \times [0,\infty)$ in parameter space a subset of 2-dimensional $\mathbb{R}^2$. The likelihood function $L(\boldsymbol{\theta}|\boldsymbol{x})$ is given by $L(\boldsymbol{\theta}|\boldsymbol{x}) = \prod_{i=1}^{n} f(x_i;\boldsymbol{\theta})$. The values of $\boldsymbol{\theta}$ that maximizes $L(\boldsymbol{\theta}|\boldsymbol{x})$ is a maximum likelihood estimators (MLEs) $\hat{\boldsymbol{\theta}}$ of $\boldsymbol{\theta}$ [17].

Thus, unique solution MLE $\hat{\boldsymbol{\theta}}$ is obtained by optimization problem approach as:

$$\hat{\boldsymbol{\theta}} = \frac{\arg\max}{\boldsymbol{\theta}\in\Omega} L(\boldsymbol{\theta}|\boldsymbol{x}) \tag{19}$$

$$(\hat{\alpha}, \hat{\sigma}^2) = \frac{\arg\max}{(\alpha,\sigma^2)\in\Omega} \prod_{i=1}^{n} f_{\text{APT}}(\boldsymbol{x};\alpha,\sigma^2) \tag{20}$$

Alternatively, we can find the solution by log-likelihood function. By substituting equation (6) in to equation (21) and taking the logarithm of the function, we found the log-likelihood function $\log(L)$ which is given by:

$$\log(L) = \log\left(\prod_{i=1}^{n} \frac{\sqrt{2}\left(\alpha^{\text{erf}\left(x\sigma\sqrt{2}\right)} * \ln(\alpha) * \exp(-x^2 2\sigma^2)\right)}{\sqrt{\pi}\,(\alpha-1)\,\sigma}\right)$$

$$\begin{aligned}\log(L) &= \frac{n}{2} * \log\left(\frac{2}{\pi}\right) + \sum_{i=1}^{n} \text{erf}\left(\frac{x_i}{\sigma\sqrt{2}}\right) * \log(\alpha) \\ &\quad + n * \log(\log(\alpha)) - \sum_{i=1}^{n} \frac{x_i^2}{2\sigma^2} - n * \log(\alpha-1) \\ &\quad - n * \log(\sigma)\end{aligned}$$

By taking partial derivatives for $\log L$ with respect to both α and σ respectively, we get

$$\frac{\partial \log(L)}{\partial \alpha} = \frac{\sum_{i=1}^{n} \text{erf}\left(\frac{x_i}{\sigma\sqrt{2}}\right)}{\alpha} + \frac{n}{\alpha * \ln(\alpha)} - \frac{n}{\alpha-1}$$

$$\begin{aligned}\frac{\partial \log(L)}{\partial \sigma} &= -\frac{\sqrt{2} * \ln(\alpha) \sum_{i=1}^{n} x_i \exp(-x_i^2 2\sigma^2)}{\sqrt{\pi}\sigma^2} \\ &\quad + \sum_{i=1}^{n} \frac{x_i^2}{2\sigma^3} - \frac{n}{\sigma}\end{aligned}$$

The MLE of both α and σ can be found by resolving the above two nonlinear equations by equating $\frac{\partial \log(L)}{\partial \alpha} = 0$ and $\frac{\partial \log(L)}{\partial \sigma} = 0$, by using the numerical approach using such methods as Newton-Raphson and Nelder–Mead methods (Roussas, 2003). They numerically find minimum or maximum of an objective function in a multidimensional space. Note that the estimators $\hat{\alpha}, \hat{\sigma}^2$ are random variables and so they have their own distributions, means and variances. MLE estimate $\hat{\theta}_n$ is consistent and converges in probability to the true value as sample size n goes to infinity (Karr, 1993; Roussas, 2003).

Simulation Studies with Acceptance-Rejection Algorithm

Four simulations of the APTHN distribution are conducted using the true values $\alpha \in \{0.5, 3\}$ and $\sigma \in 1, 2$. The acceptance-rejection AR algorithm proposed by (Casella & Berger, 2002) is applied here in order to generate random observations from the new APTHN distribution. The half-normal pdf is used as a proposal density in the algorithm. Accepted samples are exact observations from the new distribution used. Iterations of 100000 are run, and accepted samples are plotted in Figure 11. The true pdfs are estimated using the histograms and density functions. The parameters are estimated from the random observations using the maximum likelihood estimation method.

The results of the four simulation studies demonstrate that the new density function has different shapes covering large intervals when larger variance compared to the smaller value. The newly included parameter α also greatly affects the shape and skewness of the density function.

7 Parameter Estimation using MLE Method

For the simulation studies, we generate samples of increasing sample sizes from the new distribution with given parameter values and estimate them back using the MLE method. The recital of the MLE is measured using the mean square error and bias for each case. Many sample sizes are considered in the experiments at sizes n =150, 300, 500, 1000, and 5000. In addition, the different values of parameters and are considered. The MLE estimates asymptotically converge in probability to the true parameter values, and the solution is unique. The results in Table 1 display estimates of MLE, MSE and bias for three different cases. The results show that as sample size increases,

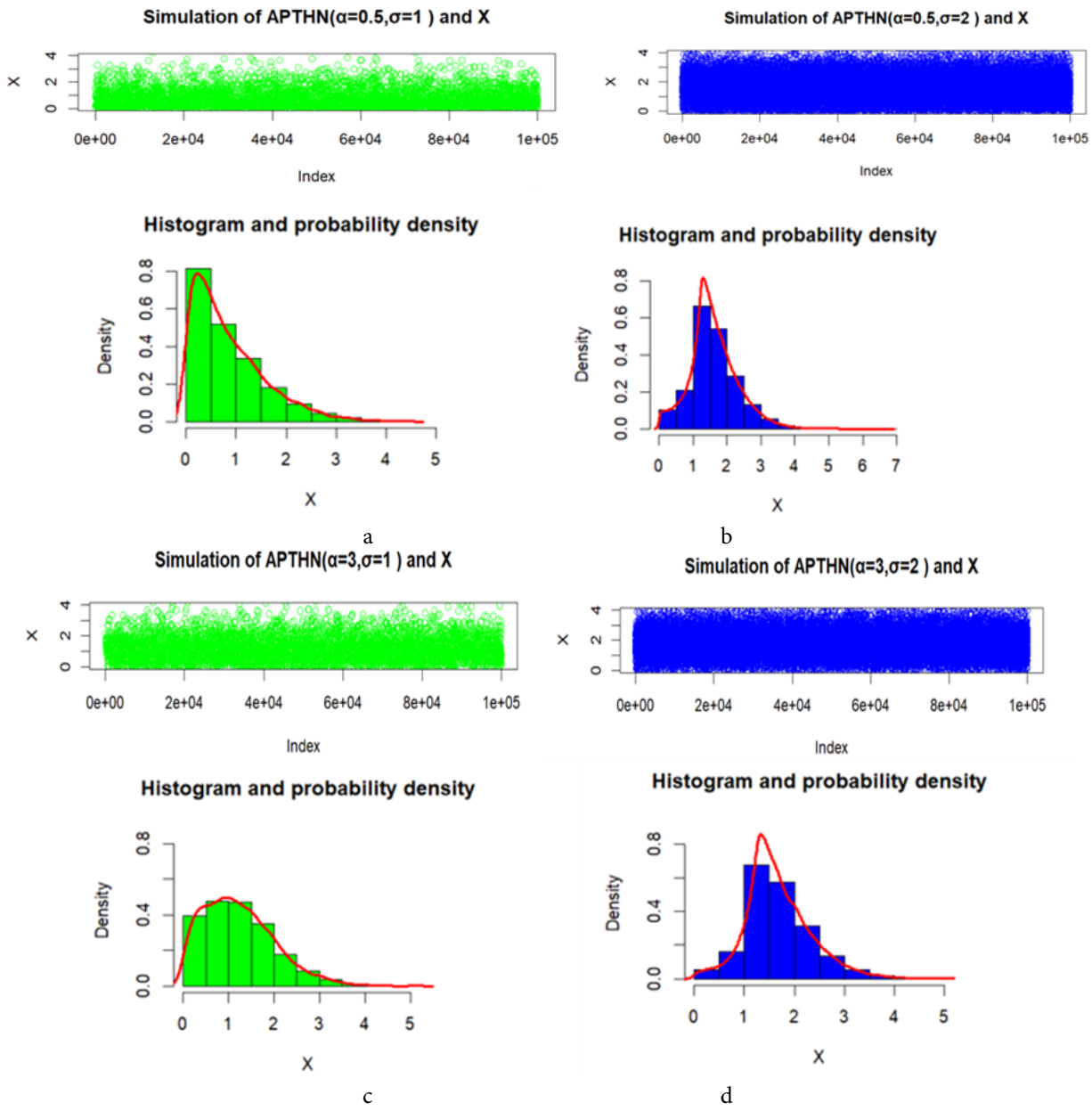

Figure 11: Plots of realization and respective histogram of the case of (a) $\alpha = 0.5$, $\sigma = 1$; (b) $\alpha = 0.5$, $\sigma = 2$; (c) $\alpha = 3$, $\sigma = 1$; (d) $\alpha = 3$, $\sigma = 2$.

the parameter estimates approach to the true value, with the respective MSE and bias-computed values both approaching zero. This holds to be true for each case of the three scenarios.

8 Model Comparison in Fitting to Three Datasets

Applications of the model to two real datasets and one simulated datasets were carried out to see the performance of the proposed APTHN distribution as compared to related one parameter existing distributions, which are half normal distribution (HND), exponential distribution (EXPD), Lindley distribution (LD), XLindley distribution (XLD), and XGamma distribution (XGD). The criteria employed are Anderson-Darling (A), Cramér-von Misses (W), Akaike information criterion (AIC), Bayesian information criterion (BIC), consistent Akaike information criterion (CAIC), and HQIC (Hannan-Quinn information criterion). The distribution with the smallest values of AIC, BIC, and CAIC is considered the best model for the given data.

First, a dataset taken from Nichols and Padgett (2006) is used and it is named the breaking stress data. This dataset includes 100 carbon fiber breaking stress observations (in GPa). Several authors have utilized these data to demonstrate how various competing models can be applied. Table 2 provides the numerical outcomes of a few goodness of fit metrics. The new model APTHND has the lowest values of BIC, AIC, CAIC, and HQIC. Based on these criteria, we found that the APTHND model best fits the breaking stress data as compared to the HND, EXPD, LD, XLD, and XGD models.

Table 1: MSE and bias based on simulations from APTHN model

Parameters True Values	n	$\hat{\alpha}$	MSE ($\hat{\alpha}$)	Bias ($\hat{\alpha}$)	$\hat{\sigma}$	MSE ($\hat{\sigma}$)	Bias ($\hat{\sigma}$)
$\alpha = 8$ $\sigma = 0.3$	150	5.4402	6.5523	2.5598	0.3249	6e-04	0.0249
	300	5.8983	4.4171	2.1017	0.3108	1e-04	0.0108
	500	6.8458	1.3323	1.1542	0.3032	9e-05	0.0032
	1000	7.8323	0.0281	0.1677	0.2966	1e-05	0.0015
	5000	8.0543	0.0029	0.0543	0.2932	4e-06	0.0007
$\alpha = 6$ $\sigma = 1$	150	3.8718	4.5292	2.1282	1.2406	0.0579	0.2406
	300	5.7930	1.2076	1.2070	1.1659	0.0275	0.1659
	500	7.0989	0.4335	1.0989	1.1378	0.0190	0.1378
	1000	6.6584	0.0429	0.6584	1.1194	0.0142	0.1194
	5000	5.9841	0.0003	0.0159	1.1292	0.0037	0.0292
$\alpha = 3$ $\sigma = 1$	150	2.7260	0.2751	0.2741	1.2475	0.0612	0.2475
	300	2.7706	0.1686	0.2106	1.1781	0.0317	0.1781
	500	2.8061	0.1281	0.1361	1.1515	0.0229	0.1515
	1000	2.9231	0.0284	0.0731	1.1469	0.0216	0.1169
	5000	2.9948	0.0090	0.0147	1.0091	0.0013	0.0191

Table 2: Measures of goodness of fits for breaking stress of carbon fiber data

Distribution	Par	MLE	W	A	AIC	CAIC	BIC	HQIC	Value
APTHND	α	3.05	0.062	0.401	749.50	749.63	754.71	751.61	372.75
	σ	3.21							
HND	σ	1.19	0.059	0.401	836.10	836.14	838.71	837.15	417.05
EXPD	λ	0.8	0.214	1.119	951.15	951.19	953.75	952.20	474.57
LD	θ	0.4	0.167	0.851	977.99	978.03	980.59	979.05	487.99
XLD	θ	0.6	0.153	0.782	847.38	847.42	849.98	848.43	422.69
XGD	θ	0.15	0.133	0.692	785.75	785.79	788.36	786.81	391.88

The second dataset consider for this paper is pharmacokinetics of indomethacin data, which explains plasma concentrations of indomethacin (mcg/ml). The dataset was analyzed by authors (Davidian & Giltinan, 1995; Kwan et al., 1976; Pinheiro & Bates, 2000). Table 3 displays the results of goodness of fit criteria including W, A, AIC, CAIC, BIC, and HQIC for aircraft failure times data. The AIC and BIC value in Table 3 is relatively lower for the new distribution as compared to other distributions. The APTHN distribution performs relatively better compare to the half normal, exponential, Lindley, xLindley and xgamma distributions. The fitting plots are displayed in Figure 12.

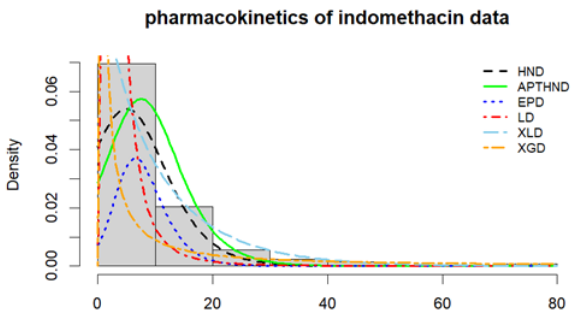

Figure 12: PPlots of fitted models to the pharmacokinetics of indomethacin data

The third dataset is one simulated data from APTHN distribution by using AR algorithm, with α=3, and σ=1. The data consists of 200 random samples. The data fitting results are given in in Table 4. The results show that the values of AIC, CAIC, BIC and HQIC are all lowest for the APTHN distribution among all models applied. The APTHN distribution still performs best.

The six distributions are fitted to three datasets including real and simulated datasets. The results show that performance of the newly suggested APTHN distribution is found to be interestingly the best. The new model is promising and so it deserves to be tested in other applications and further studies.

9 Conclusions

The purpose of this study is to develop a new continuous probability distribution using the Alpha Power Transformation (APT) method using the base Half-Normal distribution. The proposed Alpha Power Transformed Half-Normal (APTHN) distribution represents a novel contribution to statistical theory. Several statistical properties of the APTHN distribution are derived and discussed in detail. Its hazard function exhibits flexible and interesting shapes, while its probability density and cumulative distribution functions differ significantly from those of the base half-normal distribution. The performance of the proposed APTHN distribution was evaluated using one simulated dataset and two real datasets, where it outperformed six existing distributions in terms of goodness of fit. Statistical

Table 3: Measures of goodness of fits for pharmacokinetics of indomethacin data

Distribution	Par	MLE	W	A	AIC	CAIC	BIC	HQIC	Value
APTHND	α	0.19	0.263	1.692	68.91	69.10	73.29	70.64	32.45
	σ	0.8							
HND	σ	3.57	0.294	1.890	80.93	80.99	83.12	81.80	39.47
EXPD	λ	0.89	0.232	1.486	151.64	151.70	153.83	152.50	74.82
LD	θ	1.49	22.373	129.700	189.23	189.29	191.42	190.10	93.61
XLD	θ	0.87	0.239	1.538	109.15	109.21	111.34	110.02	53.58
XGD	θ	1.45	0.222	1.437	102.89	102.96	105.08	103.76	50.45

Table 4: Measures of goodness of fits for simulated data using $\alpha = 3$, and $\sigma = 1$

Distribution	Par	MLE	W	A	AIC	CAIC	BIC	HQIC	Value
APTHND	α	3.01	0.063	0.462	426.67	426.73	433.26	429.34	211.33
	σ	0.91							
HND	σ	2.08	0.031	0.259	446.4	446.5	453	449.1	221.2
EXPD	λ	0.059	0.293	1.798	1152.7	1152.8	1156.1	1154.1	575.4
LD	θ	0.053	0.095	0.747	2345.6	2345.7	2348.9	2347	1171.8
XLD	θ	0.089	0.206	1.266	1590.6	1590.7	1593.9	1592	794.3
XGD	θ	0.39	0.209	1.277	947.9	947.9	951.3	949.3	472.9

inferences including model fitting, parameter estimation, and simulation studies demonstrate that the new distribution provides valuable insights for applied probability, applied statistics, and various practical fields such as life sciences. The results of this study can serve as a foundation for future research and model development in these areas.

Acknowledgements

The author would like to forward heartfelt gratitude to Department of Mathematics of Kotebe University of Education for providing the essential facilities and support that contributed to the successful completion of this research.

Funding

No financial support was received for this particular study.

Conflicts of Interest

The authors declare that there are no conflicts of interest.

References

Alizadeh, M., Afify, A. Z., Eliwa, M. S., & Hamedani, G. G. (2021). A new two-parameter lifetime distribution: Properties, applications and different method of estimations. *Statistics, Optimization & Information Computing*, *7*(2), 291–310.

Alizadeh, M., Nasiri, V., Ghosh, S., & Tahir, M. H. (2020). The kumaraswamy half-normal distribution: Properties and applications. *Communications in Statistics - Theory and Methods*, *49*(24), 5813–5829.

Alshenawy, R. (2022). The generalization inverse weibull distribution related to x-gamma generator family: Simulation and application for breast cancer. *Journal of Function Spaces*, *2022*, 17.

Altun, E., Yousof, H. M., & Hamedani, G. G. (2018). A new generalization of generalized half-normal distribution: Properties and regression models. *Journal of Statistical Distributions and Applications*, *5*(1).

Bader, A., Rajab, A., Al-Hussaini, E. K., & El-Helbawy, A. A. (2022). On the mixture of normal and half-normal distributions. *Mathematical Problems in Engineering*, *2022*.

Bousseba, F. Z., & Sakr, A. (2025). Square transformed half normal distribution with its properties and applications. *Journal of Contemporary Applied Mathematics*, *15*(2).

Casella, G., & Berger, R. L. (2002). *Statistical inference* (2nd Edition ed).

Chouia, S., & Zeghdoudi, H. (2021). The xlindley distribution: Properties and application. *Journal of Statistical Theory and Applications*, *20*(2), 318–327.

Cordeiro, G. M., Nadarajah, S., & Ortega, E. M. M. (2016). The exponentiated half-normal distribution: Properties and applications. *Journal of Statistical Computation and Simulation*, *86*(4), 1151–1167.

Davidian, M., & Giltinan, D. M. (1995). *Nonlinear models for repeated measurement data*. Chapman & Hall/CRC.

Karr, A. F. (1993). *Probability*. Springer Science+Business Media.

Kwan, K. C., Breault, G. O., Umbenhauer, E. R., McMahon, F. G., & Duggan, D. E. (1976). Kinetics of indomethacin absorption, elimination, and enterohepatic circulation in man. *Journal of Pharmacokinetics and Biopharmaceutics*, *4*(3), 255–280.

Mahdavi, A., & Kundu, D. (2017). A new method for generating distributions with an application to exponential

distribution. *Communications in Statistics - Theory and Methods*, *46*(13), 6543–6557.

Mohiuddin, M., & Kannan, R. (2021). Alpha power transformed aradhana distributions, its properties and applications. *Indian Journal of Science and Technology*, *14*(31), 2483–2493.

Mohiuddin, M., & Kannan, R. (2022). A review: Alpha power transformation family of distributions. *Appl. Math. Inf. Sci. Lett.*, *10*(1), 1–21.

Nadarajah, S., & Kotz, S. (2006). The beta half-normal distribution. *Statistical Papers*, *47*(4), 505–518.

Nichols, M., & Padgett, W. J. (2006). A bootstrap control chart for weibull percentiles. *Quality and Reliability Engineering International*, *22*(2), 141–151.

Pinheiro, J. C., & Bates, D. M. (2000). *Mixed-effects models in s and s-plus*. Springer.

R Core Team. (2023). *R: A language and environment for statistical computing*. R Foundation for Statistical Computing. Vienna, Austria. https://www.R-project.org/

Roussas, G. (2003). *Introduction to probability and statistical inference*. Elsevier Science.

Sen, S., Maiti, S. S., & Chandra, N. (2016). The xgamma distribution: Statistical properties and application. *Journal of Modern Applied Statistical Methods*, *15*(1).

Wallner, M. (2020). *A half-normal distribution scheme for generating functions*. arXiv: 1610.00541v3 [math.CO].

East African Journal of Biophysical and Computational Sciences
ISSN (Online): 2789-3618 and ISSN (Print): 2789-360X

ARTICLE

Journal Information

Volume 6(2), 2025
DOI: https://dx.doi.org/10.4314/eajbcs.v6i2.4S

Homepage:
https://journals.hu.edu.et/hu-journals/index.php/eajbcs

Article History

Received: 09 October, 2025
Accepted: 24 November, 2025
Published Online: 25 December, 2025

How to cite

Ayele B. (2025). Evaluating Rock Construction Materials Using Petrography, Engineering Properties and Geophysical Investigation Around Hawassa, Sidama, Ethiopia. *East African Journal of Biophysical and Computational Sciences* Volume 6(2), 2025, 38-50

Open Access

Evaluating Rock Construction Materials Using Petrography, Engineering Properties and Geophysical Investigation Around Hawassa, Sidama, Ethiopia

Bekele Ayele[1,*]

[1]Department of Geology, College of Natural and Computation Sciences, Hawassa University, P.O Box 05

*Corresponding author: bekelegeo@gmail.com or bekeleay@hu.edu.et

Abstract

The petrographic description, engineering physical properties, and resistivity characteristics of rock construction materials determining the quality, durability and economic efficiency of infrastructures. The study area is situated at the marginal settings in the central and southern part of main Ethiopian rift, comprises diverse volcanic and pyroclastic rocks that are widely used in the varies construction materials but poorly characterized. The civil engineering infrastructures in Hawassa city and the Sidama regional state are deteriorating due to the inappropriate use of rock materials. Comprehensive studies on these construction materials have not yet been carried. The objective of the study was to evaluate quality of rock construction materials using petrography analysis, engineering physical property assessments and geophysical investigation. To attain this objective, 24 petrographic descriptions, 10 rocks engineering properties and 5 resistivity survey data were analyzed. The rock construction materials identified in the study area, including andesite, scoria, rhyolitic ignimbrite, ignimbrite, welded tuff, and pumice. From these, the andesite rock is composed of pyroxene (60%), plagioclase (35%), biotite (10%), and muscovite (10%) minerals, whereas the rhyolitic ignimbrite shows a flow banding texture, which contains feldspar (40%), plagioclase (25%), biotite (15%), quartz (10%), and volcanic glass (10%) minerals. The dominant structures of the study include joints, cracks, and faults are oriented NE to SW which controlled by main Ethiopian Rift system. The vertical electrical sounding results indicate that the Alamora andesite outcrops, the Boricha quarry site and Gemeto Gale area contain a potential rock layer that suitable for various infrastructures. The lowest and highest compressive strengths are observed in the Galoko Haro quarry site and Alamora andisite rock, which have values ranging from 8 N/mm² to 300.5 N/mm², respectively. The study identified potential rock for sustainable use in various infrastructure developments, providing a foundational dataset for researchers and the Sidama Regional State Mining and Energy Bureau.

Keywords: Characteristic; Rock Construction; Quarry Site; Resistivity; Sidama; Ethiopia

East African Journal of Biophysical and Computational Sciences (EAJBCS) is already indexed on known databases like AJOL, DOAJ, CABI ABSTRACTS and FAO AGRIS.

1 Introduction

Main Ethiopian rift is part of the east African rift system and is an active continental rift that extends from the Afar Depression in the northeast to the Omo Rift in the southwest (Corti, 2009; WoldeGabriel et al., 1990). It consists of northern, central and southern sectors, which differentiated by their deformational patterns and volcanic activity (Corti et al., 2020). The Northern Main Ethiopian Rift (NMER) is dominated by active volcanism, the Central Main Ethiopian Rift (CMER), shows moderate volcanic system alongside fault activity, whereas the southern (SMER) is characterized by minimal volcanism (Keir et al., 2006; Muluneh et al., 2021).

Hawassa and its surrounding geological settings lies within the central and southern Main Ethiopian Rift (MER). Regional geology of the central and southern (MER) sector is characterized by felsic, intermediate, and mafic volcanic rocks, often associated with caldera-forming volcanic phases and lacustrine sediments (Abebe et al., 2007; Hutchison, 2015; Peccerillo et al., 2003). Evaluating the properties of massive rock materials determines their suitability for the construction industry (Ahmad & Jamin, 2018; Alshkane, 2020). The inappropriate uses of these rock construction materials might challenge the geotechnical engineers. The assessment of subsurface rock layers, geophysical resistivity measurements, and geotechnical studies affect the civil engineering design (Butchibabu et al., 2019; Zhang et al., 2015). The study area, extending from Hawassa to Yirgalem, is located in the central and partially in the southern parts of the main Ethiopian rift and includes the Hawassa Caldera which hosts Lake Awassa. According to Japan International Cooperation Agency (JICA) (2012), the Hawassa caldera resulted from the large ignimbrite volcanic eruptions (Žáček et al., 2014, 2015). The caldera composed of three stages of voluminous ignimbrite volcanic eruptions, dated at about 0.9, 0.67 and 0.2 Ma, respectively (Japan International Cooperation Agency (JICA), 2012; Žáček et al., 2014). Nowadays, the construction industry extensively uses appropriate rock materials for structural loading, foundations, roads, fencing, pavements and cobblestone. It is obvious that a variety of civil engineering construction projects have been implemented around Hawassa and Yirgalem. Hence, local and regional infrastructures, such as roads, housing developments, huge buildings, bridges, etc., need a sufficient supply of suitable rock quarry products. Despite the Sidama Regional State's abundance of geologic construction materials and diverse socio-economic contexts, the potential quarry sites for rock construction materials have not been thoroughly studied. In addition, the rock construction material quarry sites are not well investigated and identified. The main objective is to evaluate quality of rock construction materials using petrography descriptions, engineering properties analysis, and geophysical survey techniques at a scale of 1:50,000 unit. To map and characterize these geological constructions resources, field investigation, laboratory analysis (i.e., thin-sectioned, rock engineering properties) and resistivity survey were applied to understand the rock construction characteristics. According to Goodman (1992), volcanic rocks are widely used as engineering material worldwide, serving as aggregates in cement and asphalt concrete, rock fill dams, railway ballast, and highway base. These geologic quarry resources have been shown to be a potential contributor to the socio-economic growth of unemployed local people of the region, and Ethiopia as a whole. Gravel and cobblestone roads often constitute the majority of the public road network in the Sidama regional state. Since the geologic materials are used for infrastructures (i.e., gravel and cobblestone roads), it is also possible to use it for building construction. Like any other standard type of road, the construction of quality gravel and cobblestone road requires sound engineering knowledge and vocational skills to secure the desired. The decorative dimension stone becoming very popular for the fascinating architects of modern buildings. These dimension stones were sold in either natural broken sizes or shapes. Engineers usually use without adequate justification of the quality of the rock material according to the requirements in different infrastructure construction works. Therefore, to assess the geological resources, a scientific study was conducted involving quarry site mapping and evaluation of the quality of construction rock materials to address the aforementioned issues. The integrated results and analysis of rock samples characterized the engineering properties of the rocks and identified potential geological quarry sites for sustainable uses and resource management in the construction industry. The results of this study, provided the fundamental database that supporting geological resource mapping and the identification of potential construction rock quarry sites. Hence, it is intended to assist researchers, governmental bodies, policymakers, and the Sidama Regional State Mining and Energy Bureau in making decisions regarding economic quarry site licensing and sustainable resource development.

2 Objectives

2.1 Main Objective

The main objective of this study is to evaluate valuable quality of rock construction materials using petrography, engineering properties, and geophysical investigation around Hawassa, Sidama Regional State, Ethiopia.

2.2 Specific Objectives

The specific objectives of the study are:

- To explore petrographic analysis and rock engineering properties
- To investigate geophysical resistivity surveys to identify subsurface lithological natures and characterize the quality of available rock construction materials
- To produce a geological map at a 1:50,000 scale and classify rock construction materials

2.3 Description of the study area

The study area Hawassa to Yirgalem is situated in the Sidama regional state. It is part of the the central and partial southern (MER) and it is bordered in the south by Aleta Wondo, in the east by Hula and Shebedino, in the north by Hawassa city and Shebedino, and in the west by Dale and Shebedino woredas, respectively (Fig. 1). Geographically, it is bounded in the Adindan Mean Universal Transverse Mercator (UTM) zone 37N, between 430000–450000 E and 746000–779800 N. The total land cover of the study locality is about 750 km². The site is accessible through main route from Addis Ababa, the capital city of Ethiopia via Hawassa city and reached through unpaved roads to the study locality (Fig. 1b, c). It forms gentle topography in the central section and moderate cliffs in the eastern and northwestern parts of the study area. The maximum and minimum altitude of the study locality range from 3000 to 1700 meters above sea level, respectively. In general, the study area shows a gradient towards the north and northwestern directions. The climatic parameters of the study area contain arid to semiarid and register the mean annual temperature range 11°C and 33°C, with an annual rainfall of 678–1286 millimeter's (Hawassa Meteorological Agency, 2010).

3 Materials and Methods

The study design and approaches were based on the specific characteristics of the locality and objective of the survey. Field data were gathered on rocks and geophysical resistivity. To meet the goals of the research mentioned, petrography descriptions and rock engineering properties were examined and geophysical resistivity data were analyzed. The geological tools required for the completion of the work include a basemap map at 1:50,000 scale, satellite image, Terrameter SAS 300B™, Brunton compass, Geographic Positioning System, geological hammer, sample bag, petrographic microscope and computer software. The integrated study methodology is illustrated below in Figure 2.

3.1 Sample collection procedures

There were about 36 rock samples, and 5 geophysics resistivity surveys were collected from different localities within the study area. The representative rock samples are collected and properly coded with Parker, kept in the sample bag, and taken to the laboratory for petrographic and rock engineering property analysis. Among the collected rock samples, 24 thin-sections and 10 rock engineering tests were analyzed in the petrographic and geotechnical laboratory at the Geological Institute of Ethiopia, Addis Ababa, respectively. Whereas 5 geophysics resistivity survey measurements are recorded during the fieldwork. These rock samples, structural data, and geophysics resistivity locations are shown (Fig. 4). The laboratory procedural techniques used for analysis have been different for thin-section and rock engineering cases and resistivity measurements are explained as follows:

3.2 Thin-section analysis

Out of the total 36 rocks sampled that were collected, only 24 samples were prepared for thin-section analysis and interpretation. The rock samples were cut by using the rock-cutter at the petrological laboratory in Geological Institute of Ethiopia to produce slabs of about 4x2 cm size. All the prepared thin-sections were studied for petrographic details using a transmitted light microscope in the laboratory of the Geological Institute of Ethiopia.

3.3 Geophysical Terrameter Electrical Resistivity Survey

This resistivity survey is collected using electrode resistivity (Schlumberger), which comprise of a transmitter and receiver. The Terrameter SAS 300B™ device involved for the vertical electrical sounding (VES) measurements (Fig. 3a). It is used to measure and detect resistance (ΔV/I), through apparent resistivity computed. The apparent resistivity values detect by increasing the electrode spacing against the half electrode separation (AB/2) to produce the field resistivity curve (Fig. 3b). An electrical current was run through a pair of electrodes (A and B) placed at varies points symmetrically from a central point, while a pair of electrodes (M and N) measured the surface features (Fig. 3b). The separations of the current electrodes (AB/2) were 1.13, 1.68, 2.18, 3.66, 4.74, 6.15, 7.96, 10.33, 13.38, 17.35, 22.49, 37.75, 48.78, 63.48, 82.27, and 106.6 m. The spacings were specific to carry out VES, which provides more lithological detail at shallow depths.

After detailed surface geological investigations, 5 vertical electrical sounding (VES) localities are selected and conducted within the study locality. The VES data was interpreted using lithological layers knowledge and its resistivity values of the subsurface formations. The location of VES points and UTM coordinates are illustrated below in Table 1.

3.4 Rock Engineering Properties Analysis Techniques

Ten rock samples are analyzed at the laboratory of Geological Institute of Ethiopia to determine rock engineering properties including compressive strength, bulk density, porosity and water absorption. Initially, the rock samples were cut using a rock cutter for rock engineering properties analysis to the standard BS 1377 part 1:1990 in the laboratory. Rock density was determined by measuring bulk mass, saturated-surface-dry mass, and submerged mass, allowing calculation of bulk volume and density. Porosity and water content were measured using the same procedure after drying samples at 105°C to constant mass, and cooled for 30 minutes in a desiccator, and the dry mass (Mdry) is measured. Compressive strength was tested on prepared cylindrical samples instrumented with axial and circumferential LVDTs and loaded at a constant strain rate until failure. Strength was calculated from the failure load and initial cross-sectional area.

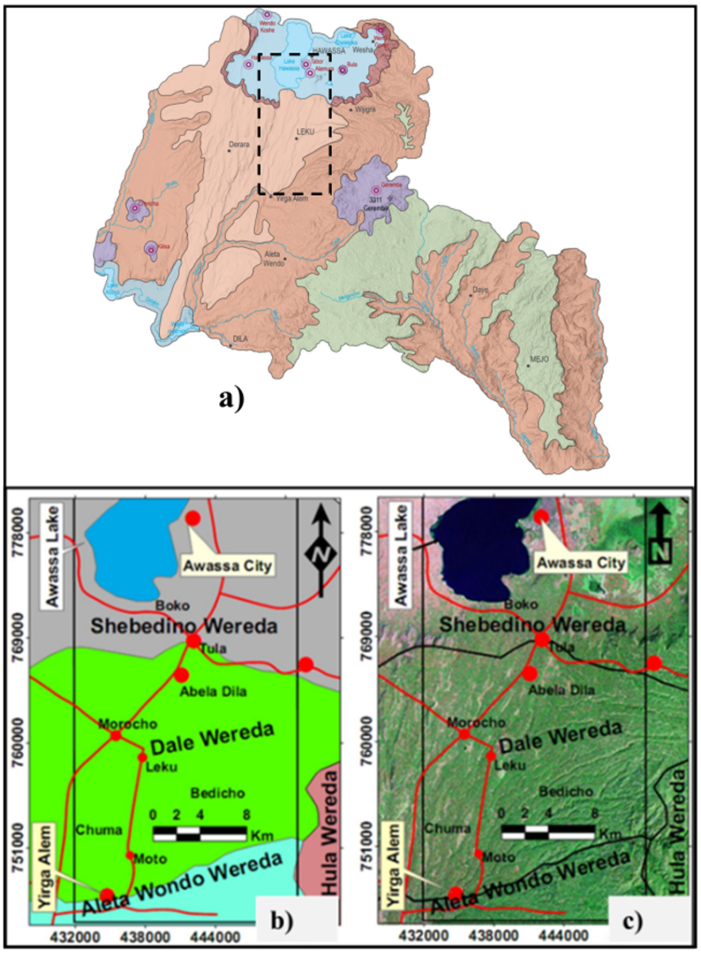

Figure 1: a) Schematic map of Sidama Regional State. b) Location and accessibility of the study area (inset broken rectangular) with respect to surrounding Sidama woredas, and c) Satellite with accessibility image of the study area.

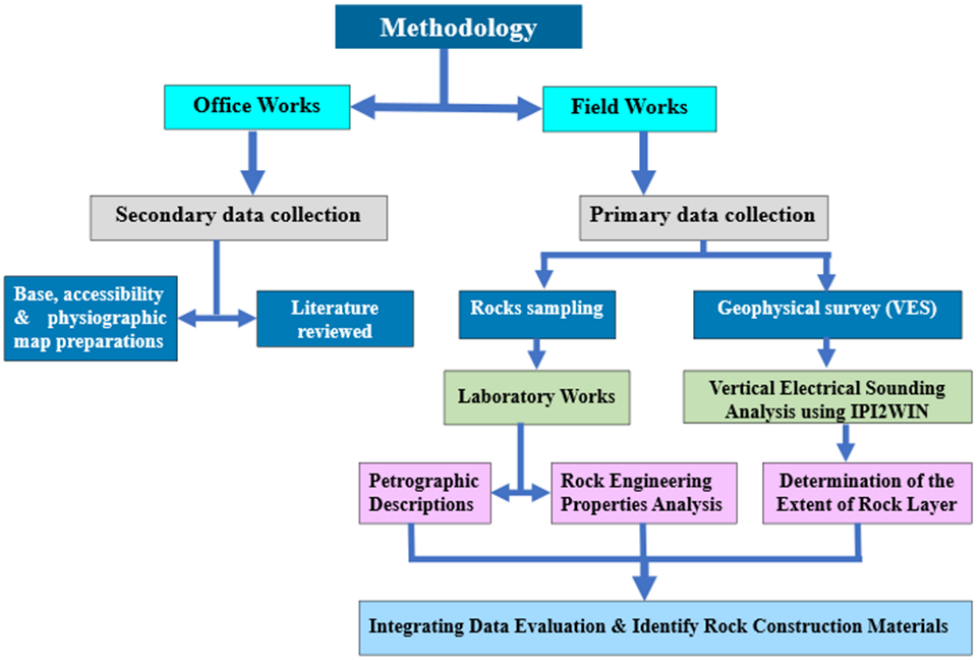

Figure 2: The general workflow of the study

3.5 Data Management and Analysis

The collected primary and secondary data are intended to be analyzed in line with mentioned objective. Data obtained from

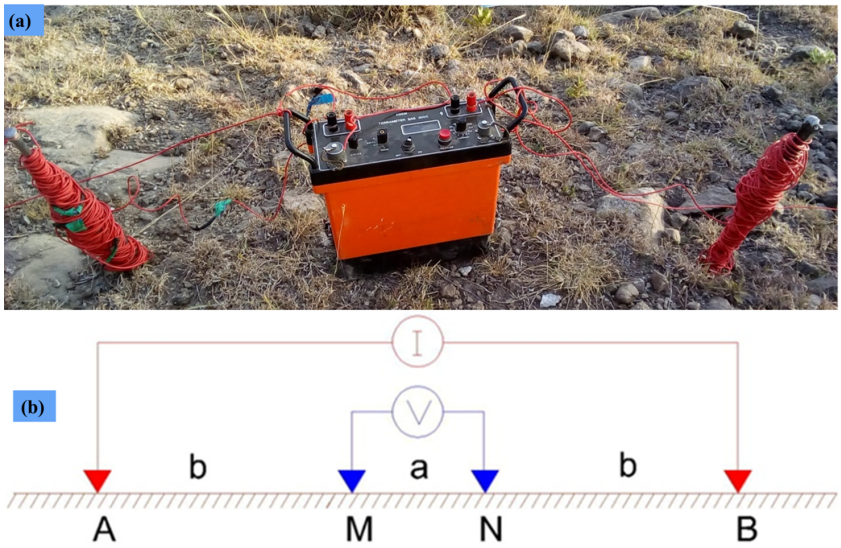

Figure 3: (a) Electrical resistivity test during geophysical survey for data acquisition. (b) Schlumberger Electrode Configuration.

Table 1: Location of VES point within the study area.

VES No.	Elevation (m)	Easting	Northing	Site Name and Landform
VES 1	1716	434614	770860	Crack Area
VES 2	1905	432747	762418	Boricha Ridge
VES 3	1811	437491	754395	Tariku Kaba Spot (Dale Woreda)
VES 4	1738	443453	773236	Gemto Gala kebele
VES 5	1709	447250	772814	Filwha area

fieldwork and laboratory analysis were organized, processed, and interpreted. The data analysis and evaluations involved the determination of rock constructions characteristics and identifications.

4 Results

4.1 Lithology and Petrography

A surface and subsurface investigation was carried out in the study area Hawassa to Yirgalem with the aim of evaluating the rock construction materials potential and quality. The rocks of the study area specifically comprise andesite, scoria, rhyolitic ignimbrite, ignimbrite, unwelded ignimbrite, lithic ignimbrite, welded tuff, unwelded tuff, pumice, colluvial sediment, and lacustrine sediment (Fig. 4).

Andesite unit

This unit was mapped in the north-central part of the study locality (Fig. 4). This rock is mainly exposed on the gentle south cliff of Alamora Mountain (Fig. 5). The andesite hand specimen description is dark grey and fine-grained texture.

Microscopically, thin section observation of the rock composition shows pyroxene (60%), plagioclase (35%), biotite (10%), and muscovite (10%) minerals (Plate 1). The contacts with the adjacent lithological units in the eastern, northern, and southern areas are unwelded ignimbrite, rhyolitic ignimbrite, and unwelded ignimbrite, respectively.

Scoria Unit

Scoria is mapped in the north-central part of the study area, and mainly exposed as a scoria domes. Scoria is glassy in composition and resulted from a vent during explosive eruption. The scoria hand specimen description is red to dark gray to black and show vesicular texture.

Rhyolitic Ignimbrite Unit

The rhyolitic ignimbrite with subordinate pyroclastic deposit is produced by voluminous eruption of rhyolitic magma ejected from the Hawassa Caldera (Rapprich et al. 2013). The out-crop samples and hand specimen description is light gray and develops a flow-banded texture (Fig. 6).

The thin-sections were observed under a transmitted light microscope with a magnification of 4x (objective) and 10 x (ocular). Based on petrographic information, the lithologies are named as rhyolitic ignimbrite rock. Microscopically, thin sections were observed under a transmitted light microscope with a magnification of 4x (objective) and 10x (ocular). Based on petrographic observation, the rock unit is composed of feldspar (40%), plagioclase (25%), biotite (15%), quartz (10%), and volcanic glass (10%) minerals (Plate 2).

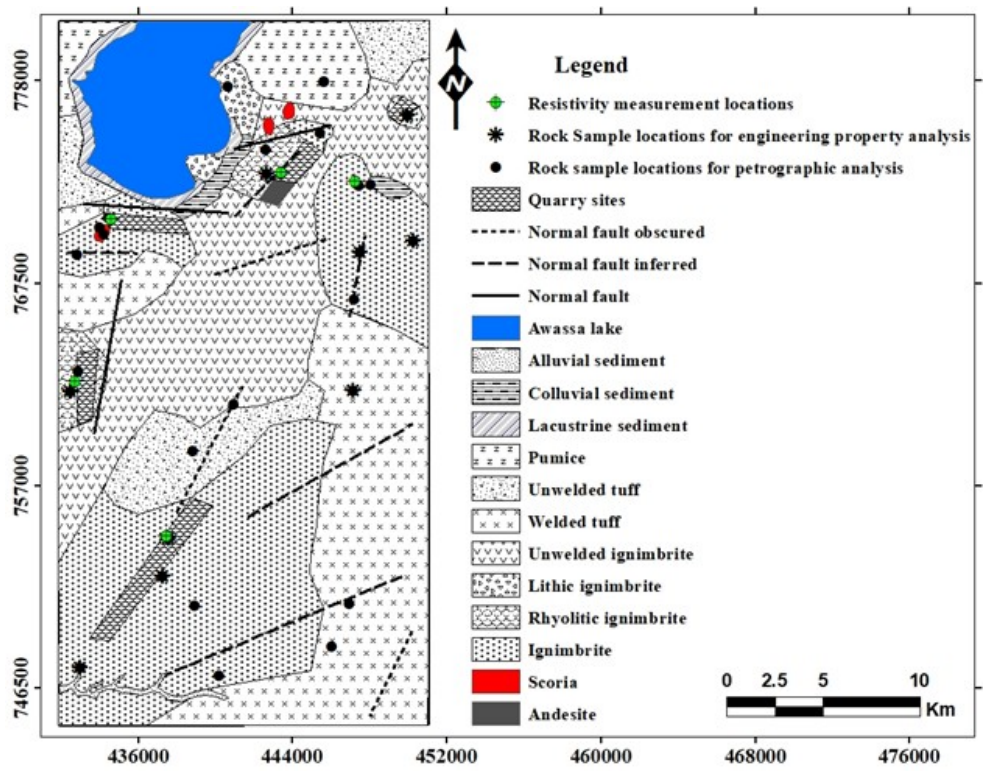

Figure 4: Geological and structural map showing sample and resistivity measurement locations of the study area.

Figure 5: Field photograph showing the andesite unit exposed in the study area.

Ignimbrite Unit

Ignimbrite lithology is mapped along southwestern and northeastern parts of the study area and is mainly exposed in quarry sites and along gentle mountain cliffs (Fig. 4). The ignimbrite hand specimen description is light gray and characterized by fiamme with eutaxitic texture. Microscopically, thin-section observation shows sanidine (40%), feldspar (35%), quartz (15%), and plagioclase (10%) minerals (Plate 3).

Lithic Ignimbrite Unit

Lithic fragments occur within unwelded ignimbrites and originate from wall-rocks that were incorporated during eruption. Crystal fragments are common in the main pyroclastic-flow body, where elutriation removes fine vitric ash and concentrates the denser crystals relative to glass shards.

Unwelded Ignimbrite Unit

This unit is mapped in the west and central parts and extended in the southwestern to northeastern sections within the study area. The unwelded ignimbrite out crop and hand specimen description is light to gray and fine-grained in texture. Microscopically thin section observation shows the rock unit is composed of sanidine (60%), pyroxene (25%), opaque (5%), and plagioclase (20%) minerals. Except for the opaque minerals, the rest of the minerals have developed flow texture.

Welded Tuff Unit

This unit is majorly exposed along the ragged terrain and sub-elevated along the southeastern of the study area (Fig. 4). A microscopically thin section shows mineralogical composition in percentage as volcanic glass (95%) and opaque (5%) minerals.

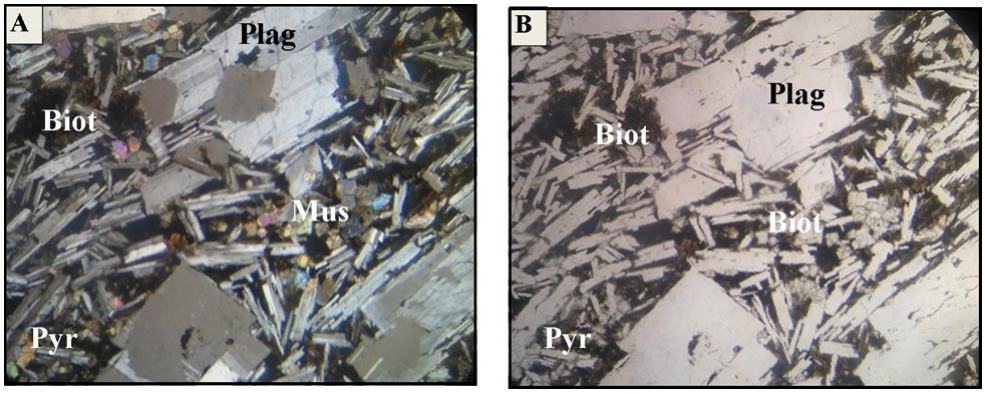

Plate .1: Microphotographs of andesite rock under XPL (A) and PPL (B) (NB. 40 time's magnification). (Abbreviations: Pyr= pyroxene, plag= plagioclase, Biot= biotite, Mus= muscovite).

Figure 6: Field photographs of rhyolitic ignimbrite unit observed during sample collections.

The rock unit is associated with fragment rock.

Pumice Unit

This unit crops out along the northern margin of the study area (Fig. 4). It covers some parts within the Hawassa Caldera. The color of the rock is light, vesiculated, fine-grained texture. Mineralogically, they are composed of volcanic glass (90%), quartz (7%), and opaque (3%) minerals (Plate 4).

Obsidian Unit

Obsidian is formed because of very rapid cooling of lava and characterized by a glassy texture. The rock unit is exposed in the central part, specifically associated with rhyolitic ignimbrite rock at the back of Alamora Ridge in the study area. Obsidian is black, dark, and green in color.

Colluvial and Lacustrine Sediment

Colluvial sediments occur locally along steep slopes and fault scarps, consisting of weathered ignimbrite and pyroclastic rock blocks accumulated at the lowlands near landslides and rockfalls. Their observed thickness is about 5 m. Lacustrine sediments occur around the swamps of Lake Hawassa and within endorheic graben depressions. They consist of unconsolidated mud, silt, sand, gravel, and conglomerate.

Alluvial Sediments

Alluvial sediments are found in the southern part of the study area within recent alluvial fans, formed where eroded material is deposited at abrupt gradient changes. These fans occur at valley mouths where streams flow into valleys and consist of re-deposited soil and fine- to medium-grained sands rich in weathered volcanic and volcaniclastic rocks, commonly containing angular pumice clasts.

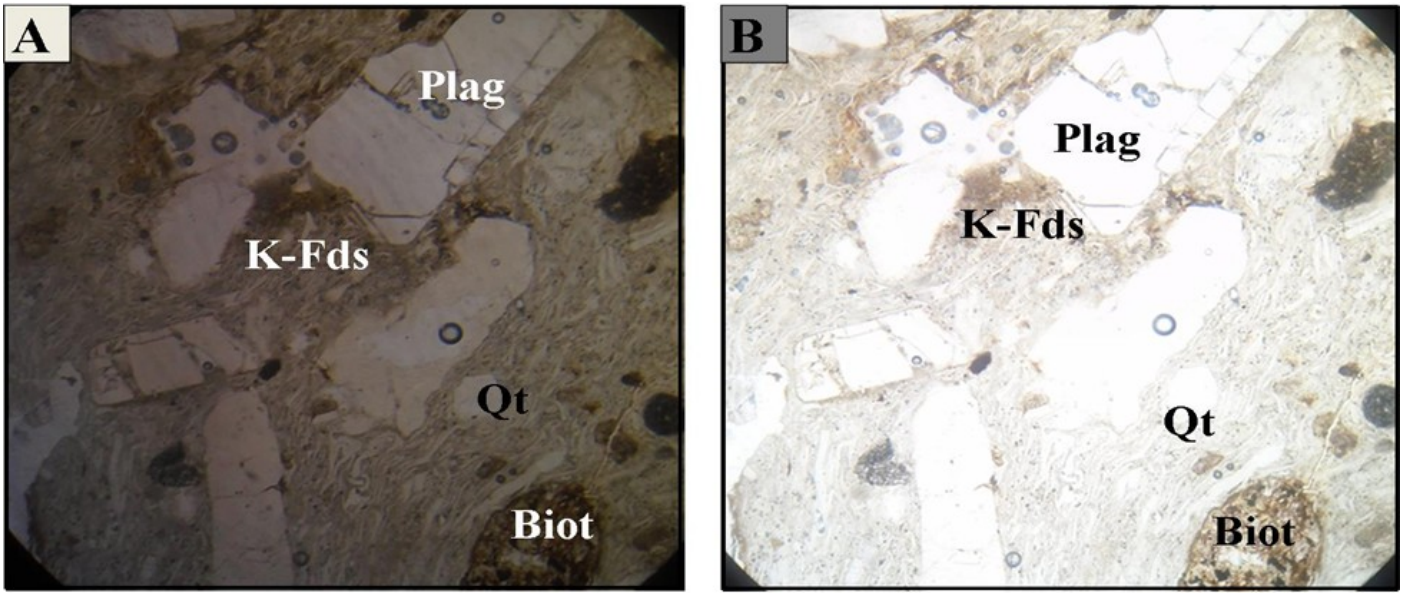

Plate .2: Microphotographs of rhyolitic ignimbrite rock under XPL (A) and PPL (B) (NB. 40 time's magnification). (Abbreviations: plag= plagioclase, Qt = quartz, K-Fds= k-feldspar and Biot= biotite).

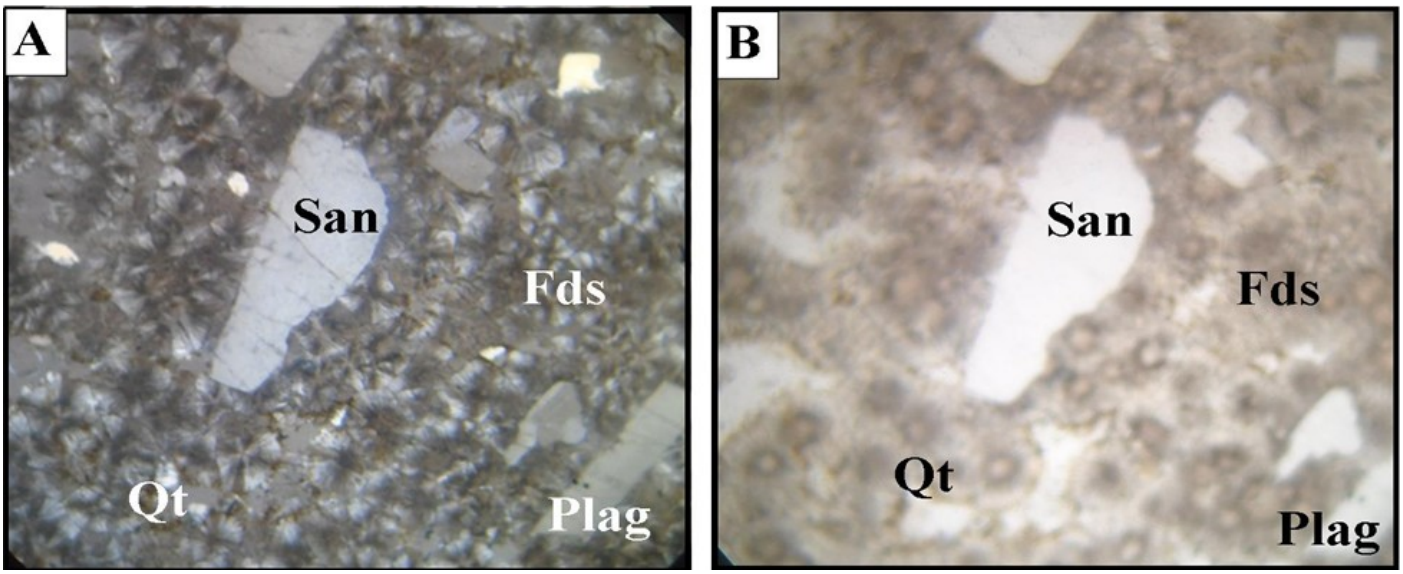

Plate .3: Microphotographs of ignimbrite rock under XPL (A) and PPL (B) (NB. 40 time's magnification). (Abbreviations: San = sanadine, Fds= feldspar, Qt = quartz and Plag= plagioclase).

4.2 Structural Geology

Mainly the structures of the study area are orientated in NE–SW directions which implies controlled by main Ethiopian rift. The dominant structures of the study are included: calderas, joints, cracks, and faults. Awassa caldera is a semicircular shape and forming a topographic depression of 35 × 20 km that results from magma erupting from a shallow magma reservoir. This leads to a loss of structural support for the overlying rock, collapse of the ground and formation of a caldera depression. Different faulting orientations are formed during caldera collapse (WoldeGabriel et al., 1990). The caldera is mainly characterised with silicic lava flows, pumices, welded and unwelded tuffs. Joints and cracks are dominant in the trachytic unit, whereas faults are common in the ignimbrite unit. A set of N-S trending vertical to sub-vertical joints and cracks were formed on the welded tuff (Fig. 7).

4.3 Electrical Resistivity Test and Analysis

Crack Area Vertical Electrical Sounding 1 (VES 1)

The apparent resistivity model curve for VES1 reveals a three-layers subsurface structure with resistivity varying between 78.33 Ωm and 1091 Ωm (Table 2). The topsoil was 2.9 m thick and had a resistivity range 78.33 to 572.3 Ωm, whereas, the second layer had a thickness of 19 m with a resistivity of 524.5 Ωm. The resistivity of the third layer is 1091 Ωm. Deductions made from the results suggest loose topsoil material at the top, possibly continuing to the depth of 21.92 m as volcanic ash.

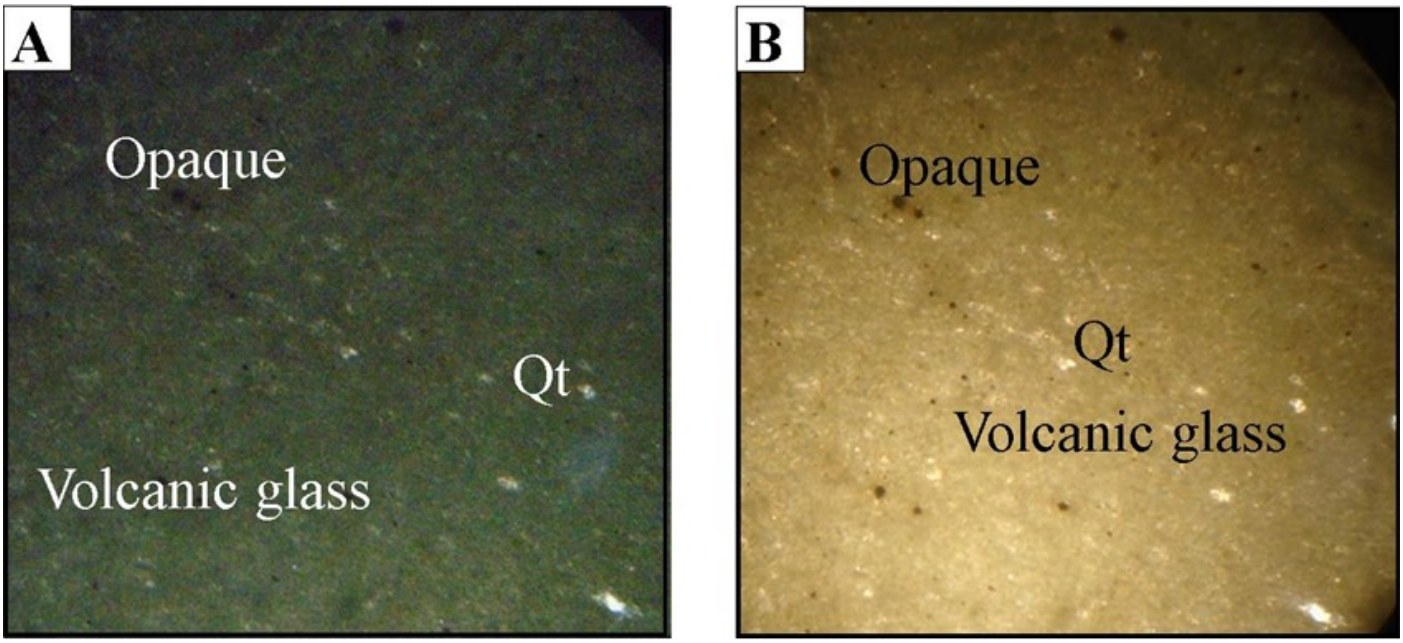

Plate .4: Microphotographs of pumice Under XPL (A) and PPL (B) (NB. 40 time's magnification). (Abbreviations: Qt = quartz).

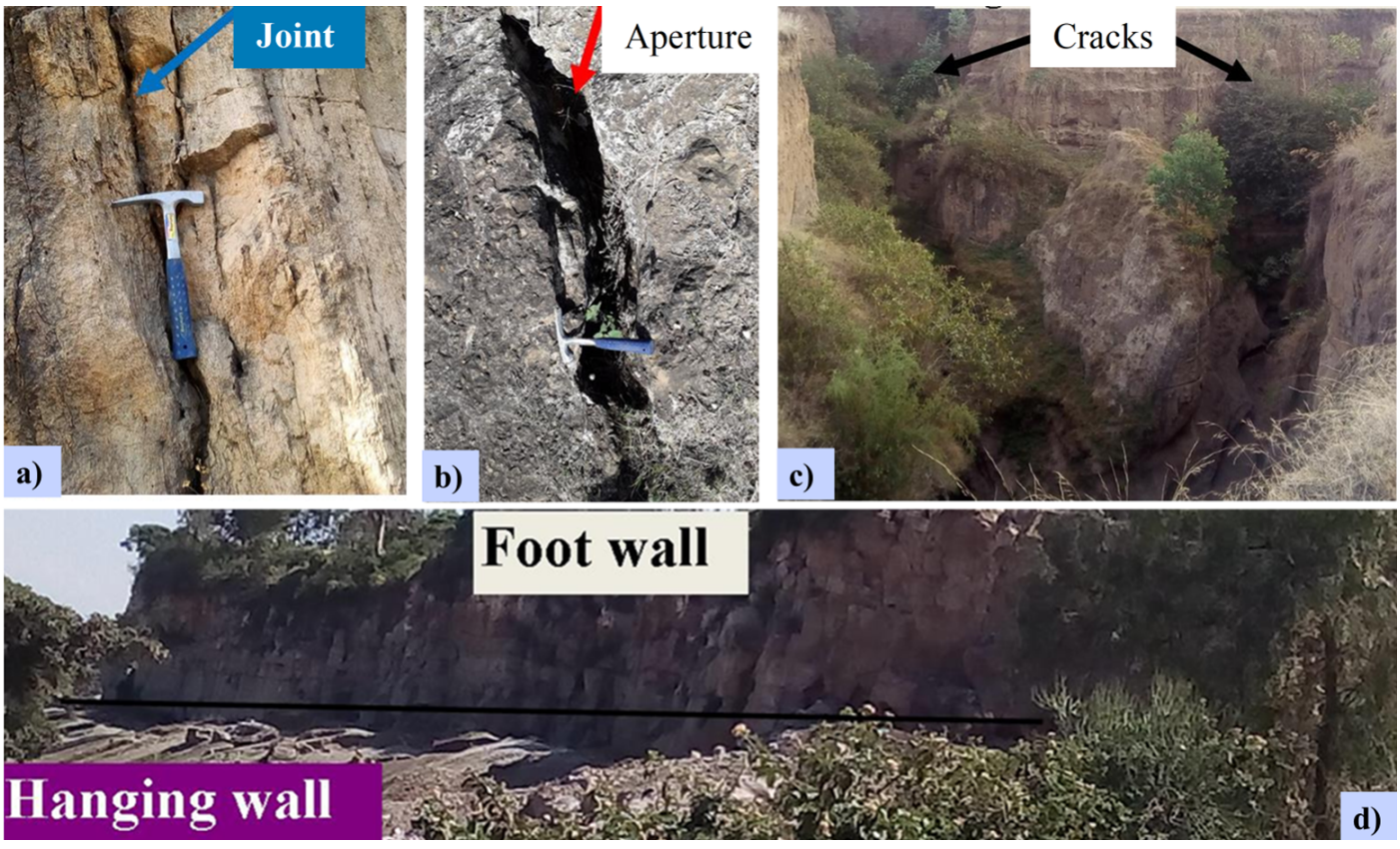

Figure 7: a) N-S trending joints, b) Apertures fracture, c) Big cracks and d) Norma fault within the ignimbrite rocks near the central part of the study area.

The third layer shows increasing resistivity suggest volcanic rock. The model curve and subsurface layers derived from VES 1 conducted around the crack area are shown (Fig. 8).

Table 2: Model layer resistivity and thickness of VES-1

Layer	Resistivity ohm-m	Thickness (m)	Depth (m) From	Depth (m) To	Possible Interpretations	Remarks
1	572.3 78.33	0.48 2.42	0 0.48	0.48 2.9	Top soil	Loose material
2	524.5	19	2.9	21.92	Volcanic ash	Semi-Consolidated
3	1091	-	21.92	>21.92	Volcanic rock	Massive

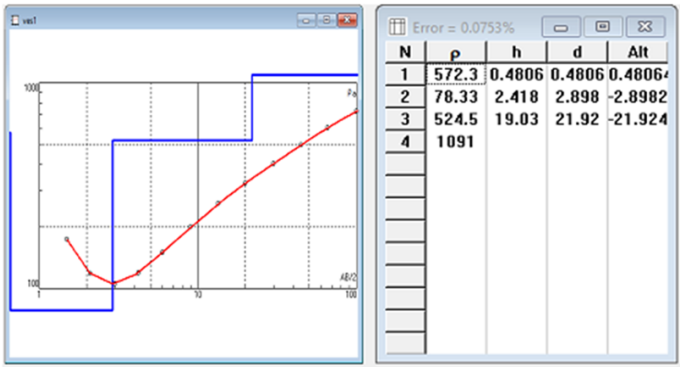

Figure 8: Vertical Electrical Sounding 1 (VES 1) model curve and layers near the crack area.

Boricha Ridge Locality Vertical Electrical Sounding 2 (VES 2)

The geological section at VES 2 suggests that the subsurface is made up of three layers with apparent resistivity values ranging between 64.7 Ωm and 3108 Ωm (Table 3). The upper layer, which has an apparent resistivity of 64.7 Ωm, is 1.13 m thick, is followed beneath it by a second layer of resistivity, 3108 Ωm, and thickness of 14.3 m. The third layer, which is the deepest layer, has an apparent resistivity of 1748 Ωm. It is inferred from these results that the top layer is loose soil and is underlain by a massive ignimbrite layer. Decreasing the apparent resistivity in the third layer indicates that the rock could be weathered or have fractures with water. The model curve and subsurface layers derived at VES 2 carried on the Boricha ignimbrite quarry site (Fig. 9).

Table 3: Model layer resistivity and thickness of VES-2

Layer	Resistivity ohm-m	Thickness (m)	Depth (m) From	Depth (m) To	Possible Interpretations	Remarks
1	64.7	1.13	0	1.13	Top soil	Loose
2	3108	14.3	1.13	15.5	Ignimbrite	Massive
3	1748	—-	15.5	>15.5	Slightly weathered Ignimbrite	Weathered

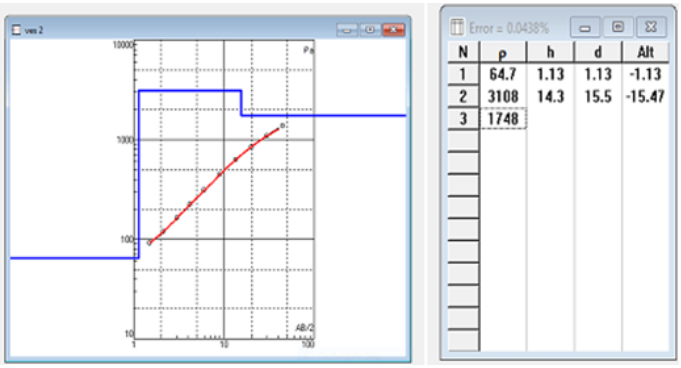

Figure 9: Vertical Electrical Sounding 2 (VES 2) model curve and interpreted subsurface layers at the Boricha ignimbrite quarry site.

Tariku Kaba Spot (Dale Woreda) Vertical Electrical Sounding 3 (VES 3)

From the VES 3 curve of the station, the subsurface consists of two layers. The apparent resistivity values range from 7.61 Ωm to 361 Ωm (Table 4). The thickness and apparent resistivity of the first layer is 2.17 m and 7.61 Ωm. The second layer has a resistivity of 361 Ωm (Fig. 10). It is apparent that the top layer might be loose silty clay soil with moisture content. The resistivity of the second layer suggests a massive formation.

Table 4: Model layer resistivity and thickness of VES-3

Layer	Resistivity ohm-m	Thickness (m)	Depth (m) From	Depth (m) To	Possible Interpretations	Remarks
1	7.61	2.17	0	2.17	Silty CLAY soil	Loose & moist
2	361	—	2.17	>2.17	Ignimbrite	Massive

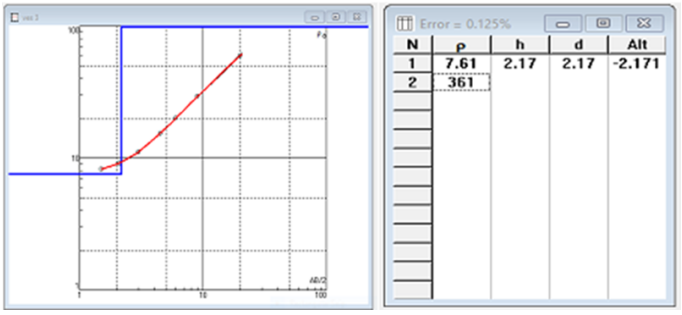

Figure 10: Vertical Electrical Sounding 3 (VES 3) model curve and interpreted subsurface layers at the Tariku Kaba site (Dale Woreda).

Gemto Gala Locality Vertical Electrical Sounding 4 (VES 4)

The subsurface structure at station VES4 is made up of 2 layers of apparent resistivities ranging between 277 Ωm and 15040 Ωm (Table 5). The results reveal that the topsoil has an apparent resistivity of 277 Ωm and is 0.48 m thick. The second layer has an apparent resistivity of 15040 Ωm. The analysis of these results reveals a fairly weathered upper layer and a massive basalt second layer. The model curve and subsurface layers derived at VES 4 measured at the Gemto Gala locality (Fig. 11).

Table 5: Model layer resistivity and thickness of VES-4

Layer	Resistivity ohm-m	Thickness (m)	Depth (m) From	Depth (m) To	Possible Interpretations	Remarks
1	277	0.48	0	0.48	Top soil	Loose
2	15040	—	0.48	>0.48	Very strong Tracy-basalt	Very Massive

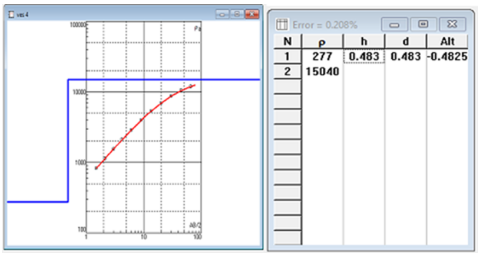

Figure 11: Vertical Electrical Sounding 4 (VES 4) model curve and interpreted subsurface layers at the Gemto Gala locality.

Filwha Area Vertical Electrical Sounding 5 (VES 5)

From the vertical electrical sounding curve of station VES 5, the subsurface consists of three layers. The apparent resistivity values range from 122 Ωm to 922 Ωm (Table 6). The thickness and apparent resistivity of the first layer are 0.9 m and 304 Ωm. The second layer is 3.02 m thick and has a resistivity of 122 Ωm. The third layer, however, has the apparent resistivity of 922 Ωm. It is apparent that the top layer might be loose topsoil and is underlain by a weathered second layer. The resistivity of the deepest layer suggests a massive formation. The model curve and subsurface layers derived near the Zelalem Filwha locality (Fig. 12).

Table 6: Model layer resistivity and thickness of VES-5

Layer	Resistivity ohm-m	Thickness (m)	Depth (m) From	Depth (m) To	Possible Interpretations	Remarks
1	304	0.9	0	0.9	Top soil	Loose
2	122	3.02	0.9	3.92	Volcanic rock	Weathered
3	922	—	3.92	>3.92	Volcanic rock	Massive

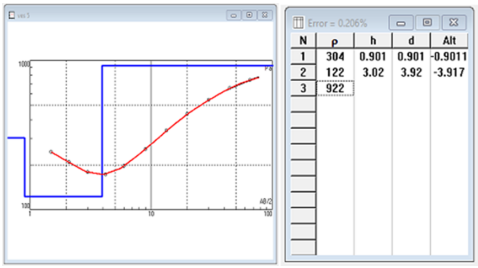

Figure 12: Vertical Electrical Sounding 5 (VES 5) model curve and interpreted subsurface layers near the Zelalem Filwha locality.

4.4 Rock Engineering Properties Analysis Techniques

The collected fresh representative rock was subjected to laboratory analysis, which includes bulk density, porosity, water absorption and compressive strength tests. The physical tests were conducted in the central laboratory of the Geological Institute of Ethiopia at Addis Ababa, which has a good reputation for such tests. The lists of selected tests and results from the Geological Institute of Ethiopia are given in Table 7 separately.

5 Discussion

The field and laboratory work carried out during the research activities were compiled and compared together to reveal the engineering performance of the rock mass in terms of construction material suitability. The exposed lithology shows a variety of textural and mineralogical characteristics, which affect their physical, chemical and construction material properties. From the interpretation of VES 1 (near the crack area): The third layer may be a good potential zone for infrastructures purposes which characterized by the resistivity value of 1091 Ωm. This resistivity value indicates that there is less dense volcanic rock, possibly ignimbrite with saturated pore water. At VES 2 (Boricha quarry site): The second layer could be a promising zone characterized by a high resistivity value of 3108 Ωm. This high value suggests massive ignimbrite without saturation and promising for constructions. At VES 3 (Tariku Kaba quarry site): After topsoil, the resistivity value for the second layer increased to 361 Ωm. This low value suggests that the layer is fractured unevenly, though it could be a good potential zone with low quality. At VES 4 (Gemto Gala Kebele): Unlike other rocks, this site shows the very highest resistivity value of 15040 Ωm for the second layer. This highest value shows that the layer is highly massive basalt without weathering and fractures, hence a potential zone for infrastructures. In contrast, at VES 5 (near Zelalem Filwha area or hot spring site): the resistivity value of 922 Ωm for the third layer suggests that the layer could be massive volcanic rock but possibly weathered and slightly fractured. Out of the five resistivity survey sites, VES 2 and VES 4 highly promising zones for future potential zone of quarry sites.

The physical properties, particularly water absorption, density, compressive strength and porosity have been found to be useful properties in assessing the rock material quality. Water absorption is important indicator of weathering resistance. Water absorption and bulk density vary from 0.80 to 29.13% and from 1.45 to 2.56 gm/m^3, respectively. The lowest water absorber among the rock samples is ALRS 2, while the highest one is the WRS3 sample. The porosity value is low in ALRS2 and highest in the WRS3 sample. The lowest water absorption and lowest porosity were observed in the ALRS 2, but bulk density is high. The highest water absorption and highest porosity were observed in the WRS 3 sample, which shows the linear relationship. The moderate values are found in the BRS1, ERS5, and YRS4 samples (Fig. 13 a). The strength of a rock's construction materials is of crucial importance in the

Table 7: Summarized rock engineering results of the study area.

Sample ID	Water Absorption (%)	Porosity (%)	Bulk-Density (gm/cm^3)	Compressive Strength (N/mm^2)
BRS 1	3.63	8.67	2.38	197.8
ERS 5	8.62	18.16	2.11	143.7
GRS 1	15.13	26.61	1.75	77.2
ERS 6	2.29	5.75	2.50	8
CHRS 2	19.84	32.26	1.62	45.5
IRS 3	21.17	34.98	1.65	35.0
ALRS 2	0.80	2.06	2.56	300.5
WRS 3	29.13	42.44	1.45	21.0
YRS 4	10.76	20.36	1.88	94.6

construction industry and for engineering purposes. The lowest and highest compressive strengths were observed in the ERS 6 and ALRS2 samples, respectively, and the values range from 8 N/mm² to 300.5 N/mm². The moderate values of 143.7 and 197.8 N/mm² were found in the ERS5 and BRS1 samples, respectively (Fig. 13 b).

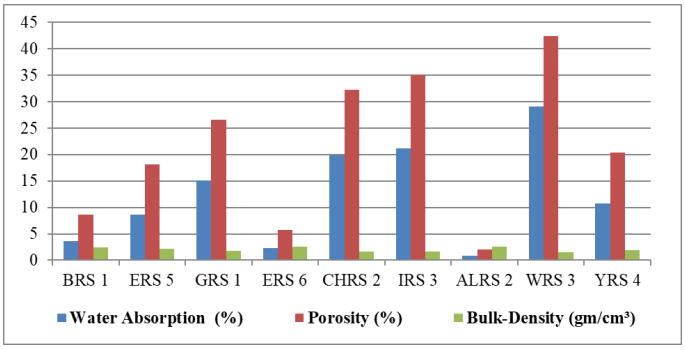

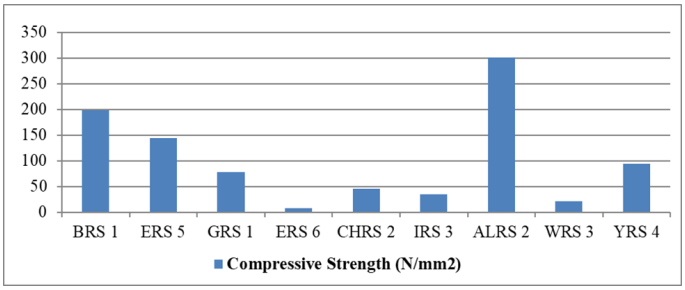

Figure 13: a) The physical properties of selected rock samples and b) The graph shows the lowest and highest compressive strength at selected rock samples.

6 Conclusions

Based on the field investigations and laboratory results acquired from the study locality, the following conclusions are drawn: -

- The lithologic formation of the study area specifically comprises of andesite, scoria, rhyolitic ignimbrite, ignimbrite, unwelded ignimbrite, lithic ignimbrite, welded tuff, unwelded tuff, pumice, colluvial sediment and lacustrine sediment.
- Andesite, rhyolitic ignimbrite and ignimbrite rocks within the study area are the most and a vital role in constructing the infrastructures structures which are destined to be strong, appealing and economical.
- Geologic setting of the study area belongs to central and southern parts of main Ethiopian rift (CMER). Therefore, the study locality lies on the main Ethiopian rift axes and highly affected by divergent forces.
- A combination of laboratory testing of samples, empirical analysis and field observations might be employed to determine the geology and requisite engineering properties.
- The laboratory test results from Alamora andisite rock (ALRS2), Boricha ignimbrite quarry site (BRS1) and Galoko Haro quarry site (near Leku Woreda) (ERS5) rock samples show good engineering properties in terms of strength values ranging from 143.7 to 300.5 N/mm², and relatively low water absorption and porosity suggests qualifying and suitable materials for structural load-bearing applications.
- The laboratory test results of rock samples from the Gane quarry site (GRS1, near Yirgalem), near Chuma town (CHRS2), Hanta area (IRS3), and Abela Wendo (YRS4) indicate relatively moderate compressive strength values ranging from 35 to 94.6 N/mm², accompanied by high porosity. The elevated porosity makes these rocks susceptible to weathering and degradation, particularly in environments with frequent water exposure. Due to their relatively high porosity, these rock materials are not recommended for use as humus stones or corridor pavements where moisture contact is common. However, they are suitable for cobblestone urban roads, box culverts and local buildings applications purposes.

Acknowledgment

The author expresses profound gratitude to Hawassa University for providing financial support to conduct this research study around Hawassa to Yirgalem locality, Sidama Regional State, Ethiopia.

The author indebted their deep thanks to Research and Technology Transfer, Research and Development Directorate offices for initiating the research and facilitating logistics, and to all who participated in the characterizing of construction material around Hawassa to Yirgalem and made a valuable intellectual contribution to the assessment process.

I would also like to thank Jeevanandam Mariappan (PhD) who was previously Hawassa University staff, Mr. Addis Haile (from Awassa mine and energy office expert), and residential people of the study area for their invaluable assistance during data collection, guidance's and reviewing. Several individuals have also contributed a lot to the successful completion of this research work, and thus, deserve acknowledgements for their contributions during data collection.

Conflicts of Interest

The authors declare that there are no conflicts of interest.

Funding

This particular study was funded by the College of Natural and Computational Sciences, Hawassa University.

References

Abebe, B., Acocella, V., Korme, T., & Ayalew, D. (2007). Quaternary faulting and volcanism in the main ethiopian rift. *Journal of African Earth Sciences*, *48*(2-3), 115–124. https://doi.org/10.1016/j.jafrearsci.2006.10.005

Ahmad, N. R., & Jamin, N. (2018). Preliminary view of geotechnical properties of soft rocks of semanggol formation at pokok sena, kedah. *IOP Conference Series: Earth and Environmental Science*, 012117.

Alshkane, Y. M. A. (2020). Deformability and shear strength parameters of the foundation of a project on tanjero formation in iraq using rmr and gsi. *Journal of Duhok University*, *23*(2), 523–534.

Butchibabu, B., Khan, P. K., & Jha, P. C. (2019). Foundation evaluation of underground metro rail station using geophysical and geotechnical investigations. *Engineering Geology*, *248*, 140–154. https://doi.org/10.1016/j.enggeo.2018.11.013

Corti, G. (2009). Continental rift evolution: From rifting to active breakup in the main ethiopian rift, east africa. *Earth-Science Reviews*, *96*(1–2), 1–53. https://doi.org/10.1016/j.earscirev.2009.05.003

Corti, G., Philippon, M., Sani, F., Keir, D., & Kidane, T. (2020). Space–time evolution of continental rifting: The east african rift system and the afar triangle. *Earth-Science Reviews*, *210*, 103414. https://doi.org/10.1016/j.earscirev.2020.103414

Goodman, R. E. (1992). *Engineering geology: Rock in engineering construction* (Second) [562p]. Wiley.

Hawassa Meteorological Agency. (2010). *Sources of the climatic parameters around hawassa* (tech. rep.). Hawassa Meteorological Agency.

Hutchison, W. (2015). *Past, present and future volcanic activity at restless calderas in the main ethiopian rift* [Doctoral dissertation, University of Oxford].

Japan International Cooperation Agency (JICA). (2012). *The study on groundwater resources assessment in the rift valley lakes basin in the federal democratic republic of ethiopia* (Final Report (Main Report)) (p. 721). Kokusai Kogyo Co., Ltd., Ministry of Water and Energy (MoWE).

Keir, D., Kendall, J.-M., Ebinger, C. J., & Stuart, G. W. (2006). Variations in lithospheric structure along the main ethiopian rift. *Geophysical Journal International*, *165*(1), 123–138. https://doi.org/10.1111/j.1365-246X.2006.02932.x

Muluneh, A. A., Biggs, J., Lewi, E., Kendall, J.-M., & Ayele, A. (2021). Seismicity and deformation at aluto volcano, main ethiopian rift: Evidence for an interplay between tectonics and magmatism. *Journal of Volcanology and Geothermal Research*, *410*, 107141. https://doi.org/10.1016/j.jvolgeores.2020.107141

Peccerillo, A., Barberio, M. R., Yirgu, G., Ayalew, D., Barbieri, M., & Wu, T. W. (2003). Relationships between mafic and peralkaline silicic magmatism in continental rift settings: A petrological, geochemical and isotopic study of the gedemsa volcano, central ethiopian rift. *Journal of Petrology*, *44*(11), 2003–2032. https://doi.org/10.1093/petrology/egg068

WoldeGabriel, G., Aronson, J. L., & Walter, R. (1990). Geology, geochronology, and rift basin development in the central sector of the main ethiopia rift. *Geological Society of America Bulletin*, *102*(4), 439–458. https://doi.org/10.1130/0016-7606(1990)102<0439:GGARBD>2.3.CO;2

Žáček, V., Rapprich, V., Aman, Y., Berhanu, B., Čížek, D., Dereje, K., Erban, V., Ezra, T., Firdawok, L., Habtamu, M., Hroch, T., Kopačková, V., Kycl, P., Málek, J., Mišurec, J., Orgoň, A., Pécskay, Z., Šíma, J., Tarekegu, D., & Verner, K. (2014). *Explanation booklet to the set of geoscience maps of ethiopia at scale 1:50,000, subsheet 0738-c4 hawasa*. Czech Geological Survey/Aquatest/Geological Survey of Ethiopia.

Žáček, V., Rapprich, V., Šíma, J., Škoda, R., Laufek, F., & Legesa, F. (2015). Kogarkoite, $Na_3(SO_4)F$, from the shalo hot spring, main ethiopian rift: Implications for f enrichment of thermal groundwater related to alkaline silicic volcanic rocks. *Journal of Geosciences*, *60*, 171–179. https://doi.org/10.3190/jgeosci.194

Zhang, Q. H., Li, Y. J., Yu, M. W., Hu, H. H., & Hu, J. H. (2015). Study of the rock foundation stability of the aizhai suspension bridge over a deep canyon area in china. *Engineering Geology*, *198*, 65–77. https://doi.org/10.1016/j.enggeo.2015.09.004

East African Journal of Biophysical and Computational Sciences
ISSN (Online): 2789-3618 and ISSN (Print): 2789-360X

Journal Information

Volume 6(2), 2025
DOI: https://dx.doi.org/10.4314/eajbcs.v6i2.5S

Homepage:
https://journals.hu.edu.et/hu-journals/index.php/eajbcs

Article History
Received: 02 June, 2025
Accepted: 02 December, 2025
Published Online: 25 December, 2025

How to cite

Gebrehana T.G. and Geleta H.L.(2025). Hilbert Space of Complex-Valued Harmonic Functions in the Unit Disc. *East African Journal of Biophysical and Computational Sciences* Volume 6(2), 2025, 51-56

Open Access

ARTICLE

Hilbert Space of Complex-Valued Harmonic Functions in the Unit Disc

Tseganesh Getachew Gebrehana[1], Hunduma Legesse Geleta[2,*]

[1,2] Department of Mathematics, Addis Ababa University, P.O.Box 1176, Addis Ababa, Ethiopia.

[*] Corresponding Author: hunduma.legesse@aau.edu.et

Abstract

The study investigated an extended version of Hilbert space of analytic functions called Hilbert space of complex-valued harmonic functions. It is found that functions in Hilbert space of complex-valued harmonic functions exhibit many properties analogous to its analytic counterpart such as complex-valued harmonic function analogous of norm, equivalent norms, reproducing kernels, growth estimates and Littlewood-Paley Identity Theorem. In particular, the researchers established that several fundamental results known for Hilbert space of analytic functions naturally extend to this broader harmonic framework. Beyond theoretical interest, these findings provide new tools for studying operator theory, potential theory, and approximation processes within the harmonic setting, thereby opening avenues for further research and applications in related areas of Mathematics and applied sciences.

Keywords: Complex-valued harmonic functions; Growth estimates; Hilbert space; Inner product; Integral means; Norm; Reproducing kernel.

East African Journal of Biophysical and Computational Sciences (EAJBCS) is already indexed on known databases like AJOL, DOAJ, CABI ABSTRACTS and FAO AGRIS.

1 Introduction

The study of complex-valued harmonic functions on the unit disk $\mathbb{D} = \{z \in \mathbb{C} | z| < 1\}$ has a long, tracing back to the seminal work of (Clunie & Sheil-Small, 1984) who first systematically introduced harmonic mappings of the form $f = h + \bar{g}$, where h and g are analytic in $\mathbb{D}$. Such functions naturally generalize analytic mappings, and they have been studied extensively in geometric function theory and operator theory; see, for example, (Dorff & Rolf, 2012; P. Duren, 2004) and the foundational references (Axler et al., 2001; Zhao, 1990).

The Hardy space $H^2(\mathbb{D})$ of analytic functions is a well-established Hilbert space whose power series coefficients belong to $l^2(\mathbb{Z}^+)$; its norm admits several equivalent formulations, and its element enjoys well-known growth and kernel estimates (see Cowen and MacCluer (1995), P. L. Duren (2001), Luery (2013), Romnes (2020), and Shapiro (1993)). Harmonic Hardy spaces $H_h^p(\mathbb{D})$ provide a natural extension where one admits functions of the form f=h+, where h and g are

analytic in $\mathbb{D}$. Many classical results for analytic Hardy spaces extend to these spaces (Shapiro, 1993; Zhao, 1990), but the Hilbert case $H_h^2(\mathbb{D})$ is of particular interest because of its inner product structure, reproducing kernel, and operator theoretic applications.

The purpose of this paper is to revisit $H_h^2(\mathbb{D})$, to establish its Hilbert space structure, and to develop self-contained proofs of several of its fundamental properties: equivalent norms, Littlewood-Paley identity, growth estimates, and reproducing kernels. While these results are classical in harmonic analysis, our aim is to highlight their analogues in the harmonic setting in parallel with the analytic case, and to present proofs that are accessible and unified as shown in the preprint (Gebrehana & Geleta, 2024) or https://arxiv.org/abs/2410.22045. The paper is organized as follows. Section 2 defines the space $H_h^2(\mathbb{D})$ and establishes its Hilbert space structure. Section 3 discusses equivalent norms and the Littlewood-Paley identity. Section 4 presents growth estimates and the explicit form of the reproducing kernel. We conclude with remarks on similarities and differences with the analytic case.

2 NORM ON $H_h^2(\mathbb{D})$

In this section, we define a norm on space of complex-valued harmonic functions whose coefficients in the Taylor series representation is square-summable and then show such space is a Hilbert space.

Theorem 2.1 Let f be a complex-valued harmonic function on the unit disc $\mathbb{D}$ given by

Let $f(z) = h(z) + \overline{g(z)}$, where $h(z) = \sum_{n=0}^{\infty} a_n z^n$ and $g(z) = \sum_{n=0}^{\infty} b_n z^n$ are analytic. Suppose

$$H_h^2(\mathbb{D}) = \Big\{ f : \mathbb{D} \to \mathbb{C} : f(z) = \sum_{n=0}^{\infty} a_n z^n + \overline{\sum_{n=0}^{\infty} b_n z^n} \text{ with } \sum_{n=0}^{\infty} \big(|a_n|^2 + |b_n|^2\big) < \infty \Big\}.$$

Then, $\|\cdot\|_{H_h^2(\mathbb{D})} : H_h^2(\mathbb{D}) \to \mathbb{R}$ defined by

$$\|f\|_{H_h^2(\mathbb{D})} = \Big(\sum_{n=0}^{\infty} \big(|a_n|^2 + |b_n|^2\big) \Big)^{1/2}$$

is a norm.

Proof:

(i) Since $\sum_{n=0}^{\infty} \big(|a_n|^2 + |b_n|^2\big) \geq 0$, we have $\|f\|_{H_h^2(\mathbb{D})}^2 \geq 0$, and

$$\sum_{n=0}^{\infty} \big(|a_n|^2 + |b_n|^2\big) = 0 \iff a_n = 0,\ b_n = 0 \iff f = 0.$$

Thus $\|f\|_{H_h^2(\mathbb{D})}^2 = 0$ if and only if $f = 0$.

(ii)

$$\begin{aligned} \|\alpha f\|_{H_h^2(\mathbb{D})}^2 &= \sum_{n=0}^{\infty} \big(|\alpha a_n|^2 + |\alpha b_n|^2\big) \\ &= |\alpha|^2 \sum_{n=0}^{\infty} \big(|a_n|^2 + |b_n|^2\big) \\ &= |\alpha|^2 \|f\|_{H_h^2(\mathbb{D})}^2. \end{aligned}$$

Thus $\|\alpha f\|_{H_h^2(\mathbb{D})} = |\alpha| \|f\|_{H_h^2(\mathbb{D})}$.

(iii) Suppose $f(z) = \sum_{n=0}^{\infty} a_n z^n + \overline{\sum_{n=0}^{\infty} b_n z^n}$ and $F(z) = \sum_{n=0}^{\infty} A_n z^n + \overline{\sum_{n=0}^{\infty} B_n z^n}$ are in $H_h^2(\mathbb{D})$. Then

$$\begin{aligned} \|f + F\|_{H_h^2(\mathbb{D})}^2 &= \sum_{n=0}^{\infty} \big(|a_n + A_n|^2 + |b_n + B_n|^2\big) \\ &= \sum_{n=0}^{\infty} \Big[|a_n|^2 + |A_n|^2 + 2\Re(a_n \bar{A}_n) \\ &\qquad + |b_n|^2 + |B_n|^2 + 2\Re(b_n \bar{B}_n) \Big]. \end{aligned}$$

So, by Cauchy-Schwartz inequality on the field of complex numbers, we have

$$\begin{aligned} \|f + F\|_{H_h^2(\mathbb{D})}^2 &\leq \sum_{n=0}^{\infty} \big(|a_n|^2 + |b_n|^2\big) + \sum_{n=0}^{\infty} \big(|A_n|^2 + |B_n|^2\big) \\ &\quad + 2\sqrt{\sum_{n=0}^{\infty} |a_n|^2 \sum_{n=0}^{\infty} |A_n|^2} + 2\sqrt{\sum_{n=0}^{\infty} |b_n|^2 \sum_{n=0}^{\infty} |B_n|^2} \\ &\leq \|f\|_{H_h^2(\mathbb{D})}^2 + \|F\|_{H_h^2(\mathbb{D})}^2 + 2\|f\|_{H_h^2(\mathbb{D})} \|F\|_{H_h^2(\mathbb{D})}. \end{aligned}$$

From which we obtain,

$$\|f + F\|_{H_h^2(\mathbb{D})} \leq \|f\|_{H_h^2(\mathbb{D})} + \|F\|_{H_h^2(\mathbb{D})}.$$

Therefore, from (i), (ii) and (iii), $\|\cdot\|_{H_h^2(\mathbb{D})}$ is a norm on $H_h^2(\mathbb{D})$. □

Remark: Any analytic and conjugate analytic functions are harmonic. Since $h(z) = \sum_{n=0}^{\infty} a_n z^n$ is analytic, $g(z) = \sum_{n=0}^{\infty} b_n z^n$ is analytic and $\overline{g(z)} = \overline{\sum_{n=0}^{\infty} b_n z^n}$ is conjugate analytic, we have

$$f(z) = h(z) + \overline{g(z)} = \sum_{n=0}^{\infty} a_n z^n + \overline{\sum_{n=0}^{\infty} b_n z^n}$$

is harmonic.

Theorem 2.2. Let $H_h^2(\mathbb{D})$ be the space of complex-valued harmonic functions on the unit disc of the form

$$f(z) = h(z) + \overline{g(z)} = \sum_{n=0}^{\infty} a_n z^n + \overline{\sum_{n=0}^{\infty} b_n z^n},$$

where h and g are analytic in $\mathbb{D}$ and

$$\sum_{n=0}^{\infty} \big(|a_n|^2 + |b_n|^2\big) < \infty.$$

Then $H_h^2(\mathbb{D})$ is a Hilbert space with respect to the inner product

$$\langle f, F\rangle = \sum_{n=0}^{\infty}\big(a_n\overline{A}_n + b_n\overline{B}_n\big),$$

where $f(z) = \sum_{n=0}^{\infty} a_n z^n + \overline{\sum_{n=0}^{\infty} b_n z^n}$, and $F(z) = \sum_{n=0}^{\infty} A_n z^n + \overline{\sum_{n=0}^{\infty} B_n z^n}$ are in $H_h^2(\mathbb{D})$.

Proof: We define a mapping

$$T : H_h^2(\mathbb{D}) \to \ell^2(\mathbb{Z}^+) \times \ell^2(\mathbb{Z}^+),$$

as $T(f) = (a_n, b_n)_{n\geq 0}$.

It is immediate that T is linear. Moreover,

$$\|T(f)\|^2_{\ell^2\times\ell^2} = \sum_{n=0}^{\infty}|a_n|^2 + \sum_{n=0}^{\infty}|b_n|^2 = \|f\|^2_{H_h^2(\mathbb{D})}.$$

So, T is an isometry. Since every pair of square-summable sequences $(a_n), (b_n)$ defines a function of the form

$$f(z) = \sum_{n=0}^{\infty} a_n z^n + \overline{\sum_{n=0}^{\infty} b_n z^n},$$

the map T is onto. Hence, T is a linear isometric isomorphism. Since $\ell^2(\mathbb{Z}^+) \times \ell^2(\mathbb{Z}^+)$ is a Hilbert space, its isometric image $H_h^2(\mathbb{D})$ is also a Hilbert space. □

3 EQUIVALENT NORMS

We now consider Complex-valued harmonic functions analogous of equivalent norm by integral means and Littlewood-Paley Identity Theorem which were studied in space of analytic functions.

Theorem 3.1 The norm defined on $H_h^2(\mathbb{D})$(in Theorem 2.1) has another equivalent representation by integral means which is denoted by $M_2^2(f, r)$and defined by

$$M_2^2(f, r) = \frac{1}{2\pi}\int_{-\pi}^{\pi}|f(re^{i\theta})|^2\, d\theta,$$

where $f(z) = h(z) + \overline{g(z)} = \sum_{n=0}^{\infty} a_n z^n + \overline{\sum_{n=0}^{\infty} b_n z^n}$ on $\mathbb{D}$ and $0 \leq r < 1$.

Proof: Using polar representation of $f = h + \overline{g}$, we get

$$f(re^{i\theta}) = \sum_{n=0}^{\infty} a_n r^n e^{in\theta} + \overline{\sum_{n=0}^{\infty} b_n r^n e^{in\theta}}.$$

After some algebraic manipulation, we obtain

$$\begin{aligned}|f(re^{i\theta})|^2 &= \sum_{n=0}^{\infty}\sum_{m=0}^{\infty} a_n\bar{a}_m r^{n+m}e^{i(n-m)\theta}\\ &+ \sum_{n=0}^{\infty}\sum_{m=0}^{\infty} a_m b_n r^{m+n}e^{i(n+m)\theta}\\ &+ \overline{\sum_{n=0}^{\infty}\sum_{m=0}^{\infty} a_m b_n r^{m+n}e^{i(n+m)\theta}}\\ &+ \sum_{n=0}^{\infty}\sum_{m=0}^{\infty} b_m\bar{b}_n r^{n+m}e^{i(n-m)\theta}.\end{aligned}$$

It is clear that the integral of exponential function $\{e^{i(n-m)\theta}\}_{n=0}^{\infty}$ is 2π when $n = m$ and 0 when $n \neq m$. Multiplying both sides by $\frac{1}{2\pi}$ and integrating with respect to θ from $-\pi$ to π, we get

$$\begin{aligned}&\frac{1}{2\pi}\int_{-\pi}^{\pi}|f(re^{i\theta})|^2\, d\theta\\ &= \sum_{n=0}^{\infty}|a_n|^2r^{2n} + \sum_{n=0}^{\infty}|b_n|^2r^{2n}\\ &\quad + \frac{1}{2\pi}\int_{-\pi}^{\pi}\sum_{n=0}^{\infty}\sum_{m=0}^{\infty} 2\Re(a_n b_m r^{n+m}e^{i(n+m)\theta})\, d\theta\\ &= \sum_{n=0}^{\infty}\big(|a_n|^2 + |b_n|^2\big)r^{2n}\\ &\quad + \sum_{n=0}^{\infty}\sum_{m=0}^{\infty}\frac{2r^{n+m}}{2\pi}\Re\Big(a_n b_m\int_{-\pi}^{\pi}e^{i(n+m)\theta}\, d\theta\Big)\\ &= \sum_{n=0}^{\infty}\big(|a_n|^2 + |b_n|^2\big)r^{2n}.\end{aligned}$$

Therefore,

$$M_2^2(f, r) = \frac{1}{2\pi}\int_{-\pi}^{\pi}|f(re^{i\theta})|^2\, d\theta = \sum_{n=0}^{\infty}\big(|a_n|^2 + |b_n|^2\big)r^{2n}.$$

To complete the proof, we need to show $\|f\|_{H_h^2(\mathbb{D})} = \lim_{r\to 1^-} M_2(f, r)$. From the above equation we have

$$M_2^2(f, r) = \sum_{n=0}^{\infty}\big(|a_n|^2+|b_n|^2\big)r^{2n} \leq \sum_{n=0}^{\infty}\big(|a_n|^2+|b_n|^2\big) = \|f\|^2_{H_h^2(\mathbb{D})}$$

whenever $f \in H_h^2(\mathbb{D})$ and $0 \leq r < 1$. So $M_2(f, r)$ is bounded by the $H_h^2(\mathbb{D})$-norm.

It remains to show that whenever $\lim_{r\to 1^-} M_2^2(f, r) = M < \infty$, then the partial sum of the series $M_2^2(f, r) = \sum_{n=0}^{\infty}\big(|a_n|^2 + |b_n|^2\big)r^{2n}$ are bounded on the unit disc by M^2:

$$\sum_{n=0}^{N}\big(|a_n|^2 + |b_n|^2\big)r^{2n} \leq \sum_{n=0}^{\infty}\big(|a_n|^2 + |b_n|^2\big)r^{2n} \leq M^2.$$

As $r \to 1^-$, this partial sum converges to functions in $H_h^2(\mathbb{D})$, which must therefore be bounded by M^2 as well. If every partial

sum of Taylor series representation of functions in $H_h^2(\mathbb{D})$ is bounded on the unit disc by M^2, then this is also true for the series. This completes the proof.

Corollary 3.2. The space of bounded complex-valued harmonic functions $f = h + \overline{g}$ on $H_h^\infty(\mathbb{D})$ is a subset of $H_h^2(\mathbb{D})$.

Proof: Let $f \in H_h^\infty(\mathbb{D})$. Then $\|f\|_{H_h^\infty(\mathbb{D})} = \sup_{z\in\mathbb{D}} |f(z)|$. Now,

$$\begin{aligned}\frac{1}{2\pi}\int_{-\pi}^{\pi} |f(re^{i\theta})|^2\, d\theta &\le \frac{1}{2\pi}\int_{-\pi}^{\pi} \left(\sup|f(re^{i\theta})|\right)^2 d\theta \\ &= \frac{1}{2\pi}\int_{-\pi}^{\pi} \|f\|^2_{H_h^\infty(\mathbb{D})}\, d\theta \\ &= \|f\|^2_{H_h^\infty(\mathbb{D})},\end{aligned}$$

which holds true for every $0 < r < 1$. So for any $f \in H_h^\infty(\mathbb{D})$ we get

$$\lim_{r\to 1^-} M_2^2(f, r) \le \|f\|^2_{H_h^\infty(\mathbb{D})}.$$

Hence, $f \in H_h^2(\mathbb{D})$. □

The following theorem is Littlewood-Paley identity theorem for space of complex-valued harmonic functions. It provides another expression for the $H_h^2(\mathbb{D})$-norm.

Theorem 3.3. For every complex-valued harmonic function $f = h + \overline{g} \in H_h^2(\mathbb{D})$ we have

$$\begin{aligned}\|f\|^2_{H_h^2(\mathbb{D})} &= |h(0) + \overline{g(0)}|^2 \\ &\quad + 2\int_{\mathbb{D}} |h'(z) + \overline{g'(z)}|^2 \log\frac{1}{|z|}\, dA(z),\end{aligned}$$

where dA denotes the normalized measure on $\mathbb{D}$; i.e., $dA = \frac{1}{\pi}\, dx\, dy = \frac{1}{\pi} r\, dr\, d\theta$.

Proof: We start by considering the right hand side of the equation in Theorem 3.3. Using the polar form of f, we obtain

$$\begin{aligned}&|(h+\overline{g})(0)|^2 + 2\int_{\mathbb{D}} |h'(z) + \overline{g'(z)}|^2 \log\frac{1}{|z|}\, dA \\ &= |h(0) + \overline{g(0)}|^2 \\ &\quad + 2\int_{-\pi}^{\pi} \frac{1}{\pi}\int_0^1 |(h' + \overline{g'})(re^{i\theta})|^2 \left(\log\frac{1}{r}\right) r\, dr\, d\theta.\end{aligned}$$

Interchanging the two integrals (which can be justified by Fubini's theorem), we have

$$\begin{aligned}&|h(0) + \overline{g(0)}|^2 + 2\int_{\mathbb{D}} |h'(z) + \overline{g'(z)}|^2 \log\frac{1}{|z|}\, dA \\ &= |h(0) + \overline{g(0)}|^2 \\ &\quad + 2\int_0^1 \left(\frac{1}{\pi}\int_{-\pi}^{\pi} |(h' + \overline{g'})(re^{i\theta})|^2\, d\theta\right)\left(\log\frac{1}{r}\right) r\, dr.\end{aligned}$$

Applying simple algebraic manipulations, we obtain

$$\begin{aligned}&|h(0) + \overline{g(0)}|^2 + 2\int_{\mathbb{D}} |h'(z) + \overline{g'(z)}|^2 \log\frac{1}{|z|}\, dA \\ &= |h(0) + \overline{g(0)}|^2 \\ &\quad + 4\int_0^1 M_2^2(h'(z) + \overline{g'(z)}, r)\left(\log\frac{1}{r}\right) r\, dr.\end{aligned}$$

Replacing by the Taylor series representation, we get

$$\begin{aligned}&|h(0) + \overline{g(0)}|^2 + 2\int_{\mathbb{D}} |h'(z) + \overline{g'(z)}|^2 \log\frac{1}{|z|}\, dA \\ &= |h(0) + \overline{g(0)}|^2 \\ &\quad + 4\int_0^1 \sum_{n=1}^{\infty} \left(n^2|a_n|^2 + n^2|b_n|^2\right) r^{2n-2}\left(\log\frac{1}{r}\right) r\, dr \\ &= |h(0) + \overline{g(0)}|^2 \\ &\quad + 4\sum_{n=1}^{\infty} n^2\left(|a_n|^2 + |b_n|^2\right)\int_0^1 r^{2(n-1)}\left(\log\frac{1}{r}\right) r\, dr \\ &= |h(0) + \overline{g(0)}|^2 \\ &\quad + 4\sum_{n=1}^{\infty} n^2\left(|a_n|^2 + |b_n|^2\right)\frac{1}{4n^2} \\ &= |h(0) + \overline{g(0)}|^2 + \sum_{n=1}^{\infty}\left(|a_n|^2 + |b_n|^2\right) \\ &= \|f\|^2_{H_h^2(\mathbb{D})}.\end{aligned}$$

From which we obtain,

$$|h(0) + \overline{g(0)}|^2 + 2\int_{\mathbb{D}} |h'(z) + \overline{g'(z)}|^2 \log\frac{1}{|z|}\, dA = \|f\|^2_{H_h^2(\mathbb{D})}.$$

This completes the proof.

4 GROWTH ESTIMATES AND KERNELS

The analogous growth estimates and reproducing kernels on space of complex-valued harmonic functions in the unit disc can be obtained as follows:-

Theorem 4.1 (Growth estimate). For each $z \in \mathbb{D}$, and $f = h + \overline{g} \in H_h^2(\mathbb{D})$ it holds that $|f(z)| \le \frac{2\|f\|_{H_h^2(\mathbb{D})}}{\sqrt{1-|z|^2}}$.

Proof: By applying the triangle inequality for the modulus and Cauchy-Schwarz inequality to the complex-valued harmonic function f, for each $z \in \mathbb{D}$, we obtain

$$\begin{aligned}|f(z)| &= \left|\sum_{n=0}^{\infty} a_n z^n + \overline{\sum_{n=0}^{\infty} b_n z^n}\right| \\ &\le \sum_{n=0}^{\infty} |a_n||z|^n + \sum_{n=0}^{\infty} |b_n||z|^n \\ &\le \left(\sum_{n=0}^{\infty} |a_n|^2\right)^{\frac{1}{2}}\left(\sum_{n=0}^{\infty} |z|^{2n}\right)^{\frac{1}{2}} \\ &\quad + \left(\sum_{n=0}^{\infty} |b_n|^2\right)^{\frac{1}{2}}\left(\sum_{n=0}^{\infty} |z|^{2n}\right)^{\frac{1}{2}} \\ &= \left[\left(\sum_{n=0}^{\infty} |a_n|^2\right)^{\frac{1}{2}} + \left(\sum_{n=0}^{\infty} |b_n|^2\right)^{\frac{1}{2}}\right]\left(\sum_{n=0}^{\infty} |z|^{2n}\right)^{\frac{1}{2}} \\ &\le \left(\|h\|_{H_h^2(\mathbb{D})} + \|g\|_{H_h^2(\mathbb{D})}\right)\left(\sum_{n=0}^{\infty} |z|^{2n}\right)^{\frac{1}{2}} \\ &= \frac{\|h\|_{H_h^2(\mathbb{D})} + \|g\|_{H_h^2(\mathbb{D})}}{\sqrt{1-|z|^2}}.\end{aligned}$$

But then, $\|h\|_{H_h^2(\mathbb{D})} \leq \|f\|_{H_h^2(\mathbb{D})}$ and $\|g\|_{H_h^2(\mathbb{D})} \leq \|f\|_{H_h^2(\mathbb{D})}$, which gives

$$|f(z)| \leq \frac{2\|f\|_{H_h^2(\mathbb{D})}}{\sqrt{1-|z|^2}}. \quad \square$$

Theorem 4.2 (Reproducing kernel). Suppose $\mathbb{D} = \{z \in \mathbb{C} : |z| < 1\}$ is the unit disc in the complex plane and $H_h^2(\mathbb{D})$ the Hilbert space of complex-valued harmonic functions

$$f(z) = \sum_{n=0}^{\infty} a_n z^n + \overline{\sum_{n=0}^{\infty} b_n z^n},$$

with

$$\|f\|^2_{H_h^2(\mathbb{D})} = \sum_{n=0}^{\infty} |a_n|^2 + \sum_{n=0}^{\infty} |b_n|^2.$$

Then for each $\alpha \in \mathbb{D}$ the evaluation function $f \longmapsto f(\alpha)$ is bounded and the reproducing kernel is given by

$$K_\alpha(z) = \frac{1}{1-\bar{\alpha}z} + \frac{1}{1-\alpha\bar{z}}, \quad (|\bar{\alpha}z| < 1),$$

satisfying

$$\langle f, K_\alpha \rangle = f(\alpha)$$

for all $f \in H_h^2(\mathbb{D})$; moreover this kernel is unique.

Proof: Define $e_n(z) = z^n$ and $h_n(z) = \bar{z}^n$ for $n \geq 0$. Recall that for

$$f(z) = \sum_{n=0}^{\infty} a_n z^n + \overline{\sum_{n=0}^{\infty} b_n z^n},$$
$$g(z) = \sum_{n=0}^{\infty} c_n z^n + \overline{\sum_{n=0}^{\infty} d_n z^n},$$

in $H_h^2(\mathbb{D})$ the inner product of f and g is given by,

$$\langle f, g \rangle = \sum_{n=0}^{\infty} a_n \bar{c}_n + \sum_{n=0}^{\infty} b_n \bar{d}_n.$$

This gives $\langle e_n, e_m \rangle = \delta_{nm}$, $\langle h_n, h_m \rangle = \delta_{nm}$ and $\langle e_n, h_m \rangle = 0$ where δ_{nm} represents the Kronecker delta. Thus, $\{e_n\}_{n\geq 0} \cup \{h_n\}_{n\geq 0}$ is an orthonormal basis of $H_h^2(\mathbb{D})$.

Now, by the standard reproducing kernel Hilbert space formula,

$$\begin{aligned} K_\alpha(z) &= \sum_{n=0}^{\infty} e_n(z)\overline{e_n(\alpha)} + \sum_{n=0}^{\infty} h_n(z)\overline{h_n(\alpha)} \\ &= \sum_{n=0}^{\infty} z^n \bar{\alpha}^n + \sum_{n=0}^{\infty} \bar{z}^n \overline{\bar{\alpha}^n} \\ &= \sum_{n=0}^{\infty} \bar{\alpha}^n z^n + \sum_{n=0}^{\infty} \alpha^n \bar{z}^n. \end{aligned}$$

Each series converges for $|\alpha z| < 1$, giving the closed form

$$K_\alpha(z) = \frac{1}{1-\bar{\alpha}z} + \frac{1}{1-\alpha\bar{z}}.$$

To show K_α is in $H_h^2(\mathbb{D})$, the coefficient sequences of K_α are $(\bar{\alpha}^n)_{n\geq 0}$ and $(\alpha^n)_{n\geq 0}$, so

$$\|K_\alpha\|^2_{H_h^2(\mathbb{D})} = \sum_{n=0}^{\infty} |\alpha|^{2n} + \sum_{n=0}^{\infty} |\alpha|^{2n} = \frac{2}{1-|\alpha|^2} < \infty.$$

Hence, K_α is in $H_h^2(\mathbb{D})$ and the evaluation is bounded.

For $f(z) = \sum_{n=0}^{\infty} a_n z^n + \overline{\sum_{n=0}^{\infty} b_n z^n} \in H_h^2(\mathbb{D})$ we have

$$\langle f, K_\alpha \rangle = \sum_{n=0}^{\infty} a_n \alpha^n + \sum_{n=0}^{\infty} b_n \bar{\alpha}^n = f(\alpha).$$

So, the reproducing kernel property holds.

Conversely, if for all $\alpha \in \mathbb{D}$ the evaluation $H_h^2(\mathbb{D}) \ni f \longmapsto f(\alpha)$ is a bounded linear functional on $H_h^2(\mathbb{D})$, then by Riesz Representation theorem, there exists a function L_α in $H_h^2(\mathbb{D})$ with the property,

$$f(\alpha) = \langle f, L_\alpha \rangle.$$

If another L_α reproduces evaluation, then $\langle f, K_\alpha - L_\alpha \rangle = 0$ for all $f \in H_h^2(\mathbb{D})$. Taking $f = K_\alpha - L_\alpha$ we get $\|K_\alpha - L_\alpha\|^2_{H_h^2(\mathbb{D})} = 0$. Hence $K_\alpha = L_\alpha$, which shows the kernel is unique.

5 Conclusion

In summary, we have developed a Hilbert space framework for complex-valued harmonic functions on the unit disc, analogous to the well-established analytic setting. An equivalent norm representation was derived in terms of integral means, providing a natural structure for further analysis. Within this framework, we established a harmonic analogue of the Littlewood–Paley Identity Theorem and derived comparable growth estimates for complex-valued harmonic functions, thereby extending classical results from analytic function theory to the harmonic setting.

Furthermore, we introduced the reproducing kernel associated with this Hilbert space, which plays a central role in functional analysis by enabling evaluation functionals and facilitating the study of bounded linear operators. This kernel provides a powerful tool for analyzing the geometry and operator theory of the space.

These results not only enrich the theory of harmonic function spaces but also open new avenues for research. Potential directions include the study of composition operators, multipliers, and dual spaces, as well as applications in potential theory and approximation theory. The harmonic framework developed here may also have implications in related fields such as signal processing and mathematical physics, where harmonic functions naturally arise.

Acknowledgements:

We would like to thank Addis Ababa University and Adama Science and Technology University, for providing us

opportunities. We sincerely thank the reviewers for their careful evaluation of our manuscript and their constructive comments.

Conflicts of Interest

The authors declare that there are no conflicts of interest regarding the publication of this paper.

Funding

No funding is received in conducting this research.

References

Axler, S., Bourdon, P., & Wade, R. (2001). *Harmonic function theory* (Vol. 137). Springer Science & Business Media.

Clunie, J., & Sheil-Small, T. (1984). Harmonic univalent functions. *Annales Fennici Mathematici*, *9*(1), 3–25.

Cowen, C. C., & MacCluer, B. D. (1995). *Composition operators on spaces of analytic functions* (Vol. 20). CRC Press.

Dorff, M., & Rolf, J. S. (2012). Anamorphosis, mapping problems, and harmonic univalent functions. In *Explorations in complex analysis* (pp. 197–269).

Duren, P. (2004). *Harmonic mappings in the plane* (Vol. 156). Cambridge University Press.

Duren, P. L. (2001). *Univalent functions* (Vol. 259). Springer Science & Business Media.

Gebrehana, T. G., & Geleta, H. L. (2024). Hilbert space of complex-valued harmonic functions in the unit disc. *arXiv preprint*. https://arxiv.org/abs/2410.22045

Luery, K. (2013). *Composition operators on hardy spaces of the disk and half-plane* [Doctoral dissertation, University of Florida].

Romnes, H. B. (2020). *Composition operators on the hardy space of dirichlet series* [Master's thesis, NTNU].

Shapiro, J. H. (1993). *Composition operators and classical function theory*. Springer-Verlag.

Zhao, C. (1990). *Harmonic bergman spaces* [Doctoral dissertation, Washington University].

East African Journal of Biophysical and Computational Sciences
ISSN (Online): 2789-3618 and ISSN (Print): 2789-360X

Journal Information

Volume 6(2), 2025
DOI: https://dx.doi.org/10.4314/eajbcs.v6i2.6S

Homepage:
https://journals.hu.edu.et/hu-journals/index.php/eajbcs

Article History
Received: 09 July, 2025
Accepted: 09 December, 2025
Published Online: 25 December, 2025

How to cite

Mathewos et al. (2025). Assessment of Microbial Contamination in Beef from Abattoir to Retail Meat Outlets in Shone Administrative Town, Hadiya Zone, Southern Ethiopia. *East African Journal of Biophysical and Computational Sciences* Volume 6(2), 2025, 57-70

ARTICLE

Assessment of Microbial Contamination in Beef from Abattoir to Retail Meat Outlets in Shone Administrative Town, Hadiya Zone, Southern Ethiopia

Merkin Mathewos[1], Beyene Dobo[1,*], Abraham Mikru[1]

[1]College of Natural and Computational Sciences, Department of Biology, P.O.Box: 05, Hawassa, Ethiopia.

*Corresponding author:beyeneashl@yahoo.co.uk

Abstract

This study investigated microbial contamination along the beef production chain in Shone Administrative Town, Hadiya Zone, Southern Ethiopia. It assessed the contamination pathways from abattoirs to butcher shops. A total of 9 carcass samples from the abattoir and 30 meat samples from 10 butcher shops were analyzed for aerobic mesophilic bacterial count (AMBC), total coliform count (TCC), fecal coliform count (FCC), Staphylococcus aureus, Salmonella, and Shigella. At the abattoir, Sample 2 exhibited the highest AMBC (6.56±0.02 log CFU/ml), while Sample 1 recorded the highest TCC, FCC, and Salmonella levels. Sample 3 had the greatest loads of S. aureus and Shigella. The lowest microbial loads varied across samples, with Sample 2 showing the lowest TCC, FCC, and S. aureus. Among butcher shops, Butchers 10 and 5 showed the highest AMBC and TCC values, respectively, whereas Butcher 9 recorded the highest FCC and S. aureuscounts. Salmonella and Shigella were most prevalent in samples from Butcher 2. In contrast, Butcher 2 had the lowest AMBC, and Butcher 6 recorded the lowest TCC, FCC, and S. aureuslevels. Notably, Salmonella and Shigella were absent in samples from Butcher 3. Observational assessments further revealed poor hygiene practices during meat processing, handling, and transportation, posing significant food safety risks. The detection of pathogenic organisms such as Salmonella, Shigella, FCC, and S. aureusindicates substantial potential for foodborne infections and intoxications. In conclusion, the study underscores the urgent need to strengthen hygienic practices throughout the beef supply chain to safeguard public health in the region.

Keywords: Abattoir; butcher; Beef; contamination; hygiene; intoxication

East African Journal of Biophysical and Computational Sciences (EAJBCS) is already indexed on known databases like AJOL, DOAJ, CABI ABSTRACTS and FAO AGRIS.

1 Introduction

Ethiopia is home to the largest livestock population in Africa. According to the 2021 Agricultural Sample Survey, there are around 70.3 million cattle, 42.9 million sheep, and 52.5 million goats (Legese et al., 2023). Livestock production is a vital part of the national economy, making up nearly 45% of agricultural GDP and about 18.7% of the total national GDP. In 2021, cattle production alone through meat, milk, hides, draft power, and other products brought in an estimated USD 8.52 billion (Li et al., 2023).

Beef is a crucial component of the Ethiopian diet, offering high-quality protein and essential micronutrients like vitamins A and B, which can be scarce in plant-based diets. The demand for meat is on the rise, fueled by population growth, increasing incomes, urbanization, and changing dietary habits. However, despite this growing appetite, significant food safety issues continue to challenge the meat production and marketing chain (Duguma & Janssens, 2020).

Various studies from different regions in Ethiopia have highlighted concerning levels of microbial contamination in raw beef. For example, a 2023 study in Assosa Town (Benishangul-Gumuz region) found high aerobic mesophilic bacterial counts (averaging 5.04 log10cfu/g) and elevated levels of *Staphylococcus aureus* (3.84 log10cfu/g) in slaughterhouses and butcher shops (Legese et al., 2023). In Hawassa, (Kenaw et al., 2024) reported high total plate counts, Enterobacteriaceae, and staphylococci on meat and contact surfaces, largely due to inadequate disinfection practices and the common exposure of meat to flies.

Similarly, a study conducted in three cities of the Tigray region found frequent contamination of raw cattle meat with zoonotic pathogens like Escherichia coli, *Salmonella* spp., *Staphylococcus aureus*, and Campylobacter spp., which pose serious public health risks (Reda et al., 2025). In a study carried out in the slaughterhouses of Bishoftu, researchers found that beef carcasses were contaminated with *Salmonella* and E. coli O157, highlighting serious issues with hygiene practices in these facilities (Gutema et al., 2021).

The findings also revealed that ongoing problems like poor sanitation, inadequate hygiene in both slaughterhouses and retail spaces, and lax enforcement of food safety regulations are compromising meat quality and public health in Ethiopia. This is particularly concerning in towns like Shone, where beef is sourced from both abattoirs and butcheries, making it crucial to evaluate the sanitary conditions throughout the meat production and distribution process.

2 Materials and Methods

2.1 Description of the Study Area

This study was carried out in Shone Administrative Town, located in the Hadiya Zone of Central Ethiopia (Figure 1). It is one of the eleven towns in the Hadiya Zone, part of the Central Ethiopian Regional state. Geographically, Shone is the farthest town from the zonal capital, Hosanna. It is found approximately 345 km south of Addis Ababa on the main road to Arba Minch, and97 km Southeast of Hosanna, and 17 km south of Durame.

Shone serves as the administrative center for both the town and the East Badawacho Woreda. It is situated at $7°8'21''$N latitude and $37°57'0''$E longitude, with an altitude of 1700 m above sea level. The town covers a total area of $35.32\,km^2$ and falls within the *woinadega* (mid-altitude) climatic zone. The local economy mainly depends on trade and related activities. According to the Central Statistical Agency (CSA) (2013), Shone has a population of 49,747, with 24,377 males and 25,370 females, and women make up about 51 % of the total.

Although there are slaughterhouses in the town that serve the locals, there are differences in the operational standards and degree of hygiene. Meat from sheep, goats, and cattle is frequently consumed by locals; consumption patterns are determined by both cultural and economic considerations. The community has uneven waste management procedures, and it frequently disposes of organic waste including animal byproducts inappropriately. The municipality generally has hygienic issues, which could affect the quality and safety of meat products.

2.2 Study Design

A cross-sectional study design was used, employing purposive sampling technique to collect meat samples. The samples were gathered from the Shone Administrative Town abattoir and ten retail meat outlets. Three replicate samples were collected from each location (abattoir and meat shops) to ensure data reliability and consistency. Laboratory analyses were conducted on selected microorganisms. These included aerobic mesophilic bacterial counts (AMBC), total coliform counts (TCC), faecal coliforms (FCC), *Staphylococcus aureus*, *Salmonella*, and *Shigella*.

To assess hygiene and sanitation practices, structured questionnaires were administered in English, Amharic, and Hadiyyisa. These were complemented by direct observations of the hygienic conditions and practices among workers in both abattoirs and meat shops. The questionnaires evaluated the knowledge and awareness of meat handlers regarding contamination risks along the beef production chain from the abattoir to retail outlets.

2.3 Sample Size Determination for Questionnaires Administration

During this study, respondents were selected from all retail meat outlets and abattoir workers of Shone administrative town for participating in the study following systematic random sampling technique by using the following simple formulae (Yamane, 1967).

$$n = \frac{N}{1 + N(e)^2} \tag{1}$$

Where n= is the sample size N= is the population size and e =is the level of precision. Using the above formulae, out of 43 workers of meat shops and abattoir of the study town (Godoliyas=4, Abaroso=3, Firehiwot=3, Meskel=4, Abenezer=2, Mini=4, Lichcha=3, Luci=3, Arenchbaxo =3, Fkadusiga bet=4

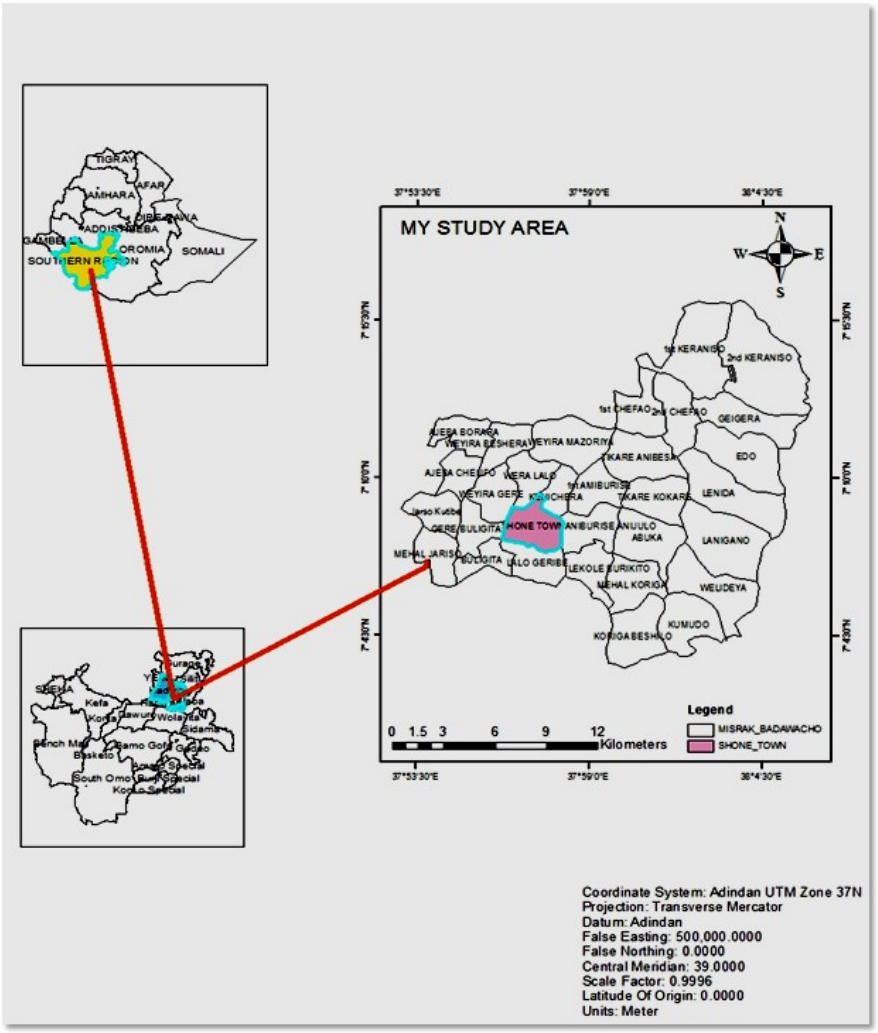

Figure 1: Location map of Shone administrative town (Source: Ethio. GIS)

and abattoir=10),38 respondents were selected. Therefore, N=43 and p=.5

$$n = \frac{N}{1 + N(e)^2(2)}$$

$= \frac{43}{1+43(.05)^2} = 38$ are sample size To keep proportionality of population among each, Palercolmorin formulae was used as cited by William Jams (1977). That means

$$Ps = \frac{nx}{N} \quad (3)$$

Where ps=proportional allocation to size X=number of populations in each retail meat outlets and abattoir N =total sample size N=total number of populations in all retail meat outlets and abattoir According to the above formulae proportionality number for each meat shop were Godoliyas = 3.61≈3, Abaroso = 2.71≈3, Firehiwot =2.71≈3, Meskel =3.61≈3, Abenezer = 1.8≈2, Licha =2.71≈3, Lucy =2.71≈3, Arenich baxo =2.71≈3, Fikadusiga bet=3.61≈3,Mini=3.61≈3 and abattoir=9.04≈9.Totally, 38 respondents, 9 from abattoir and 29 from butchers, were selected for interviews.

2.4 Data Collection Instruments

To support this study, data were gathered using structured questionnaires, direct field observations guided by prepared checklists, and meat sampling from the abattoir and retail meat outlets in Shone Administrative Town, Hadiya Zone, Central Ethiopia Regional State.

2.4.1 Observation and Checklist

Direct visual inspections were conducted to identify possible sources of microbial contamination during beef processing and to assess hygiene practices in the abattoir and butcher shops. The observations were accompanied by a checklist covering critical elements for good hygienic handling. The checklist focused on the condition of animals before slaughter (supported by veterinary specialist), the state of slaughterhouse facilities, processing procedures, hygiene of personnel and equipment, and meat transportation methods.

2.4.2 Questionnaire Administration

Questionnaires were used to collect data on from where the cattle are bought, meat distribution practices, methods of transportation, and availability of meat storage facilities. They also addressed the frequency of worker health checks, overall hygienic standards of the abattoir and meat outlets, and access to clean and safe water. The questionnaires were available in English, Amharic, and Hadiyyisa to ensure clarity and accessibility.

2.4.3 Media Preparation

All microbiological media used in this study were prepared according to the manufacturer's guidelines to maintain consistency and accuracy in laboratory testing.

2.4.4 Meat Sample Collection for Laboratory Analysis

For microbial examination, raw meat samples were aseptically collected by purposive sampling technique both from beef carcasses at the abattoir and from hanging displays in ten retail butcher shops. From 39 samples, 13samples in one round (10 from retail outlets and 3 from butcheries), each sample weighing 25 grams(according to ISO Standards: ISO 6887-2:2017), were placed in sterile containers with ice packs and immediately transported to the Veterinary Microbiology Laboratory at Hawassa University. All samples were processed within three hours of collection.

2.4.5 Preparation of Samples

Each meat sample was finely minced using a sanitized cutting blade, for each sample to prevent cross-contamination. A 10-gram portion from each sample was aseptically weighed using an analytical balance and mixed with 90 mL of sterile normal saline solution. The mixture was homogenized in a sterile beaker using a vortex mixer for two minutes. For serial dilution, seven sterile test tubes were used each filled with 9 mL of saline. One milliliter of the homogenized sample was added to the first tube and mixed thoroughly. Then, 1 mL from the first tube was transferred to the second, and this process was repeated through the seventh tube to achieve a seven-fold serial dilution (from 10^{1} to 10^{1}). One milliliter was discarded from the final dilution to ensure equal volume across tubes (Beijerinck, 1889).

2.4.6 Bacteriological Isolation and Identification

Distinct colonies that appeared on nutrient agar were examined for cultural characteristics such as shape, size, color, and texture. Gram staining and a series of standard biochemical tests were performed, following established procedures (Oyeleke & Manga, 2008). Isolates were identified based on their morphological and biochemical features including catalase, oxidase, coagulase, citrate utilization, methyl red reaction, motility, glucose fermentation, and lactose fermentation tests and compared with standard reference organisms using Bergey's Manual of Determinative Bacteriology (Buchanan & Gibbons, 1974).

2.4.7 Bacteriological Isolation

For primary isolation, bacterial growth on solid media was observed, and representative colonies were selected based on differences in size, shape, and color. These colonies were then sub-cultured onto nutrient agar and labeled for further identification.

2.5 Media for Primary Isolation and Enumeration of Bacteria

2.5.1 Aerobic Mesophilic Bacterial Count (AMBC)

Aerobic mesophilic bacteria were enumerated using the pour plate method on Plate Count Agar (PCA). From appropriately diluted samples, 0.1 mL of suspension was transferred into sterile Petri dishes containing pre-poured PCA. The plates were gently swirled in both directions to mix the inoculum evenly with the agar, then allowed to solidify for 15 minutes. They were then inverted and incubated at 35°C for 48 hours. After incubation, plates with 30–300 colonies were selected and counted using a colony counter, and CFU/mL was calculated using the formula: Colonies/Volume plated in mL) x Dilution Factor. Results were recorded as AMBC (American Public Health Association (APHA), 2017).

2.6 Enumeration of *Staphylococcus aureus*

To enumerate *Staphylococcus aureus*, the pour plate method was applied using Mannitol salt agar (MSA).Before inoculation, the storability of the media was tested by incubation of the sterile media in an autoclave for 24 hrs at 370C.Then, from each appropriate dilution, 0.1 mL was inoculated into sterile Petri dishes containing MSA. After gently swirling the plates and allowing them to solidify for 15 minutes, they were incubated at 37°C for 24 hours. Yellow-colored colonies were counted as S. *aureus*using a colony counter and the CFU/mL is calculated as shown above. Representative colonies were further sub-cultured on nutrient agar for confirmatory biochemical tests.

2.7 Enumeration of Total and Fecal Coliforms

To determine total and fecal coliform counts, 0.1 mL of each sample dilution was transferred into sterile Petri dishes containing 20 mL of MacConkey agar which was tested for its sterility before inoculation. The plates were left to solidify at room temperature for 15 minutes. Inoculated plates were incubated at 37°C for total coliforms and at 44°C for fecal coliforms for 24 hours. After incubation, plates with 30–300 colonies were selected, and red colonies were counted using a colony counter and the CFU/mL was calculated using the formula: Colonies / Volume plated in mL) x Dilution Factor. Selected colonies were sub-cultured on nutrient agar for further biochemical identification (Bhandare et al., 2007).

2.8 Detection of *Salmonella* and *Shigella* Species

To detect *Salmonella* and *Shigella*, 0.1 mL of diluted sample was poured into Petri dishes containing 20 mL of *Salmonella-Shigella* Agar (SSA). After the medium solidified, plates were incubated at 37°C for 48 hours. Black-centered colonies were identified as *Salmonella*, while colorless colonies indicated *Shigella*. Colonies were counted using a colony counter, and representative samples were sub-cultured onto nutrient agar for confirmatory tests (Cappuccino & Welsh, 2017).

Biochemical Tests for Identification of Bacterial Genera in Beef All tests were performed using pure bacterial cultures to ensure accuracy. Following staining procedures, various biochemical assays were conducted to support identification. Specific tests were selected based on the suspected bacterial types:

2.8.1 Gram Staining

Gram staining was used to differentiate Gram-positive from Gram-negative bacteria. A discrete colony was mixed with a drop of water on a clean slide, heat-fixed, and air-dried. The slide was treated sequentially with crystal violet (1 minute), Gram's iodine (1 minute), decolorizer (15 seconds), and safranin (1 minute), with gentle rinsing between steps. After drying, the sample was examined under an oil immersion microscope. Blue or purple cells indicated Gram-positive bacteria, while pink cells indicated Gram-negative bacteria (Bartholomew & Mittwer, 1952).

2.8.2 Catalase Test

A loopful of a 24-hour bacterial culture was placed on a clean slide, and a drop of 3% hydrogen peroxide was added. Immediate bubbling indicated a positive catalase reaction (Chester, 1979).

2.8.3 Coagulase Test

Using a sterile loop, a colony was mixed with a drop of rabbit plasma on a glass slide. Formation of white clumps within one minute indicated a positive coagulase result (Sperber & Tatini, 1975).

2.8.4 Oxidase Test

A piece of filter paper was moistened with freshly prepared 1% tetramethyl-p-phenylenediaminedihydrochloride. The test colony was streaked onto the paper. No color change after 15 seconds indicated a negative oxidase result (MacFaddin, 2000).

2.8.5 Citrate Utilization Test

Simmons citrate agar slants were inoculated with the test isolate and incubated at 37°C for 24 hours. A blue color on the slant surface indicated citrate utilization and a positive result (Forbes et al., 2007).

2.8.6 Methyl Red (MR) Test

MR-VP broth was inoculated with the test organism and incubated at 35°C for 48 hours. After incubation, five drops of methyl red reagent were added. Development of a stable red color indicated a positive result due to acid production and lowered pH (Madigan et al., 2024).

2.8.7 Glucose Fermentation Test

Phenol red glucose broth was inoculated with the test isolate and incubated at 37°C for 24 hours. A color change from red to yellow indicated acid production and a positive glucose fermentation result (MacFaddin, 2000).

2.8.8 Lactose Fermentation Test

Phenol red lactose broth was similarly inoculated and incubated at 37°C for 24 hours. Yellow coloration indicated lactose fermentation; no change indicated a negative result (MacFaddin, 2000).

2.8.9 Motility Test

Using a sterile straight wire, the test organism was inoculated into the center of a semisolid agar tube. After 24 hours of incubation

at 37°C, diffused turbidity around the stab line indicated motility, while growth confined to the stab line indicated a non-motile organism (Mitchell & Kogure, 2006).

2.9 Data Quality Control and Laboratory Safety

To ensure the reliability and validity of the research, all laboratory procedures including sample collection, handling, and culturing were performed following standardized protocols. Universal biosafety measures were strictly observed in accordance with National Committee for Clinical Laboratory Standards(NCCLS) guidelines (2002), given the potential health risks associated with handling pathogenic bacteria. All inoculated culture materials including test tubes, Petri dishes, and slides were sterilized in an autoclave at 121°C for 15 minutes prior to disposal. To prevent data mix-up, all materials were clearly labeled with unique identification codes to maintain proper tracking throughout the study.

2.10 Statistical Analysis

Data were carefully recorded, organized, and analyzed using descriptive statistics. Bacterial counts were calculated to colony-forming units per milliliter (CFU/mL) and expressed as mean log10 values. To evaluate differences in meat quality across samples, one-way analysis of variance (ANOVA) was applied at a 5% significance level. All statistical analyses were conducted using SPSS software version 20.0.

3 Results

3.1 Evaluation of Microbial Loads in Abattoir

The results of aerobic mesophilic bacterial counts (AMBC) from carcass samples collected at the Shone abattoir are summarized in Table 1. The mean log10 CFU/mL values were 6.33 ± 0.13 for sample 1, 6.56 ± 0.02 for sample 2, and 6.50 ± 0.04 for sample 3, with the overall mean value of 6.46 ± 0.47 log10 CFU/mL. Among the samples, sample 2 showed the highest bacterial load, while sample 1 had the lowest. However, the statistical analysis revealed that there is no significant difference in AMBC levels among the three samples ($p = 0.261$), indicating similar levels of contamination.

For total coliform counts (TCC), the mean log10 CFU/mL values for samples 1, 2, and 3 were 6.45 ± 0.14, 4.10 ± 2.45, and 6.32 ± 0.07, respectively, with an overall mean of 5.62 ± 0.73. Sample 1 exhibited the highest TCC, while sample 2 recorded the lowest. Despite the apparent variation, the differences among samples were not statistically significant ($p = 0.473$), suggesting relatively uniform coliform presence across the abattoir carcasses.

Regarding faecal coliform counts (FCC), the mean values were 6.16 ± 0.14 for sample 1, 3.85 ± 2.34 for sample 2, and 6.03 ± 0.21 for sample 3, resulting in an overall mean of 5.34 ± 0.69 log10 CFU/mL. Sample 1 showed the highest level of faecal contamination, while sample 2 had the lowest. Nonetheless, these variations were not statistically significant ($p = 0.479$), indicating a comparable microbial load among the sampled carcasses.

The mean log10 CFU/mL count of *Staphylococcus aureus* from carcass samples collected at the Shone abattoir is presented in Table 1. Sample 3 had the highest bacterial load at 6.30 ± 0.14, followed by sample 1 at 5.60 ± 0.15, and sample 2 at the lowest with 3.66 ± 2.31. The overall mean was 5.18 ± 0.76 log10 CFU/mL. Although there were variations in bacterial load among the samples, the statistical analysis showed no significant difference ($p = 0.417$).

For *Salmonella*, the mean log10CFU/mL values were 3.04 ± 2.03 for sample 1, 1.03 ± 1.03 for sample 2, and 1.96 ± 1.96 for sample 3. The overall mean was 2.01 ± 0.04 $\log_{10}$ CFU/mL. While the highest count was observed in sample 1 and the lowest in sample 2, these differences were not statistically significant ($p = 0.717$), suggesting a relatively even distribution of *Salmonella* contamination across the samples.

Regarding *Shigella*, the recorded counts were 1.13 ± 1.13 for sample 1, 1.96 ± 1.96 for sample 2, and 3.14 ± 1.40 for sample 3, with an overall mean of 2.07 ± 0.09 log10CFU/mL. Sample 3 exhibited the highest load, while sample 1 had the lowest. However, statistical analysis revealed no significant difference among the samples ($p > 0.05$), indicating similar levels of *Shigella* contamination in the abattoir samples.

3.2 Evaluation of Microbial Loads in Retail Meat Outlets

Microbial analysis of beef samples collected from ten butcher shops in Shone Administrative Town revealed varying levels of contamination, as summarized in Table 2. The mean log10 CFU/mL for aerobic mesophilic bacterial counts (AMBC) ranged from 7.33 ± 0.16 in samples from butcher 2 to 7.86 ± 0.27 in samples from butcher 10. The overall mean was 7.62 ± 0.05. Although numerical differences were observed, statistical analysis showed no significant variation among the shops ($p = 0.788$). AMBC was the most commonly detected group, indicating a high level of general bacterial load across outlets.

For total coliform counts (TCC), the highest value was recorded in samples from butcher 5 (7.60 ± 0.15), while the lowest was from butcher 6 (4.90 ± 2.46). The overall mean log10CFU/mL was 6.67 ± 0.41. As with AMBC, there were no statistically significant differences between butcher shops ($p = 0.625$).

Faecal coliform counts (FCC) showed a similar pattern. The highest bacterial load was observed in samples from butcher 9 (7.33 ± 0.58), and the lowest in samples from butcher 6 (4.33 ± 2.18), with a total mean of 6.31 ± 0.40 log10CFU/mL. No significant variation was detected among the shops ($p > 0.05$).

Table 1: Mean ± S.EM $\log_{10}$ colony forming units (Mean $\log_{10}$ CFU/ml) of samples (n=3) Abattoir in Shone administrative town.

Abatttior	AMBC	TCC	FCC	*S. aures*	*Salmonella*	*Shigella*
Sample 1	6.33 ± 0.13	6.45 ± 0.14	6.16 ± 0.14	5.60 ± 0.15	3.06 ± 2.03	1.13 ± 1.13
Sample 2	6.56 ± 0.02	4.10 ± 2.45	3.85 ± 2.34	3.66 ± 2.31	1.03 ± 1.03	1.96 ± 1.96
Sample 3	6.50 ± 0.04	6.32 ± 0.07	6.03 ± 0.21	6.30 ± 0.14	1.96 ± 1.96	3.14 ± 1.40
Average	6.46 ± 0.47	5.62 ± 0.73	5.34 ± 0.69	5.18 ± 0.76	2.01 ± 0.04	2.75 ± 1.09
P-Value	0.261	0.473	0.479	0.417	0.717	0.720

Key: AMBC- aerobic mesophilic bacterial count, TCC- Total coliform count, FCC- fecal coliform count

Staphylococcus aureus counts were highest in samples from butcher 9 (7.56 ± 0.56) and lowest from butcher 6 (4.50 ± 2.25). The overall mean was 6.96 ± 0.26 log10CFU/mL. Despite the range of values, differences among samples were not statistically significant ($p > 0.05$).

For *Salmonella*, the contamination levels ranged from 6.40 ± 0.26 in samples from butcher 2 to undetectable levels (0.00 ± 0.00) in samples from butcher 3. The mean log10CFU/mL across all samples was 3.16 ± 0.59. Again, no significant differences were noted ($p > 0.05$). Lastly, *Shigella* counts were highest in samples from butcher 2 (6.86 ± 0.03) and absent in samples from butcher 3. The total mean was 2.07 ± 0.09 log10CFU/mL, with no statistically significant variation among the outlets ($p > 0.05$).

3.3 Social Characteristics of Abattoir and Retail Meat Outlet Respondents

3.3.1 Age and Sex Distribution

Table 3 summarizes the age and sex distribution of the respondents involved in the study. A total of 38 individuals participated, all of whom were male. Among them, 9 were abattoir workers and 29 were employed in retail meat outlets.Of the abattoir workers, 4 respondents (44.4%) were aged between 18 and 30 years, while the remaining 5 (55.6%) were between 31 and 40 years. Among retail meat outlet workers, 16 individuals (55.2%) fell within the 18–30 age group, 11 (37.9%) were between 31 and 40 years, and 2 respondents (6.9%) were below the age of 18.

3.3.2 Educational Background and Training of Abattoir and Butchery Workers

Table 4 summarizes the education levels and training received by workers in abattoirs and retail meat outlets in Shone Administration town. Among the nine abattoir workers interviewed, 66.7% (6workers)had completed primary school, while33.3% (3 workers)had attended high school. Notably, all abattoir workers received annual training. In contrast, the study interviewedtwenty-nine butchery shop workers. Of these, 27.6% (8 workers)were illiterate,41.4% (12 workers)had completed primary school, and31% (9 workers)had reached high school level. However, 62% (18 workers)reported that they hadnot received any trainingrelated to hygienic meat handling or sanitation in the butcher's environment, while38% (11 workers)indicated they received such training annually.

3.3.3 Work Experience of Abattoir and Retail Meat Outlet Workers

According to Table 5, 66.7% (6 workers) in the abattoirs had less than five years of work experience, while the remaining 33.3% (3 workers) had between five and ten years of experience. Among the 29 workers in retail meat outlets, 48.3% (14 workers) had less than five years of experience, 31% (9 workers) had five to ten years, and 20.7% (6 workers) had between eleven and twenty years of experience.

3.4 Practices Contributing to Microbial Contamination of Beef in Abattoirs and Retail Meat Outlets

3.4.1 Meat Handling and Hygienic Practices of Abattoir and Retail Meat Outlet Workers

Table 6 presents the findings on hygiene practices among workers in abattoirs and retail meat outlets. All nine abattoir workers interviewed reported washing their hands before entering the deboning room. However, 77.8% (7 workers) used cold water and soap, while 22.2% (2 workers) used only water. Additionally, 33.3% (3 workers) had untrimmed fingernails and were considered unhygienic. Although all abattoir workers wore aprons consistently, none used hair nets. When asked about apron cleaning habits, 22.2% (2 workers) cleaned their aprons daily, 22.2% twice a week, and 55.6% only once a week.

Regarding hand washing after using the toilet, 55.6% (5 workers) always did so, while 44.4% (4 workers) did so only sometimes. Notably, 77.8% of workers used only water, not soap, for this purpose. Among the 29 retail meat outlet workers interviewed, all stated, they washed their hands before starting work. Of these, 72.4% (21 workers) used cold water and soap, while 27.6% (8 workers) used water alone. The same proportions (72.4% and

Table 2: Mean $\pm$ S.E M $\log_{10}$ colony forming units (Mean $\log_{10}$ CFU/ml) of Butchers in Shone administrative town.

Butchers	**AMPC**	**TCC**	**FCC**	***S. aures***	**Slmonella**	***Shigella***
Butcher 1	7.66 ± 0.14	7.30 ± 0.15	6.93 ± 0.38	7.26 ± 0.54	4.46 ± 2.23	4.60 ± 2.30
Butcher 2	7.33 ± 0.16	7.40 ± 0.11	6.73 ± 0.24	7.03 ± 0.37	6.40 ± 0.26	6.86 ± 0.03
Butcher 3	7.56 ± 0.17	7.50 ± 0.15	7.16 ± 0.08	7.50 ± 0.56	0.00 ± 0.00	0.00 ± 0.00
Butcher 4	7.53 ± 0.12	4.93 ± 2.46	4.83 ± 2.41	7.30 ± 0.20	4.03 ± 2.02	4.36 ± 2.19
Butcher 5	7.53 ± 0.08	7.60 ± 0.15	7.10 ± 0.15	7.13 ± 0.21	1.86 ± 1.86	1.23 ± 1.23
Butcher 6	7.76 ± 0.37	4.90 ± 2.46	4.33 ± 2.18	4.50 ± 2.25	4.00 ± 2.04	4.26 ± 2.15
Butcher 7	7.60 ± 0.15	4.93 ± 2.48	4.46 ± 2.25	6.96 ± 0.21	2.46 ± 2.46	2.40 ± 2.40
Butcher 8	7.66 ± 0.08	7.24 ± 0.26	7.03 ± 0.21	7.16 ± 0.31	2.03 ± 2.03	4.20 ± 2.10
Butcher 9	7.70 ± 0.11	7.56 ± 0.16	7.33 ± 0.58	7.56 ± 0.56	2.13 ± 2.13	2.23 ± 2.23
Butcher 10	7.86 ± 0.27	7.33 ± 0.08	7.20 ± 0.01	7.23 ± 0.18	4.20 ± 2.10	6.50 ± 0.43
Average	7.62 ± 0.05	6.67 ± 0.41	6.31 ± 0.40	6.96 ± 0.26	3.16 ± 0.59	3.60 ± 0.60
P-value	0.788	0.625	0.515	0.335	0.542	0.208

Key: AMBC- aerobic mesophilic bacterial count, TCC- Total coliform count, FCC- fecal coliform count

Table 3: Age and Sex distribution of abattoir and retail meat outlet respondents

Variables		Abattoir workers (n=9)		Retail meat outlets worker(n=29)	
		Frequency	%	Frequency	%
Age	Below 18	0	0.0	2	6.9
	18-30	4	44.4	16	55.2
	31-40	5	55.6	11	37.9
Sex	Male	9	100.0	29	100.0
	Female	0	0.0	0	0.0

Table 4: Frequency distribution of abattoir and retail meat outlet workers according to educational status and Received training.

Educational status		Abattoir workers (n=9)		Retail meat outlet workers (n=29)	
		Frequency	%	Frequency	%
Illiterates		0	0.0	8	27.6
Primary school Education		6	66.7	12	41.4
Secondary Education		3	33.3	9	31.0
Received training	Yes	9	100.0	11	38.0
	No	0	0.0	18	62.0

Table 5: Frequency distribution of respondents according to working experience in abattoir and retail meat outlets.

Work Experience (Years)	Abattoir workers (n=9)		Retail meat outlet workers (n=29)	
	Frequency	%	Frequency	(%)
0-4	6	66.7	14	48.3
5-10	3	33.3	9	31.0
11-20	0	0.0	6	20.7

27.6%) applied to the frequency of hand washing after toilet did so always, others only sometimes. None of the retail workers used gloves while handling meat.

Furthermore, 41.4% (12 workers) handled money while serving food. While 72.4% always wore aprons, 37.9% wore visibly dirty aprons, and 58.6% did not wear hair nets. In terms of transportation, all workers reported that meat was delivered to the shops using Bajaj vehicles, which were in poor hygienic condition. Finally, regarding health certification, 77.8% of abattoir workers and 79.3% of retail workers did not possess valid medical health certificates.

Table 6: Frequency distribution of Meat hand lining and Hygienic practices of abattoir and retail meat outlet workers.

Practices		Abattoir workers (n=9)		Retail meat outlet workers (n=29)	
		Frequency	%	Frequency	%
Washing hand before starting work	Yes	9	100	29	100
	No	0	0.0	0	0.0
Using water and soap		7	77.8	21	72.4
Using only water		2	22.2	8	27.6
Not cut nail		3	33.3	0	0.0
Use apron	Always	9	100	21	72.4
	Some times	0	0.0	8	27.6
Cleaning of apron	Every day	2	22.2	8	27.6
	Twice a week	2	22.2	10	34.5
	Once a week	5	55.6	11	37.9
Hair net	Used	0	0.0	12	41.4
	Not used	9	100	17	58.6
Handling money while serving meat		0	0.0	12	41.4
Washing hand after toilet	Always	5	55.6	21	72.4
	Some times	4	44.4	8	27.6
Presence of health certificate	Yes	2	22.2	6	20.7
	No	7	77.8	23	79.3

3.4.2 Hygienic Conditions of Abattoir and Retail Meat Outlet Facilities

Table 7 presents findings on hygiene practices at the abattoir and retail meat shops in Shone administrative town. Among the 9 abattoir workers interviewed, 88.9% (8 workers) reported that no daily cleaningoccurredafter slaughtering. The facility also lacked proper separation of slaughter stages such as skinning, evisceration, deboning, and meat delivery. Moreover, no rodent or insect control measures were in place, and essential sanitation tools like hot water, sterilizers, and retention rooms were absent. The lairage was poorly maintained, with accumulated cattle dung and feces-contaminated animals being slaughtered.

Additionally, 44.4% (4 workers) indicated that carcasses sometimes came into contact with the floor or the outer side of the skin/hide, increasing the risk of contamination. Out of 10 retail meat outlets inspected, 80% were found to have poor hygienic conditions, despite daily cleaning with water and soap. From 29 meat outlet workers surveyed, 41.3% (12 workers) stated that butchers did not practice daily personal hygiene.

Regarding leftover meat storage, 60% (6 out of 10) of the butchers did not use refrigerators, while 40% (4 outlets) had refrigerators in their shops. Metal hooks were commonly used in 80%of the outlets for hanging meat. All retail workers confirmed that they sold unchilled meat. For fly control, 70% of the shops used glass windows and cleaned daily, while the remaining 30% relied solely on glass windows.

4 Discussion

4.1 Microbial Load Assessment in Abattoir and Retail Meat Outlets

Aerobic mesophilic bacterial count (AMBC) is a widely accepted indicator of the general microbiological quality of meat and the hygienic conditions under which is processed. Elevated AMBC levels often reflect poor sanitation, cross-contamination, or inadequate handling practices during slaughter and retail.

In the current study, AMBC values in Shone town abattoir ranged from 6.33±0.13 to 6.56 ±0.02 log CFU/ml, with a mean of 6.46±0.47 log CFU/ml. The findingsare comparable to those reported by Ntanga (2013) in Tanzania (6.60±0.37 log CFU/ml), but higher than those observed by (Ahmad et al., 2013; Haileselassie et al., 2012; M. A. Nervy et al., 2011), indicating variability likely due to differences in hygiene protocols and facility management.

Retail butcher shops exhibited even higher AMBC levels, ranging from 7.33±0.16 to 7.86±0.27 log CFU/ml, with a mean of 7.62±0.05 log CFU/ml. These values exceed those reported by Gebeyehu Arse et al. (2013) and Melkamnesh and Mulugeta (2017), but are consistent with findings from Ntanga (2013) and Ahmad et al. (2013). The elevated bacterial loads in retail outlets may be due to contamination from handling tools, water, carcass transport, and environmental exposure. Although numerical differences were observed between abattoir and retail samples, statistical analysis revealed no significant difference ($p > 0.05$), and this is probable due to uniformly poor hygienic practices across the meat supply chain. This aligns with findings by Haileselassie et al. (2012), who emphasized the role of disorganized processing and inadequate personal hygiene in

Table 7: Frequencies distribution of abattoir and retail meat outlets facilities in Shone administrative town.

Practices		Responses (abattoir workers)		Responses (Retail meat outlet workers)	
		Frequency	%	Frequency	%
Daily cleanness of abattoir and butchers	Yes	1	11.1	17	57.7
	No	8	88.9	12	41.3
Daily cleanness of equipments	Yes	9	100.0	29	100.0
Water availability	Yes	9	100.0	29	100.0
	No	0	0	0	0
Contact of carcass with skin/hind or floor	Yes	4	44.4		
	No	5	55.6		
Refrigerator	Used			11	37.9
	Not used			18	62.1
Ways of flies control	Uses glass window only			8	27.6
	Glass window and clean daily			21	72.4

microbial contamination.

Recent studies reinforce these concerns. For instance, Kebede and Getu (2023) reported AMBC values ranging from 2.75 to 7.52 log CFU/g in abattoirs and 2.49 to 5.16 log CFU/g in butcher shops in Assosa, Ethiopia, with over 40% of samples exceeding acceptable limits. Similarly, Jaja et al. (2018) found AMBC levels exceeding 6.0 log CFU/cm² in informal meat sectors in South Africa, highlighting the public health risks posed by inadequate sanitation.

Importantly, the AMBC values recorded in this study exceed the maximum acceptable limit of 6.00 log CFU/cm² set by the International Commission on Microbiological Specifications for Foods (International Commission on Microbiological Specifications for Foods (ICMSF), 1985). According to Food and Agriculture Organization (FAO) (2007), total viable counts above 5.0 log CFU/cm² indicate unacceptable hygiene and necessitate corrective actions throughout the meat production and distribution chain.

Total Coliform Counts (TCC)

Coliform bacteria are traditionally used as indicators of fecal contamination and potential presence of enteric pathogens. While some coliforms inhabit the human intestinal tract, many are environmental and not necessarily of sanitary concern (Greenberg & Hunt, 1985). However, high coliform counts in food products, particularly meat, are undesirable and suggest poor hygiene during processing.

In the current study, the highest mean log value of TCC in abattoir samples was 6.45 ±0.14 log CFU/ml, while the lowest was 4.10 ±2.45 log CFU/ml. The overall mean was 5.62 ±0.73 log CFU/ml. These values are lower than those reported by Ntanga (2013), who found a mean of 6.33 ±0.02 log CFU/ml, but higher than the 2.29 ±2.38 log CFU/ml reported by Chepkemoi (2016). The elevated TCC in this study may be duet o inadequate hygiene practices, such as all workers participating in multiple tasks without proper sanitation or sterilization of equipment.

No statistically significant differences were observed among carcass samples ($p > 0.05$), likely due to uniform handling practices and shared equipment. In retail meat outlets, TCC ranged from 4.90 ±2.46 to 7.60 ±0.15 log CFU/ml, with a mean of 6.66 ±0.41 log CFU/ml. These values exceed those reported by Gebeyehu Arse et al. (2013), Melkamnesh and Mulugeta (2017), and Natanga (2013), who found means of 5.55, 3.97, and 1.72 log CFU/ml, respectively. Such discrepancies may reflect differences in hygiene standards, equipment sanitation, and worker practices.

Recent studies continue to highlight the role of coliforms as indicators of meat hygiene. For instance, Kang et al. (2020) emphasized the need for improved detection methods to reduce false positives, while Koech (2024) linked high coliform counts to poor handling in Nairobi butcheries.

Fecal Coliform Counts (FCC)

Fecal coliforms are more specific indicators of fecal contamination and poor sanitary conditions. In this study, FCC in abattoir samples ranged from 3.85 ±2.34 to 6.16 ±0.14 log CFU/ml, with a mean of 5.34 ±0.69 log CFU/ml. These values are lower than those reported by Natanga (2013) but higher than those by Bhandare et al. (2009) and M. A. Nervy et al. (2011).

The high FCC levels may be due to processing activities conducted on the abattoir floor and the lack of separation between clean and dirty zones, leading to cross-contamination. In retail outlets, FCC ranged from 4.33 ±2.18 to 7.33 ±0.58 log CFU/ml, with a mean of 6.31 ±0.40 log CFU/ml. These values exceed the Food and Agriculture Organization (FAO) (2007) recommended limit of 3.0 log CFU/g, indicating unacceptable hygiene levels. Recent findings by Hanyinza et al. (2020) in Zambia and Metaferiya (2022) in Ethiopia support the conclusion that poor hygiene and handling practices significantly contribute to elevated FCC in meat.

***Staphylococcus aureus* Counts**

Staphylococcus aureus is a pathogenic bacterium commonly found on the skin and mucous membranes of humans and animals. It can cause foodborne illness when present in high

numbers. In this study, S. *aureus*counts in retail meat outlets ranged from 4.50 ±2.25 to 7.56 ±0.56 log CFU/ml, with a mean of 6.96 ±0.26 log CFU/ml. These values are higher than those reported by Ahmad et al. (2013), Gebeyehu Arse et al. (2013), and Twum (2015).

The high prevalence of S. *aureus*is likely due to poor personal hygiene among meat handlers and the use of unsterilized equipment. Human hands are a major source of cross-contamination in food handling environments (Kanko et al., 2023). In abattoir samples, S. *aureus*counts ranged from 3.66 ±2.31 to 6.30 ±0.14 log CFU/ml, with a mean of 5.18 ±0.76 log CFU/ml.

Recent studies by Pérez-Boto et al. (2023) and Mumed et al. (2023) confirm the persistence of S. *aureus*in meat processing environments and its resistance to common antibiotics, underscoring the need for improved hygiene and monitoring.

Salmonella Counts

This study revealed the presence of *Salmonella* in both abattoir and retail meat outlets in Shone town. Among ten butcher shops sampled, nine showed contamination, with the highest mean log count reaching 6.46 ±0.26 CFU/ml. In the abattoir, *Salmonella* was also detected, with mean log values ranging from 1.03 ±1.03 to 3.04 ±2.03 CFU/ml. Although microbial loads differed between the two sources, the variation was not statistically significant ($p > 0.05$), suggesting similar hygiene and meat handling practices across the sites.

The overall mean *Salmonella* counts were 3.16 ±0.59 CFU/ml in butcher shops and 2.01 ±0.04 CFU/ml in the abattoir. These findings align with Twum Ernest (2015), who reported 3.60 ±0.12 CFU/ml in East Ghana, but contrast with Gebeyehu Arse et al. (2013), who found no *Salmonella* in Adama Town, Ethiopia. The contamination likely stems from poor hygiene, including unclean equipment, exposure to flies, and cross-contamination from handlers factors also highlighted in recent studies (Etikudike et al., 2022; Hammuel & Briska, 2024).

Shigella Counts

Shigella was detected in all abattoir samples, with mean log values ranging from 1.13 ±1.13 to 3.14 ±1.40 CFU/ml. In butcher shops, all but one (Butcher 3) tested positive, with the highest count at 6.86 ±0.03 CFU/ml. No significant difference was observed between the abattoir and butcher shops ($p > 0.05$), again indicating uniformity in meat handling practices.

These results differ from Gebeyehu Arse et al. (2013), who reported no *Shigella* in Adama Town. The presence of *Shigella* in this study may be due to unhygienic practices such as the use of contaminated knives and cutting boards, poor personal hygiene, and inadequate sanitation findings echoed in recent literature (Hammuel & Briska, 2024; Rabins, 2021).

Age and Sex Distribution

In the abattoir, 55.6% of workers were aged 31–40, while 44.4% were 18–30. In butcher shops, 55.6% were 18–30, 37.4% were 31–40, and 6.8% were under 18. All workers were male, consistent with findings by Adzitey et al. (2011), who noted that meat processing is typically dominated by young and middle-aged men due to the physical demands of the work.

Educational Status and Training

In the abattoir, 66.7% of workers had primary education and 33.3% had secondary education; all had received hygiene training. In contrast, 27.6% of butcher workers had no formal education, 41.4% had primary, and 31.0% had secondary education. These figures are lower than those reported in Nairobi and Tanzania (Chepkemoi, 2016; Ntanga, 2013), where higher educational attainment was observed. Low education levels may hinder comprehension and implementation of hygienic practices. Recent studies confirm that education and training significantly influence food safety behavior (AzekoAsati et al., 2024; Kassaw et al., 2024).

Work Experience

Most abattoir (66.7%) and butcher (48%) workers had less than five years of experience. This limited experience, coupled with low education and training, may reduce adherence to hygienic practices and limit peer learning. Similar concerns were raised by (Ashuro et al., 2023), who found that work experience significantly affects meat hygiene practices.

4.2 Practices Contributing to Microbial Contamination of Beef in Abattoirs and Retail Meat Outlets

Hygiene Practices of Workers

The study revealed several hygiene-related shortcomings among abattoir and retail meat outlet workers that contribute to microbial contamination of beef. Although all abattoir workers reported washing their hands before entering the deboning room, 22.2% used only water, and 77.8% did not use soap. Furthermore, only 55.6% consistently washed their hands after using the toilet, while 44.4% did so occasionally. Additionally, 33.3% of workers had untrimmed nails, posing further hygiene risks.

Despite all abattoir workers wearing aprons, most did not clean them daily, and none wore hairnets. These findings contrast with Natanga (2013), who reported that most abattoir workers in Morogoro, Tanzania, did not wear protective clothing. However, the lack of daily cleaning and absence of hairnets in the current study still presents significant contamination risks.

Retail meat outlet workers also demonstrated poor hygiene. While all washed their hands before work, 27.6% used only water, and only 27.6% consistently washed their hands after toilet use. None used gloves, and 41.4% handled money while serving meat, a known vector for microbial transmission (N. J. Nervy et al., 2011). These practices are inconsistent with findings from Chepkemoi (2016) and Little et al. (1999), who reported even lower hand washing rates in Kenya and the UK, respectively.

Meat was commonly transported in Bajaj vehicles, which were also used for other purposes, including transporting people and goods. This practice violates hygiene standards and increases the risk of contamination. Similar concerns were raised by Adzitey et al. (2011) in Ghana and Chepkemoi (2016) in Kenya.

A significant proportion of workers lacked medical health certification 77.8% in abattoirs and 79.3% in retail outlets raising concerns about their fitness to handle food. This is higher than the 15.4% reported by Haileselassie et al. (2013) in Mekelle, Ethiopia, but lower than rates in Nairobi and Isiolo, Kenya (Chepkemoi, 2016). Recent studies confirm that poor hygiene practices, inadequate protective clothing, and improper meat transportation significantly contribute to microbial contamination. For instance, Kebede and Getu (2023) found high levels of *Staphylococcus aureus* and *Salmonella* in meat samples from Ethiopian abattoirs and butcher shops, largely due to poor handling and environmental hygiene.

Hygienic Conditions of Abattoir and Retail Meat Outlet Facilities The Shone town abattoir is situated near residential areas, limiting its potential for expansion and exposing it to unauthorized access and vermin due to the absence of fencing. Observations revealed that 88.9% of abattoir workers reported no routine cleaning after slaughtering, and there was no clear separation between critical processes such as skinning, evisceration, deboning, and carcass delivery. All operations were conducted on a contaminated floor, increasing the risk of microbial contamination.

The facility lacked essential infrastructure, including septic tanks and designated waste disposal pits. Effluents were stored in a poorly maintained borehole with limited capacity, often overflowing and contaminating the surrounding environment. Solid wastes such as faeces, horns, and tissue scraps were discarded near the abattoir, creating foul odors and attracting pests like rodents, flies, and stray animals.

These findings align with previous studies. For instance, Adzitey et al. (2011) and Adeyemo et al. (2009) reported similar unhygienic practices in Ghana and Nigeria, respectively, where carcasses were processed on bare or unclean floors due to the absence of hoisting equipment. Akinro et al. (2009) highlighted the environmental hazards posed by effluent seepage into water sources. More recently, Yimana and Hassen (2024) emphasized that inadequate infrastructure, lack of trained personnel, and poor sanitation practices continue to compromise meat safety in Ethiopian abattoirs. Retail meat outlets in Shone town also exhibited poor hygienic conditions. Although 80% of shops reported daily cleaning with water and soap, most used unclean wooden chopping blocks and lacked refrigeration for leftover meat. Only 40% of outlets had refrigerators, and many mixed leftover meat with fresh cuts, increasing the risk of cross-contamination. Domestic flies were prevalent due to the practice of opening glass windows during sales, allowing insects to enter.

These observations are consistent with findings by Nurye and Demlie (2021), who reported high microbial loads in meat from butcher shops due to inadequate hygiene and poor infrastructure. Similarly, Ali et al. (2010) noted that cleaning once daily with detergent and water is insufficient to maintain sanitary conditions in meat retail environments.

Overall, the study underscores the urgent need for improved infrastructure, regular sanitation, proper waste management, and training of personnel to ensure meat safety from slaughter to retail.

5 Conclusion

This study found that meat from both abattoirs and retail outlets in Shone administrative town was contaminated with high levels of microorganisms, as indicated by elevated Aerobic Mesophilic Bacterial Count (AMBC), Total Coliform Count (TCC), Fecal Coliform Count (FCC), *Staphylococcus aureus*, *Salmonella*, and *Shigella*. The results suggest that both the abattoir and retail meat outlets failed to meet basic sanitation and hygiene standards.

The poor hygiene and sanitation practices observed at slaughterhouses and butcher shops likely contributed to the microbial contamination, posing a serious public health risk. The presence of these pathogens highlights the potential for food borne illnesses if contamination is not addressed.To protect public health, it is essential to promote proper meat handling and sanitation practices through education and enforcement of hygiene standards in abattoirs and butcheries.

Funding Statement

This research did not receive funding from any public, commercial, or non-profit organizations.

Data Availability Statement

All data supporting the findings of this study are included in the article. Requests for additional information can be directed to the corresponding author.

Declaration of Interest

The authors declare no conflicts of interest.

Acknowledgment

The authors fully acknowledge Hawassa University for providing the laboratory to do research, the Shone town municipality, and all the abattoirs and the retail outlets for their kind cooperation during sample collection and interviews.

References

Adeyemo, O. K., Adeyemi, I. G., & Awosanya, E. J. (2009). Cattle cruelty and risk of meat contamination at Akinyele cattle market and slaughter slab in Oyo state, Nigeria. *Nigerian Veterinary Journal*, *30*(1), 34–38.

Adzitey, F., Teye, G. A., & Kutah, W. N. (2011). Microbial quality of beef sold on selected markets in the Tamale metropolis in the Northern region of Ghana. *Livestock Research for Rural Development*, *23*(1).

Ahmad, M. U. D., Sarwar, M., Najeeb, M. F., & Anjum, A. A. (2013). Microbial quality of meat and meat products in Lahore. *Pakistan Journal of Zoology*, *45*(4), 1041–1046.

Akinro, A. O., Ologunagba, I. B., & Yahaya, O. (2009). Environmental implications of unhygienic operation of a city abattoir in Akure, Western Nigeria. *ARPN Journal of Engineering and Applied Sciences*, *4*(9), 61–63.

Ali, A. A., Abdelgadir, W. S., & Elamin, K. M. (2010). Microbial contamination of sheep carcasses at El Kadero slaughterhouse Khartoum state, Sudan. *Journal of Animal and Veterinary Advances*, *9*(15), 2004–2006.

American Public Health Association (APHA). (2017). *Compendium of methods for the microbiological examination of foods* (5th ed.). APHA.

Ashuro, Z., Zeysse, N., & Ayalew, M. (2023). Meat hygiene knowledge, handling practices and associated factors among meat handlers in Gedeo zone, Ethiopia. *Scientific Reports*, *13*, 42225.

AzekoAsati, D., Abdulai, P. M., Boateng, K. S., Appau, A. A. A., Ofori, L. A., & Agyekum, T. P. (2024). Food safety knowledge and practices among raw meat handlers and the microbial content of raw meat sold at Kumasi abattoir butchery shops in Kumasi, Ghana. *BMC Public Health*, *24*, 975.

Bartholomew, J. W., & Mittwer, T. (1952). The gram stain. *Bacteriological Reviews*, *16*(1), 1–29. https://doi.org/10.1128/br.16.1.1-29.1952

Beijerinck, M. W. (1889). *The bacteria and their culture methods*. F.C.W. Vogel.

Bhandare, S. G., et al. (2007). A study on microorganisms associated with raw meat. *Journal of Public Health and Epidemiology*, *1*(1), 1–5.

Bhandare, S. G., Sherikar, A. T., Paturkar, A. M., Waskar, V. S., & Zende, R. J. (2009). A comparison of microbial contamination on sheep/goat carcasses in a modern Indian abattoir and traditional meat shops. *Food Control*, *20*(5), 506–512.

Buchanan, R. E., & Gibbons, N. E. (1974). *Bergey's manual of determinative bacteriology.*

Cappuccino, J. G., & Welsh, C. T. (2017). *Microbiology: A laboratory manual* (11th ed.). Pearson.

Central Statistical Agency (CSA). (2013). *Agricultural sample survey 2012/2013*. Addis Ababa, Ethiopia.

Chepkemoi, S. (2016). *Assessment of hygiene and safety practices in meat handling in Nairobi and Isiolo counties, Kenya* [Master's thesis]. University of Nairobi.

Chester, B. (1979). Semi-quantitative catalase test as an aid in identification of oxidative and nonsaccharolytic gram-negative bacteria. *Journal of Clinical Microbiology*, *10*(4), 525–528. https://doi.org/10.1128/jcm.10.4.525-528.1979

Duguma, B., & Janssens, G. P. (2020). Assessment of livestock feed resources and coping strategies with dry season feed scarcity in mixed crop–livestock farming systems around the Gilgel Gibe catchment, southwest Ethiopia. *Sustainability*, *13*(19), 10713. https://doi.org/10.3390/su131910713

Etikudike, V., Egbunike, E., & Nwakozor, C. (2022). Prevalence and antibiogram of Salmonella and Shigella species isolated from retailed meat in Ihiala town, Nigeria. *Journal of International Research in Medical and Pharmaceutical Sciences*, *17*(3), 6–12.

Food and Agriculture Organization (FAO). (2007). *Meat hygiene manual.* Food and Agriculture Organization of the United Nations.

Forbes, B. A., Sahm, D. F., & Weissfeld, A. S. (2007). *Bailey & scott's diagnostic microbiology* (12th ed.). Mosby Elsevier.

Gebeyehu Arse, T., et al. (2013). Microbial quality of meat from abattoir and butcher shops in Adama town, Ethiopia. *Ethiopian Veterinary Journal*, *17*(2), 1–15.

Greenberg, A. E., & Hunt, D. A. (1985). *Standard methods for the examination of water and wastewater* (16th ed.). American Public Health Association.

Haileselassie, M., Taddele, H., Adhana, K., & Kalayou, S. (2012). Food safety knowledge and practices of abattoir and butchery workers in Ethiopia. *Food Control*, *26*(2), 452–455.

Haileselassie, M., Taddele, H., Adhana, K., & Kalayou, S. (2013). Food safety knowledge and practices of abattoir and butchery workers in Mekelle city, Ethiopia. *Asian Pacific Journal of Tropical Biomedicine*, *3*(5), 407–412.

Hammuel, C., & Briska, J. (2024). Occurrence of Salmonella and Shigella species on meat contact surfaces in Wukari, Nigeria. *African Journal of Biochemistry and Molecular Biology Research*, *1*(1), 113–123.

Hanyinza, S., Ndashe, K., Mfune, R., et al. (2020). Bacteriological quality of beef and hygiene practices of food handlers in butcheries in Kasama district, Zambia. *medRxiv*. https://doi.org/10.1101/2020.06.06.20124214

International Commission on Microbiological Specifications for Foods (ICMSF). (1985). *Microorganisms in foods 2: Sampling for microbiological analysis: Principles and specific applications*. University of Toronto Press.

Jaja, I. F., Green, E., & Muchenje, V. (2018). Aerobic mesophilic, coliform, Escherichia coli, and Staphylococcus aureus counts of raw meat from the formal and informal meat sectors in South Africa. *International Journal of Environmental Research and Public Health*, *15*(4), 819. https://doi.org/10.3390/ijerph15040819

Kang, J. Y., Lee, S. H., Jo, A. H., et al. (2020). Improving the accuracy of coliform detection in meat products using modified dry rehydratable film method. *Food Science and Biotechnology*, *29*, 1289–1294.

Kanko, T., Seid, M., & Alemu, M. (2023). Evaluation of bacteriological profile of meat contact surfaces, handling practices of raw meat and its associated factors in butcher shops of Arba Minch town, southern Ethiopia—a facility based cross sectional study. *Food*

Safety and Risk, *10*, 1. https://doi.org/10.1186/s40550-023-00102-2

Kassaw, S., Damtew, M., & Geto, A. (2024). Assessment of knowledge, attitudes, and hygienic practices of meat handlers in Arbaminch town, Ethiopia. *SSRN Electronic Journal*. https://doi.org/10.2139/ssrn.5014963

Kebede, M. T., & Getu, A. A. (2023). Assessment of bacteriological quality and safety of raw meat at slaughterhouse and butchers' shop in Assosa town, Ethiopia. *BMC Microbiology*, *23*, 403. https://doi.org/10.1186/s12866-023-03106-2

Kenaw, Z., Ejeso, A., Deresse, D., & Olkeba, B. K. (2024). Microbial contamination and meat handling practices in Hawassa city butcher shops, Ethiopia. *Environmental Health Insights*, *18*, 11786302241293289. https://doi.org/10.1177/11786302241293289

Koech, P. C. (2024). *Assessing microbiological safety of meat sold in butcheries in Nairobi and associated handling practices* [Master's thesis]. University of Nairobi.

Legese, G., Gelmesa, U., Jembere, T., Degefa, T., Bediye, S., Teka, T., Temesgen, D., Tesfu, Y., Berhe, A., Gemeda, L., Takele, D., Beyene, G., Belachew, G., Hailu, G., & Chemeda, S. (2023). *Ethiopia national dairy development strategy 2022–2031*. Ministry of Agriculture, Federal Democratic Republic of Ethiopia. Addis Ababa, Ethiopia.

Li, Y., Mayberry, D., Jemberu, W., Schrobback, P., Herrero, M., Chaters, G., Knight-Jones, T., & Rushton, J. (2023). Characterizing Ethiopian cattle production systems for disease burden analysis. *Frontiers in Veterinary Science*, *10*, 1233474.

Little, C. L., et al. (1999). Microbiological quality of retail meat in the UK. *Journal of Applied Microbiology*, *87*(4), 535–544.

MacFaddin, J. F. (2000). *Biochemical tests for identification of medical bacteria* (3rd ed.). Lippincott Williams & Wilkins.

Madigan, S., Deneault, A.-A., Duschinsky, R., Bakermans-Kranenburg, M. J., Schuengel, C., van IJzendoorn, M. H., Ly, A., Fearon, R., Eirich, R., & Verhage, M. L. (2024). Maternal and paternal sensitivity: Key determinants of child attachment security examined through meta-analysis. *Psychological bulletin*, *150*(7), 839.

Melkamnesh, A., & Mulugeta, K. (2017). Microbial quality of meat in Bahir Dar city, Ethiopia. *Ethiopian Journal of Veterinary Science*, *11*(2), 45–52.

Metaferiya, H. M. (2022). Microbiological quality of meat in butcher shops in Gelemso town, Ethiopia. *Austin Journal of Tropical Medicine & Hygiene*, *3*(1), 1–6.

Mitchell, J. G., & Kogure, K. (2006). Bacterial motility: Links to the environment and a driving force for microbial physics. *FEMS Microbiology Ecology*, *55*(1), 3–16. https://doi.org/10.1111/j.1574-6941.2005.00003.x

Mumed, B. A., Jafer, M., & Belina, D. (2023). *Assessment of hygienic practice, isolation and antibiogram profiles of Staphylococcus aureus from goat meat in Eastern Ethiopia* [Master's thesis]. Haramaya University.

Natanga, L. (2013). *Assessment of hygiene and sanitation practices in abattoirs in Morogoro municipality, Tanzania* [Master's thesis]. Sokoine University of Agriculture.

Nervy, M. A., et al. (2011). Microbiological quality of meat in selected markets. *Journal of Food Safety*, *31*(3), 345–351.

Nervy, N. J., et al. (2011). Microbial contamination of currency notes in circulation. *Journal of Environmental Health Research*, *11*(2), 60–64.

Ntanga, P. D. (2013). *Assessment of meat handling practices and awareness of meat borne diseases among meat vendors in Morogoro municipality, Tanzania* [Master's thesis]. Sokoine University of Agriculture.

Nurye, M., & Demlie, M. (2021). Assessment of hygienic practices and microbial quality of meat at slaughterhouses and butcher's shops in West Hararghe zone, Ethiopia. *Abyssinia Journal of Science and Technology*, *6*(2), 32–41.

Oyeleke, S. B., & Manga, B. S. (2008). *Essentials of laboratory practical in microbiology*. Tobest Publishers.

Pérez-Boto, D., D'Arrigo, M., García-Lafuente, A., et al. (2023). Staphylococcus aureus in the processing environment of cured meat products. *Foods*, *12*(11), 2161. https://doi.org/10.3390/foods12112161

Rabins, S. L. (2021). Epidemiological study on Shigella from meat and its public health significance. *International Journal of Current Microbiology and Applied Sciences*, *10*(12), 433–443.

Reda, M., Mebrahtu, T., Gebru, M., et al. (2025). Prevalence, antimicrobial resistance, and public health risk assessment of zoonotic bacterial pathogens in raw cattle meat from three zonal cities in Tigray, Ethiopia. *BMC Microbiology*, *25*, 722. https://doi.org/10.1186/s12866-025-04469-4

Sperber, W. H., & Tatini, S. R. (1975). Interpretation of the tube coagulase test for identification of Staphylococcus aureus. *Applied Microbiology*, *29*(4), 502–505. https://doi.org/10.1128/am.29.4.502-505.1975

Twum, E. (2015). Microbial contamination of meat in New Abirem market, Ghana. *African Journal of Food Science*, *9*(3), 123–129.

Yamane, T. (1967). *Elementary sampling theory*. Prentice-Hall.

Yimana, M., & Hassen, A. (2024). Assessment of the operational facilities and hygienic practices of abattoirs and butcher shops in Ethiopia. *Discover Food*, *4*(1), 88.